



Review

Recent advances in metal/covalent organic frameworks based materials: Their synthesis, structure design and potential applications for hydrogen production

Wei-Ting Chung^{a,1}, Islam M.A. Mekheimer^{b,1}, Mohamed Gamal Mohamed^{c,1}, Ahmed M. Elewa^b, Ahmed F.M. EL-Mahdy^c, Ho-Hsiu Chou^{b,*}, Shiao-Wei Kuo^{c,*}, Kevin C.-W. Wu^{a,d,*}

^a Department of Chemical Engineering, National Taiwan University (NTU), No. 1, Sec. 4, Roosevelt Road, Taipei 10617, Taiwan

^b Department of Chemical Engineering, National Tsing Hua University, Hsinchu 300044, Taiwan

^c Department of Materials and Optoelectronic Science, Center for Crystal Research, National Sun Yat-Sen University, Kaohsiung 804, Taiwan

^d Institute of Biomedical Engineering & Nanomedicine, National Health Research Institute, Keyan Road, Zhunan, Miaoli City 350, Taiwan

ARTICLE INFO

Article history:

Received 30 August 2022

Received in revised form 3 January 2023

Accepted 1 February 2023

Available online 9 March 2023

Keywords:

Metal-organic frameworks
Covalent-organic frameworks
Catalytic hydrogen evolution
Steam reforming reaction
Dry reforming reaction

ABSTRACT

In recent years, both-organic frameworks (MOFs) based and covalent-organic frameworks (COFs) based materials have been extensively utilized for catalysis because of their specific surface area, tunable porosity, and structural versatility. Amongst the various MOFs/COFs-based catalysis implementation, catalytic hydrogen production (H_2) processes have subbed attention to alternative energy stemming from fossil fuel and the increasing global warming issue. As the growing demand for a sustainable, renewable, safe, and stable energy supply for the future is in urgent need, had urgently needed potential green energy or future energy attributed to the promising power-to-gas energy storage technology and the environmentally friendly zero carbon emission. Nowadays, most of the hydrogen is granted by the reforming reactions because of its mature large-scale production technology and economic benefits; in addition, electrochemical water splitting is another prospective route for hydrogen generation to fulfill the carbon reality. In this review, we provide an overview of the recent applications and developments of hydrogen production by using MOFs/COFs and the derived catalysts, including (1) the steam reforming reaction, (2) the dry reforming reaction, (3) the electrocatalytic water splitting, (4) the photocatalytic water splitting, and (5) the photo-electrocatalytic water splitting. Furthermore, we focus on the design of MOF/COF-based catalysts. Finally, the opportunities and challenges are also overviewed to guide the MOFs/COFs-derived catalysts applied for their hydrogen production (H_2).

© 2023 Elsevier B.V. All rights reserved.

Contents

1. Introduction	2
2. Introduction of MOFs and MOF-derived materials	4
3. Synthetic approaches of MOF materials	5
3.1. Solvothermal synthesis	6
3.2. Electrochemical synthesis	6
3.3. Mechanochemical synthesis	6
3.4. Microwave-assisted synthesis	6
3.5. Sonochemical synthesis	6
4. Covalent organic framework (COF)	6
4.1. Introduction and design skeleton structure of COFs	6
5. Synthetic approaches of COF materials	8
5.1. Solvothermal synthesis	8

* Corresponding authors.

E-mail addresses: hhchou@mx.nthu.edu.tw (H.-H. Chou), kuoswf@faculty.nsysu.edu.tw (S.-W. Kuo), kevinwu@ntu.edu.tw (K.C.-W. Wu).

¹ The authors contributed equally to this work.

5.2.	Mechanochemical synthesis	9
5.3.	Sonochemical synthesis	10
5.4.	Microwave synthesis	10
5.5.	Light-induced synthesis	10
5.6.	Vapor-assisted synthesis	10
5.7.	Interfacial synthesis	10
5.8.	Post-Synthetic COF modifications	11
5.9.	Multicomponent reactions method	11
6.	Hydrogen	12
6.1.	Hydrogen production by using MOFs and MOF-derived catalysts	14
6.1.1.	Hydrogen production from steam reforming reaction	14
6.1.2.	The influence of metal selection on catalysts	15
6.1.3.	The influence of thermal stability on catalysts	16
6.1.4.	The influence of chemical stability on catalysts	16
6.2.	Hydrogen production from the dry reforming reaction	17
6.2.1.	The influence of metal selection and thermal stability on catalysts	17
6.2.2.	The influence of chemical stability on catalysts	18
6.2.3.	The nonthermal-activated dry reforming reaction	19
7.	Photo and/or electrocatalytic systems for hydrogen evolution, oxygen evolution, and overall water splitting assisted by covalent organic frameworks	20
7.1.	COFs for photocatalytic HER, OER, and overall water splitting	20
7.1.1.	COFs for photocatalytic HER	20
7.1.2.	COF for photocatalytic OER	28
7.1.3.	COF for photocatalytic overall water splitting	28
8.	COFs for electrocatalytic HER, OER, and overall water splitting	29
8.1.	COFs for electrocatalytic HER	29
8.1.1.	Metal-free COFs for electrocatalytic HER	32
8.1.2.	Metallic COFs for electrocatalytic HER	34
8.2.	COFs for electrocatalytic (OER)	35
8.2.1.	Metal-free COFs for electrocatalytic (OER)	38
8.2.2.	Metallic COF for electrocatalytic (OER)	40
8.3.	COFs for electrocatalytic overall water splitting	42
8.4.	COFs for photoelectrochemical water splitting	43
9.	Conclusion	45
	CRedit authorship contribution statement	45
	Declaration of Competing Interest	46
	Acknowledgement	46
	References	46

1. Introduction

Developing high-performance materials is essential to improving energy density and conversion efficiency [1–6]. Metal-organic frameworks (MOFs) and covalent organic frameworks (COFs) materials are a new class of porous framework materials with stable pore structures and ultrahigh-specific surface areas [7–12]. MOFs and COFs, which can be designed and fabricated efficiently, have been lifeful organic materials for the past two decades. Also, a MOF or COF's pore structure can be adjusted by modifying its backbone and various functionalization modifications [13–17]. Their unique compositions and designs make them suitable for gas storage and separation [18], batteries [19], catalysis [20], sensors [21], photo-energy conversion [22], drug delivery [23,24], and optoelectronic [25]. MOFs have several advantages, including a large specific surface area, a high porosity, and the ability to control the structure and morphology of the pore spaces. However, traditional MOFs low stability and low electrical conductivity limit these materials' applications [26]. Although MOFs have achieved considerable advancement in electrochemical applications [27–29]. One of the primary restraints in the application of MOFs is that their surface area and adsorption capacity dramatically decrease when exposed to moisture [30–32]. In addition, most MOFs have intrinsically poor electrical conductivity, and their narrow micropores limit the rapid diffusion of gas inside the pores; thus, these defects have impeded their full potential. These disadvantages of

MOFs, MOF composites, which combine MOFs with various functional materials and make them candidates for applications related to clean energy, have been proposed recently. Metal-organic frameworks (MOFs), also recognized as porous coordination polymers (PCPs), were first published by Prof. O. M. Yaghi in 1995 [33]. Prof. Yaghi and his co-workers added $\text{Cu}(\text{NO}_3)_2 \cdot 2.5\text{H}_2\text{O}$, 4,4'-bpy, and 1,3,5-triazine in deionized water and transferred them into a stainless bomb for the sequent heating process [33]. They successfully synthesized the $\text{Cu}(4,4'\text{-bpy})1.5\text{NO}_3(\text{H}_2\text{O})_{1.25}$, by hydrothermal method and they called it the zeolite-like crystalline material, which is the well-known metal-organic framework [33]. MOFs are varied by various arrangements comprising metal clusters or metal ions as nodes and organic ligands as linkers, as shown in Fig. 1 [34]. Owing to the outstanding large Brunauer-Emmett-Teller (BET) specific surface area ranging from 1000 to 10,000 m^2/g , large pore volume, and impressive structural versatility, MOFs certainly dropped a bombshell to the polymer chemistry field [35]. Compared with the common porous materials such as zeolite, silica gel, and metal oxides, MOFs perform much superior. Besides, due to the modularity between metal clusters and organic ligands, >90,000 kinds of MOFs have been synthesized and simulated over the past decades. The number is growing daily, which indicates that MOFs are prospective and developing materials for many applications [36,37]. With the different dimensional arrangements, MOFs could be assembled in either 2-dimensional or 3-dimensional structures. Since the discovery of graphene in

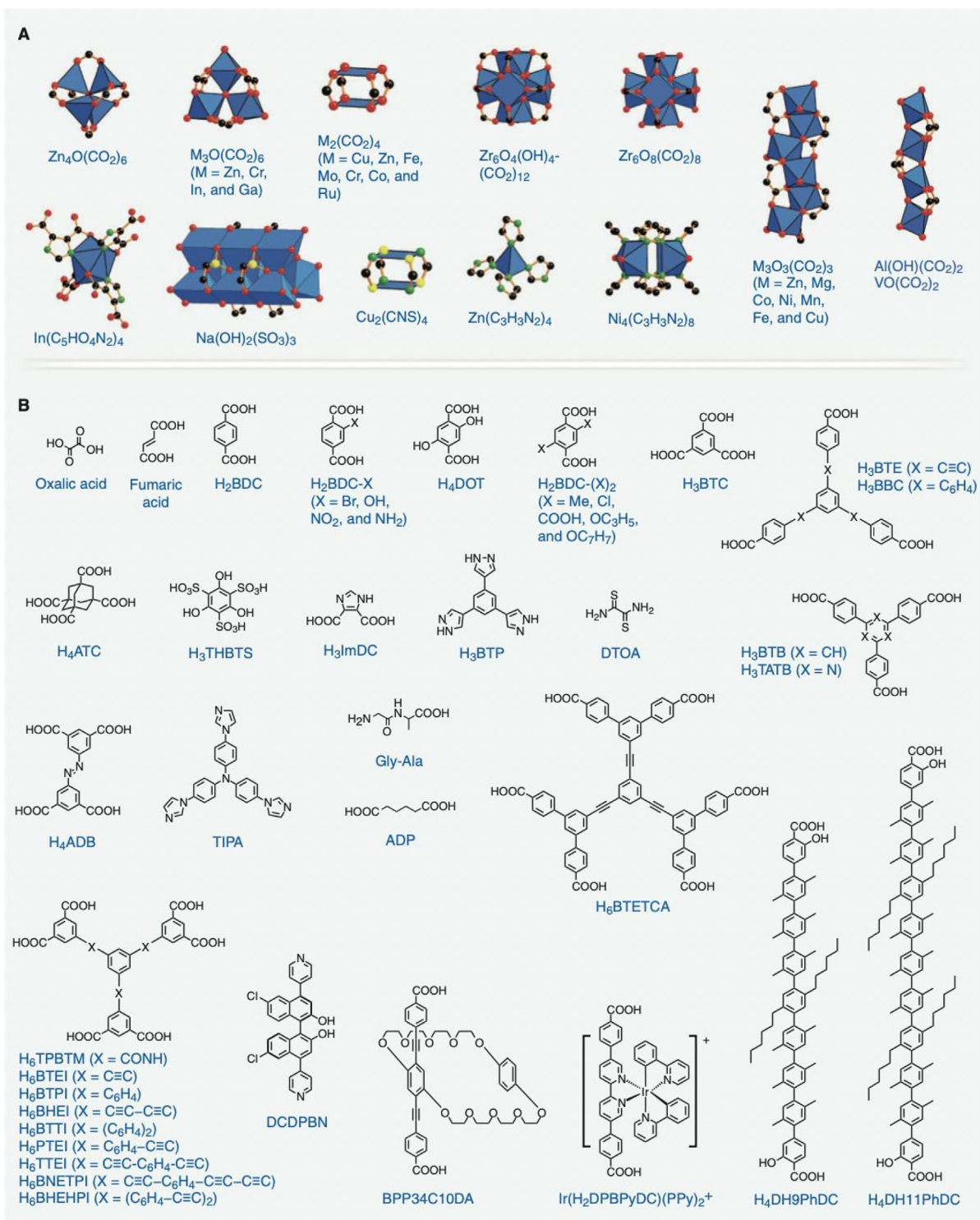


Fig. 1. Inorganic secondary building units (A) and organic linkers (B) of MOF. Ref. [34] with permission of the Science.

2004, 2D MOFs nanosheets have grasped the attention because of their overwhelming ultrathin thickness and high specific surface area feature [3,38]. Until now, 2D MOFs nanosheets have already been used in many usages, including gas separation, energy storage, and conversion, chemical sensing, catalysis, etc. [39]. Based on MOF's inborn advantages of high specific surface area and tunable porosity, which are decisive properties in catalysis, many researchers have devoted themselves to investigations since the 2000 s. However, as the field develops, there comes a significant

issue of thermal and chemical stability problems during practical utilizations. Healy et al. published the earliest review, which summarized the thermal decomposition temperature from a pile of MOF literature and proposed the decomposition mechanisms of various classes of MOFs [40]. As for chemical stability, ZIF-8, MIL-101, and UiO-66 are famous for their high chemical stability blessed by metals' inertness and the larger pore size properties. Ding et al. have summarized the approaches and applications of high chemical stability MOFs [41]. Furthermore, MOFs also have

been extensively applied to the precursors to obtain MOF-derived materials imposed by different heat treatment conditions, such as porous carbon and porous metal oxide [42]. The sacrifice of the expensive organic linkers would be a lethal drawback from an economic perspective. When it comes to practical implementation, MOF-derived materials have shown potential in diverse applications, for instance, energy storage and conversion [43,44], electrochemistry [45], and catalysis [46,47]. In contrast to MOFs, COFs are highly porous polymers with well-defined crystal structures expressed in either 2D or 3D and are connected by solid covalent bonds between light elements (such as H, B, C, N, and O) on their surface. A reversible condensation reaction is usually used to synthesize them. Hence, COFs can be viewed as MOFs with just a linker [48]. A great deal of attention has been paid to COFs since they were first reported by Yaghi et al. in 2005 [49]. Jiang and his coworkers 2009 demonstrated the potential of COFs as photocatalysts [50]. A COF (TFPT-COF) developed in 2014 by Stegbauer and colleagues can extract H₂ from water, opening the door to their application in H₂ generation and gaining worldwide attention [51]. In the same way as inorganic semiconductors, COFs are excited by light to achieve charge separation. Their bandgap (E_g) is directly proportional to the difference between HOMOs (highest occupied molecular orbitals) and LUMO (lowest unoccupied molecular orbitals) [52]. There are two ways that COF can transition electronically: $\sigma \rightarrow \sigma^*$ and $\pi \rightarrow \pi^*$. It is necessary to stimulate electron growth by ultraviolet light, while visible light is sufficient to stimulate electron growth by visible light [53]. Alternatively, using small molecules to fabricate COFs may allow them to be tunable in terms of porosity, surface groups, size, morphology, and so forth. Such high adjustability endows them with unlimited possibilities in photocatalysis. As a result, COFs may be applied to photocatalytic applications owing to the following five advantages: i) they can act as electron donors-acceptors, resulting in a reduction in the rate of recombination of photo-induced charges; ii) the periodic ordered cylindrical array of the π -conjugated system is conducive to electron delocalization, giving COFs outstanding electron transport performance and significant photoconductivity; iii) The spatial structure and energy levels of various molecular building blocks can be controlled; iv) Having a porous network structure allows them to possess a large specific surface area, enabling shorter charge transfer distances and more active sites; v) They have excellent chemical and physical stability due to their covalently bonded frame structure [54]. However, compared with other photocatalysts, the high cost and the low mechanical strength of COFs raw COF materials may hinder their applications. Scientists ignore their shortcomings, however, and continue to seek ways to develop COFs that will be low-cost and high-performance. Mainly, COFs are highly advantageous as electrocatalytic agents due to their unique structural character [55,56]. The periodic skeleton can be predesigned to target catalytically active sites, and COFs' tunable electronic structure allows them to be customized to improve electrocatalytic performance [57]. On the other hand, COFs have well-defined pores that allow ions to diffuse and active sites to be accessed. This results in a substantial improvement in energy conversion efficiency [58]. Lin et al. reported electrocatalytic CO₂ reduction in water using a metalloporphyrin-derived COF. Due to the interaction between the metal lattice and the COF lattice, the cobalt centers could have a more delocalized electronic structure due to the interaction between the metal and the COF lattice [55]. Thus, tunable molecules within the COF promote CO₂ reduction exceptionally efficiently and selectively with high activity. Researchers are primarily working on designing and synthesizing novel COFs for use as electrocatalysts at the molecular level [59,60]. However, they have a distinct microporous structure and lack any monolithic structure, which threatens to impede mass transportation during

heterogeneous catalysis, which leads to sluggish electrocatalytic activity, particularly for the gas reaction process [60–63]. While previous research has found that macroporosity in COFs can improve water oxidation mass transport by directly introducing them [61], the defects within the COFs and the boundaries between particles impede electron transport, resulting in bulk COFs being inherently less conductive and having limited electrocatalytic capabilities. Recent research has identified COFs as a novel class of photo absorber candidates for solar-driven H₂ evolution [64]. H₂ evolution has been catalyzed by various COFs as photocatalysts when sacrificial donors and co-catalysts are present [51,65,66]. A photoelectrochemical (PEC) approach may also be used to power solar-driven H₂ evolution (HER), with photogenerated electrons from the photo absorber driving the reaction [66–69]. The current bottleneck for PEC H₂ evolution using COFs as the photo absorber is the lack of practical solutions for fabricating COF thin films or heterojunction architectures that allow the photogenerated charge in COFs to be efficiently harvested. Photoelectrochemistry could provide a profound understanding of charge separation and charge extraction in photo absorbers [25]. Solvents have been used to prepare crystalline COF films and photoelectrodes [25], but controlling their morphology and thickness remains challenging. Several methods and their challenges were used in this work to show the recent developments in the synthesis and design of metal/covalent Organic Frameworks for hydrogen evolution strategies. These processes include steam and dry reforming reactions, water reduction, oxygen generation, and water splitting by photocatalysis, electrocatalysis, and photoelectrochemical processes.

2. Introduction of MOFs and MOF-derived materials

Metal-organic frameworks (MOFs), also recognized as porous coordination polymers (PCPs), were first published by Prof. O. M. Yaghi in 1995 [33]. Prof. Yaghi and his co-workers added Cu(NO₃)₂·2.5H₂O, 4,4'-bpy, and 1,3,5-triazine in deionized water and transferred them into a stainless bomb for the sequent heating process [33]. They successfully synthesized the Cu(4,4'-bpy)_{1.5}NO₃(H₂O)_{1.25} by hydrothermal method, and they called it the zeolite-like crystalline material which is the well-known metal-organic framework [33]. MOFs are varied by various arrangements comprising metal clusters or metal ions as nodes and organic ligands as linkers, shown in Fig. 1 [34]. With the efforts from many researchers all over the world, MOFs have already been potential platforms for diverse practical implementations, including gas separation and storage [70–73], CO₂ capture [74], drug delivery [75,76], chemical sensing [77–79], batteries, energy storage and conversion, and last but not least, catalysis [80–84]. In this section, we will discuss three important knowledge of MOF separately, divided into metal, organic, and framework according to the full name of MOF. To get a further investigation into the skeleton structure of MOFs, let's introduce metal first. The metal-containing components, also known as inorganic secondary building units (SBUs) and metal clusters, play the part of joints in the coordination of MOF. Bivalent and trivalent metals from 3d transition metals and 3p metals such as Zn, Cu, Ni, Co, Fe, Al, and Cr are the two major metallic groups used in MOF synthesis. Apart from this, relative minority of lanthanide-based MOFs are also synthesized [83]. By using the same metal cluster with different organic ligands, it is possible to synthesize isorecticular MOFs, namely Zn₄O(BDC)₃ (IRMOF-1), Zn₄O(NDC)₃ (IRMOF-8), Zn₄O(NHDC)₃ (IRMOF-11), and Zn₄O(BTB)₃ that connect nodes between nodes presents the organic ligands or organic linkers acting as the connecting bridges between node and node. There are various representative examples of organic ligands used in MOF synthesis

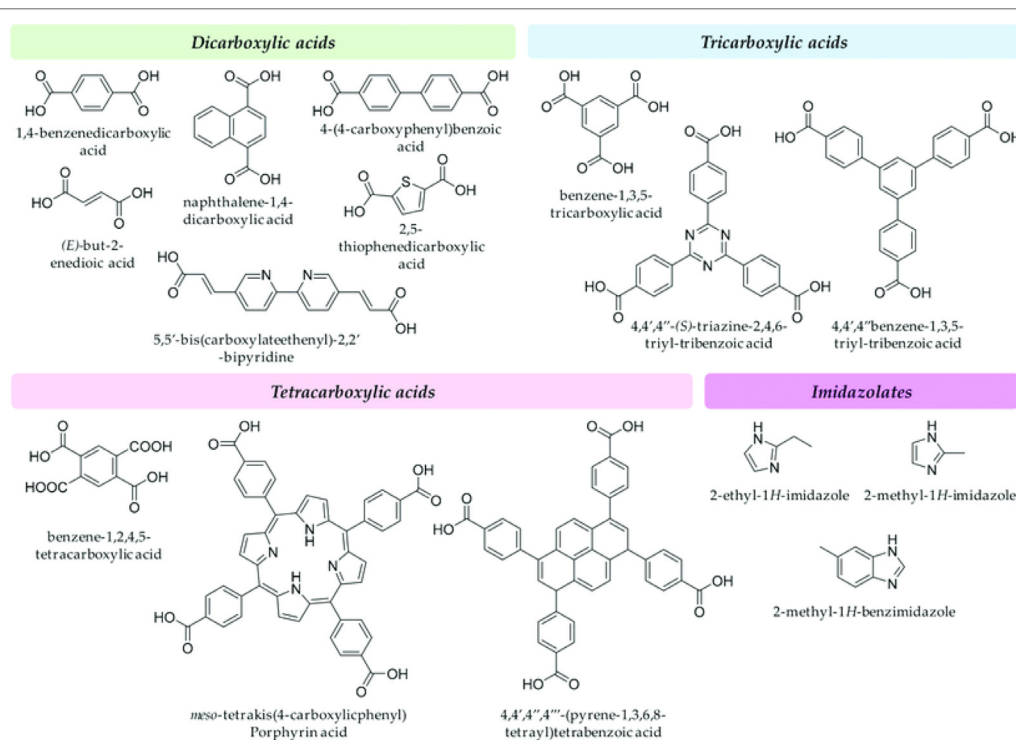


Fig. 2. Representative examples of organic ligands used in MOF synthesis. Ref. [85] with permission of the MDPI.

shown in Fig. 2 [85], which indicates that most of the organic ligands used in MOF synthesis contain more than two carboxylic acid sites and a minority of imidazolate, phosphonate, pyrazolate ligands [85]. Based on the number of anchoring sites, organic ligands are commonly classified as bidentate ligands, tridentate ligands, tetradentate ligands, and even polydentate ligands. For example, benzene-1,3,5-tricarboxylic acid (BTC) are a well-known tridentate ligand in MOF synthesis because there are three carboxylic acids in it. As the organic ligands acted as the connectors, it would also dominate the stability of the interaction between metal and ligands relied on the stable orbital overlaps. Additionally, there have been diverse researches emphasizing the decoration and the functionalization of organic ligands of MOF for to alternate properties of MOF, including the acidity/basicity, pore size distribution, specific surface area, affinity, adsorption, catalytic performance, etc [86]. Lastly, the summary, the framework combines the information from metals and organic ligands. As mentioned above, MOFs are periodically constructed with inorganic SBUs (metal clusters) and organic ligands. With different dimensional arrangements, MOFs could be assembled in either 2-dimensional and 3-dimensional structures. Since the discovery of graphene in 2004, 2D MOF nanosheets have grasped the attention because of their overwhelming ultrathin thickness and high specific surface area feature [87,88]. Until now, 2D MOF nanosheets have already been used in many usages, including gas separation, energy storage, and conversion, chemicals sensing, catalysis, etc. [39]. Healy et al. published the earliest review, which summarized the thermal decomposition temperature from a pile of MOF literature and proposed the decomposition mechanisms of various classes of MOFs [40]. As for the chemical stability, ZIF-8, MIL-101, and UiO-66 are famous for their high chemical stability blessing from the inertness of metals and the larger pore sizes. Ding et al. have summarized the approaches and applications of high chemical stability MOFs [41]. Furthermore, MOFs have been extensively applied to the precursors to obtain MOF-derived materials imposed by different heat treatment conditions such as porous

carbon and porous metal oxide [82]. To be more specific, MOF-derived porous carbon materials are fabricated under a high-temperature environment with an inert gas (nitrogen or argon). During the heating process, the organic ligands are carbonized, and the metals can be evaporated at high temperature, resulting in the formation of porous carbon material. Speaking of MOF-derived metal oxides, the materials are synthesized by calcination process under high-temperature and oxygen-contained condition. The MOF-derived materials I mention above feature high thermal and can the well-dispersion of abundant active sites [89,90]; however, the expense of organic ligands usually dominates MOF's profitability of MOF. The sacrifice of the expensive organic linkers would be a lethal drawback in economic perspective. When it comes to the practical implementation, the MOF-derived materials have been shown potential in diverse application, for instance, energy storage and conversion [43,44], electrochemistry [45], catalysis [47,90], and etc. In this review, we will concentrate on the applications of MOF and MOF-derived catalysts for gas phase hydrogen production. As far as we know, this is the first review to discuss this encouraging subject.

3. Synthetic approaches of MOF materials

Since Yaghi discovered the very first MOF by conventional solvothermal synthesis method in 1995 [33], there have been a great progress in the development of MOF synthesis over these three decades, namely, solvothermal synthesis, electrochemical synthesis, mechanochemical synthesis, microwave-assisted synthesis, and so no chemical synthesis in the order of times [91]. Besides, in the recent years, the trend of increased demands for MOFs has urged the researchers to develop a more efficient, economical, and continuous synthesis process to meet the future needs. There are more and more innovative synthetic methods have been discovered and investigated, such as spray dryer synthesis, supercritical synthesis, microfluidic synthesis, and etc. Instead

of rebuilding a whole new synthesis path, changing the several synthesis parameters including crystallinity temperature, reaction time, pH values, and solvent in order to optimize the production yield and the porosity properties is another crucial route for MOF synthesis investigation [92]. In this part, we will focus on the upsides and developments of each of the five main synthetic approaches of MOFs orderly: solvothermal synthesis, electrochemical synthesis, mechanochemical synthesis, microwave-assisted synthesis, and sonochemical synthesis.

3.1. Solvothermal synthesis

As the most conventional synthesis route, solvothermal synthesis, also known as high-throughput synthesis, is often operated in vials and tubes [93]. Consequently, this method is extensively used in labs for the purpose of synthesizing new materials and optimizing the synthesis properties. This method has also achieved the best crystallinity from XRD patterns and the best morphology from SEM/TEM images compared to the other methods [92]. In this approach, both the metal salts and the organic ligands are mixed in solvents and heated at the temperature above the boiling point of solvents for a duration of time ranging from hours to days. The common solvents includes *N,N*-dimethylformamide (DMF), methanol, ethanol, acetonitrile, and so on [94]. Apart from using the organic solvent mentioned above, hydrothermal synthesis is based on heating both metal precursors and the water [95]. To achieve the synthetic environment under high temperature and high pressure, the mixture has to be sealed in either bomb or autoclave.

3.2. Electrochemical synthesis

In 2005, HKUST-1 was the first successfully synthesized MOF by using electrochemical recipe by Mueller et al. from BASF [96]. Compared to the traditional solvothermal synthesis, it is superior owing to its easily-available reaction environment under room temperature and ambient atmosphere, high production yield, and simple operation requirements [97]. Moreover, the metals are introduced through anodic dissolution which can eliminate the contaminant, such as nitrate and chloride [98]. The electrochemical synthesis of MOF shows potential to the future scale-up industrial production process because of its continuous reaction and low energy consumption.

3.3. Mechanochemical synthesis

Although mechanical force is far from chemicals synthesis, the energy given from mechanical force provides the required energy to break molecular bonds under the microscopic scale. In 2006, the first microporous MOF which was $[\text{Cu}(\text{INA})_2]$ (INA = isonicotinic acid) was synthesized by solvent-free mechanochemical approach after grinding the metal salts and the organic ligands together for only 10 min [99]. Mechanochemical synthesis of MOF benefits its room temperature environment and the solvent-free condition, which are both environmentally-friendly advantages not only for the energy shortage problem but also for the green synthesis goal [100]. Mechanochemical synthesis of MOF has the potential to be the large-scale production method in the future [101]. Furthermore, to achieve the further greener and more sustainable future, there are researchers taking waste polyethylene terephthalate (PET) plastic as the precursors of MOF synthesis by mechanochemical approach [102].

3.4. Microwave-assisted synthesis

In 1946, the microwave technology was accidentally discovered by Percy Spencer when he stood in front of the active radar device

and the candy bar melted in his pocket [103]. With this unexpected surprise, scientists started to investigate the effect of microwave heating technology. Over the several decades, the energy from microwave irradiation has been developed mature in the organic chemical synthesis [104]. In 2005, Jhung et al. proposed the first synthesis of microwave-assisted MOF which is MIL-100 under 220 °C for 4 h [105]. The production yield is comparable to the traditional synthesis approach which expend the horizons for MOF synthesis. In summary, the microwave-assisted synthesis of MOFs features short synthesis time, high yield of desirable products instead of useless byproducts, fast crystallinity growth, precise nanostructure construction and so on [106].

3.5. Sonochemical synthesis

The sonochemical synthesis takes good use of the high-energy ultrasound with frequency above 20 kHz to trigger the acoustic cavitation [107]. The method is based on the phenomenon of the acoustic cavitation representing the sequential process of bubbles formation, growth, and the implosive collapse, which produce very high local temperatures of 500 °C, the pressures of 1000 atm and the heating and cooling rates of 10^{10} K/s via thermodynamic adiabatic processes [108]. In 2008, Qiu et al. successfully synthesized the first MOF which was $[\text{Zn}_3(\text{BTC})_2]$ by ultrasonic method. Compared to the solvothermal synthesis, the MOF is synthesized under 140 °C for 24 h [109]. By the comparison, it shows that the sonochemical synthesis features the shorter crystallinity time and milder thermal environment [110].

4. Covalent organic framework (COF)

4.1. Introduction and design skeleton structure of COFs

Chemistry is an essential subject in our life because by using this subject, new materials and structures with promising functions and properties can be efficiently designed and constructed. The primary purpose and target of chemistry are to prepare materials with highly defined structures [111]. In the polymer chemistry field, designing materials with well-ordered structures is still a challenging goal in the academic area. Recently, the synthesis and construction of polymers with well-defined order structures can be achieved by controlling factors such as regioregularity, chain sequence, molecular weight, stereoregularity, and end groups [112–114]. Crystal formation and monomer structure are essential in designing order structures in polymeric materials [115]. Furthermore, rigid building blocks and geometrically are most desirable because they can estimate the chain growth direction and leads to the structure formation with primary and high order range [116,117]. Metal-organic frameworks (MOFs), zeolites, conjugated microporous polymers (CMP), mesoporous carbons, mesoporous silica, and COFs are the main types of porous materials [118–134]. Zeolite materials are among the most stable compared to other porous materials, because of their lack of inherent functionality, variety, and poor porosity, they do not offer much potential for environmental applications [135]. MOFs have many accessible pores and are adaptable regarding chemical composition, functioning, and tuning [136]. They are frequently insufficient for practical use due to their limited stability. To overcome the disadvantages of these materials, COFs materials had extremely physical and chemical stability compared with MOFs. COFs are organic porous polymers and materials with high crystalline characteristics [135,137]. These emerging and interesting materials were prepared via network chemistry with diverse monomers containing light elements such as C, H, O, N, or B atoms) and they joined through the organic covalent bond to form 2D and 3D materials

[135,137]. Recently, COFs precursors have received much interest and attention in academic and industrial areas due to their amazing properties, including high thermal and chemical stabilities, unique molecular design, aligned polygonal pores, facile surface modification, and structural versatility, and high-order porosity [137–144]. In addition, COFs materials become excellent promising candidates in other practical implementations mass transport, energy storage and conversion, chemical sensing, luminescence, heterogeneous catalysis, drug delivery, molecular separation, Li batteries, oxygen and hydrogen evolution, gas storage and separation, and so on [135–144]. These applications come up as a result of distinctive properties for COFs materials such as inherent porosity, customizable pore structure, large surface area, flexible chemical combination, stimuli responsiveness, and biodegradability [135–144]. The high and primary order structure of COFs materials can be constructed and pre-designed using a topology diagram and step-growth poly-condensation reaction [135,137]. The combination of different monomers geometries can carry out the resulting COFs with different topology types [135,137]. The polygonal skeletons are the main unique property of COFs compared to other polymers and porous materials, which open the door and offer a great opportunity for designing and developing a new class of functional porous polymeric materials. Their shape, interface, environment, and pore diameters can be pre-established using post-synthetic functionalization or polycondensation reactions. Depending on the dimensional array of the hypothetical unit cell used to depict the crystalline framework, COFs are categorized as 2D or 3D [135,137]. Through dipolar molecular interactions or, in the particular instance of aromatic rings, π electron stacking, those planes are tightly packed to form the 3D shape of the actual synthetic material [137]. Different approaches are used to construct COFs with different topologies combinations (2D and 3D COFs) from various rigid units, as presented in Figs. 3 and 4 [137]. Firstly, 2D COFs are covalently 2D polymers that stretch in the x and y dimensions and aggregate in the z direction to form organized one-dimensional (1D) channels [135,137]. On the other hand, 3D COFs are prepared through a 3D growth of the polymer backbone with chain folding and overlapping [135,137]. Figs. 3 and 4 show a topology diagram for building polygons skeletons via the conjunction of building block units to form crystalline networks lattices in 2D or 3D COFs with intermittent placed knots and linkers. The combinations of different monomers' geometries lead to the construct of crystalline 2D COFs, as displayed in Fig. 3. Fig. 3 shows kagome, tetragonal, rhombic, tetragonal, and trigonal structures are the most polygons skeletons in 2D COFs materials. For example, using $[C_3 + C_3]$, $[C_2 + C_2 + C_2]$ or $[C_3 + C_2]$ geometry combinations lead to formation of hexagonal 2D COF. The C_3 -symmetric unit functions as a knot, whereas the C_2 -symmetric component functions as a linker. The backbones of C_3 -symmetric units are azatriphenylene, triphenyl triazine, triphenylene, phenyl, and triphenylbenzene, whereas the networks of C_2 -symmetric monomers are pyrene, bipyridine, porphyrin, biphenyl, phenyl, and anthracene. By using $[C_4 + C_4]$ or $[C_4 + C_2]$ topology diagram to construct tetragonal 2D COFs. Rhombic COFs have been created using the monomer combination $[C_2 + C_2]$, while Kagome COFs may be created using either a $[C_3 + C_2]$ or a $[C_2 + C_2]$ topological design. The outcome of the construction units forming a three-dimensional net is a 3D COF. The resulting polygonal pattern is defined by the -structure of the perpendicular assembly. The $[C_2 + C_2]$ topological strategy corresponds to one of two potential structures: a rhombic-shaped skeleton or a kagome structure. The development of 2D COFs with dense -units and micropores, required for the development of -stacked organic polymeric materials and porosities, has been accomplished utilizing a $C_6 + C_2$ network architecture scheme. This topology scheme permitted the building of triangular lattices with highly dense units and smaller

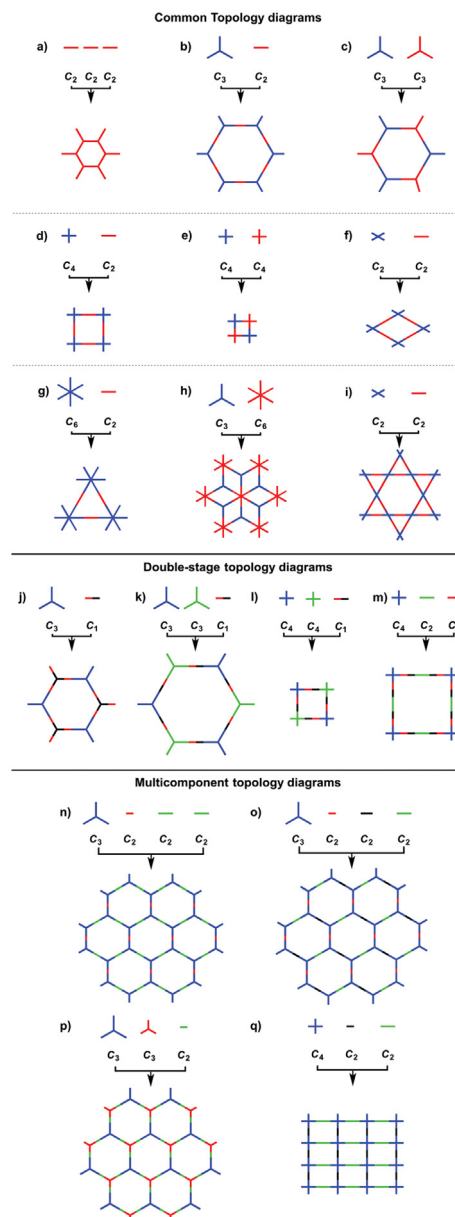


Fig. 3. Geometric illustrations demonstrate the fundamental building blocks for the development of (2D COFs Reproduced from Ref. [137] with permission of the Royal Chemical Society.

pores compared to all other topology diagrams. Generally speaking, a trigonal architecture is best for creating microporous COFs, but tetragonal and hexagonal morphologies help create mesopores. Interestingly, in a $[C_2 + C_2 + C_2]$ topology diagram, kagome-type COFs with triple pores have been built from a single knot with two linkers of differing lengths. COFs with dual-pore hexagonal structures are more likely to develop when asymmetric building blocks are condensed or when hydrogen bonds are added to the COF skeleton [137]. The trigonal topology diagram is likely $[C_6 + C_2]$ or $[C_3 + C_2]$. The knot location is located by the C_6 -symmetric unit, whereas the C_2 -symmetric moiety occupies the linked site. hexa-substituted backbones, including hexaphenylbenzene or hexabenzocoronene, are common for C_6 -symmetric units. In contrast, the C_3 -symmetric monomers for the $[C_3 + C_2]$ combination are commonly hexa-substituted triphenylene and hexaazatriphenylene counterparts, which result in a trigonal skeleton with two distinct pore diameters. To create 3D COFs, a knot with

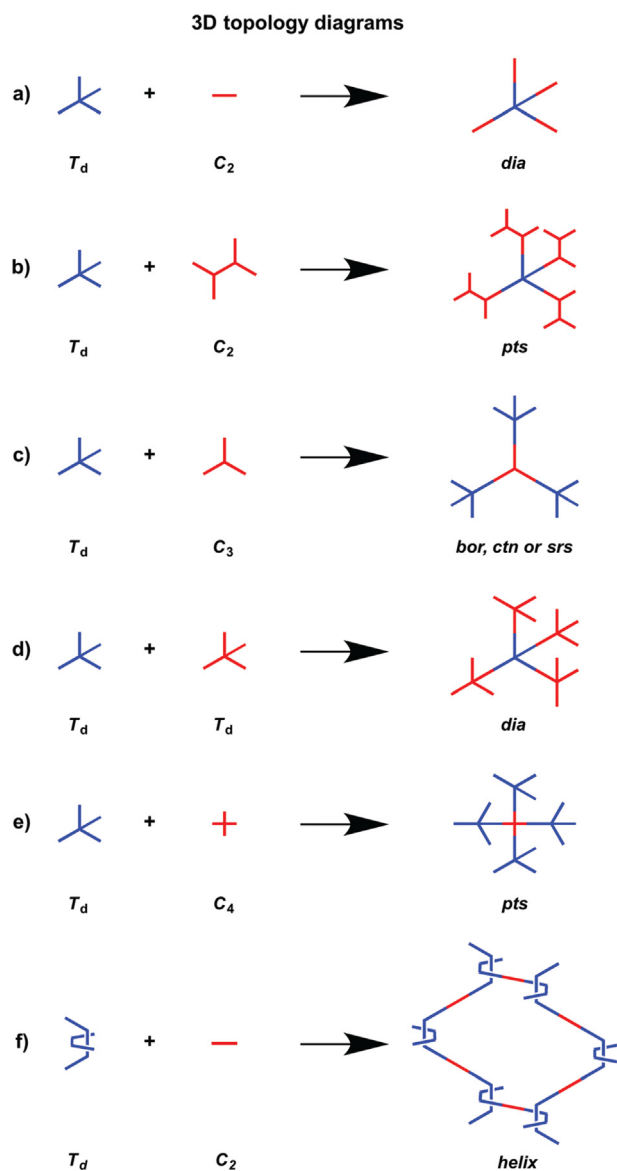


Fig. 4. Geometric illustrations demonstrate the fundamental building blocks for the development of 3D COFs Reproduced from Ref. [137] with permission of the Royal Chemical Society.

T_d or orthogonal symmetrical is necessary to guarantee the 3D development of the polymer backbone. Different topologies, such as *bor*, *ctn*, *dia*, *rra*, *srs*, *cff*, and *pts* nets, have been developed into 3D COFs [Fig. 4]. The common knot compounds, such as tetra(4-dihydroxyborylphenyl)methane (TBPM), tetra(4-dihydroxyborylphenyl)silane (TBPS), tetrakis(4-aminophenyl)methane (TAPM), 1,3,5,7-tetraaminoadamantane (TAA), tetrakis(4-formylphenyl) (TASP). Designing 3D COFs with *ctn* and *bor* networks utilizing [$T_d + C_3$] is possible [145]. T_d -symmetric units like tetra(4-dihydroxyborylphenyl)methane (TBPM) or TBPS tetra(4-dihydroxyborylphenyl)silane (TBPS) that self-condensate or co-condensate with a C_3 -symmetric linker produce 3D COFs with a *ctn* net, whereas TBPS that undergoes the same process produces a *bor* net. Due to the absence of interpenetration, the resultant COFs have a significant surface area and a low density. The [$T_d + C_2$] diagram can create a *dia* network with the greatest number of 3D COFs because of the variety of C_2 -symmetric monomers [146–152]. The [$T_d + C_4$] or [$T_d + C_2$] diagram have been used to construct the *pts* net; however, the C_2 - and C_4 -symmetric subunits need four reactive

functional groups to generate 3D COFs with twofold different interpenetration [151–153]. Additionally, the [$T_d + C_3$] conjunction may result in a *srs* net [135,137].

5. Synthetic approaches of COF materials

In contrast to typical polymers, COFs have unique compositions, uniformities, pore size, and geometries, making their production more difficult. A mixture of research fields, including dynamic/reversible bonding, topochemical polymerization, chemical synthesis, and reticular assembly, is necessary for effective COF creation, making the production of a rationally designed COF with specified features still challenging [135,137]. The key to the synthesis is figuring out how to balance these two forces throughout the reaction to produce a crystalline porous structure. The synthesis of COFs has been made possible via a variety of polycondensations; both reversible and non-reversible processes involving >10 different links have demonstrated success in this regard. In contrast to bulk processes, COFs have also been created synthetically using various techniques and on a range of substrates, providing a variety of application-specific morphologies. After Yaghi's group published the first COF in 2005 [49], other papers showed various methods for synthesizing COFs. COFs have been created using a variety of organic covalent linkers, including imide, boronic ester, boroxine, azine, triazine, sp^2 -carbon, hydrazone, b-ketonamine, imine, and phenazine [17]. In this part, we list and discuss the techniques employed to create COFs, such as ultrasonication, mechanochemical, condensation, ionothermal, multicomponent, microwave-assisted, and light-induced processes. As known that different physicochemical features of COFs are produced by controlling the pore structure and choosing the different linkers.

5.1. Solvothermal synthesis

In this approach, a blend of monomers mixed in several carefully selected solvents is heated at 100–120 °C in a closed Pyrex tube for 3–5 days. To raise the dissolution of the monomers, solvent selection is essential. The spread of the molecules into the solution can be mediated by solvent mixes (for instance, 1-butanol/dichlorobenzene or 1,4-dioxane/mesitylene in the presence of acetic acid), which will hasten the nucleation of COFs. Additionally, the enclosed atmosphere ensures water is accessible throughout the process, enhancing the COFs' ability to crystallize. To achieve high crystallinity and porosity of COFs materials in this method, the reaction parameters including the medium, temperature, catalyst, and modulator must be fine-tuned. Two COFs (COF-1 and COF-5) were first reported by Yaghi *et al* [49]. Fang *et al* prepared a 3D-COF named JUC-564 with *stp* topology and high BET surface area and big pore size during the solvothermal method through the reaction of 1,3,6,8-tetrakis(4-aminophenyl)pyrene (TAPPy) and 2,3,6,7,14,15-hexakis(4'-formylphenyl)tritycene (HFPTP) [154]. Interestingly, 3D-CageCOF-1 with the *acs* structure through the condensation reaction of Cage-6-NH₂ as D_{3h} symmetry linear 2,5-dihydroxyterephthalaldehyde [59]. Furthermore, He *et al* prepared 3D-ceq-COF through the Schiff base reaction between 2,3,6,7,14,15-hexa(4-formylphenyl)tritycene (HFPTP) and (b) 1,3,5-tris(4-aminophenyl)triazine (TAPT) [155]. The JUC-569 with *acs* topology was constructed by condensation reaction [6 + 6] of 2,3,6,7,14,15-hexa(4'-formylphenyl)tritycene (HFPTP) and 2,3,6,7,14,15-hexa(3',5'-diisopropyl-4'-amino)tritycene (HDIATP) act as symmetrical triangular prism node [156]. Wang *et al* prepared 3D-TPB-COF with *pts* net, and 3D-TPB-COFFh with *ljh* topology [157]. Peng *et al* prepared two types of 2D *sql* COF and 3D *pts* COF through the reaction of hexaldehyde phenyl benzene (HFB) with tetrakis(4-aminophenyl)ethane (TPE-NH₂) or

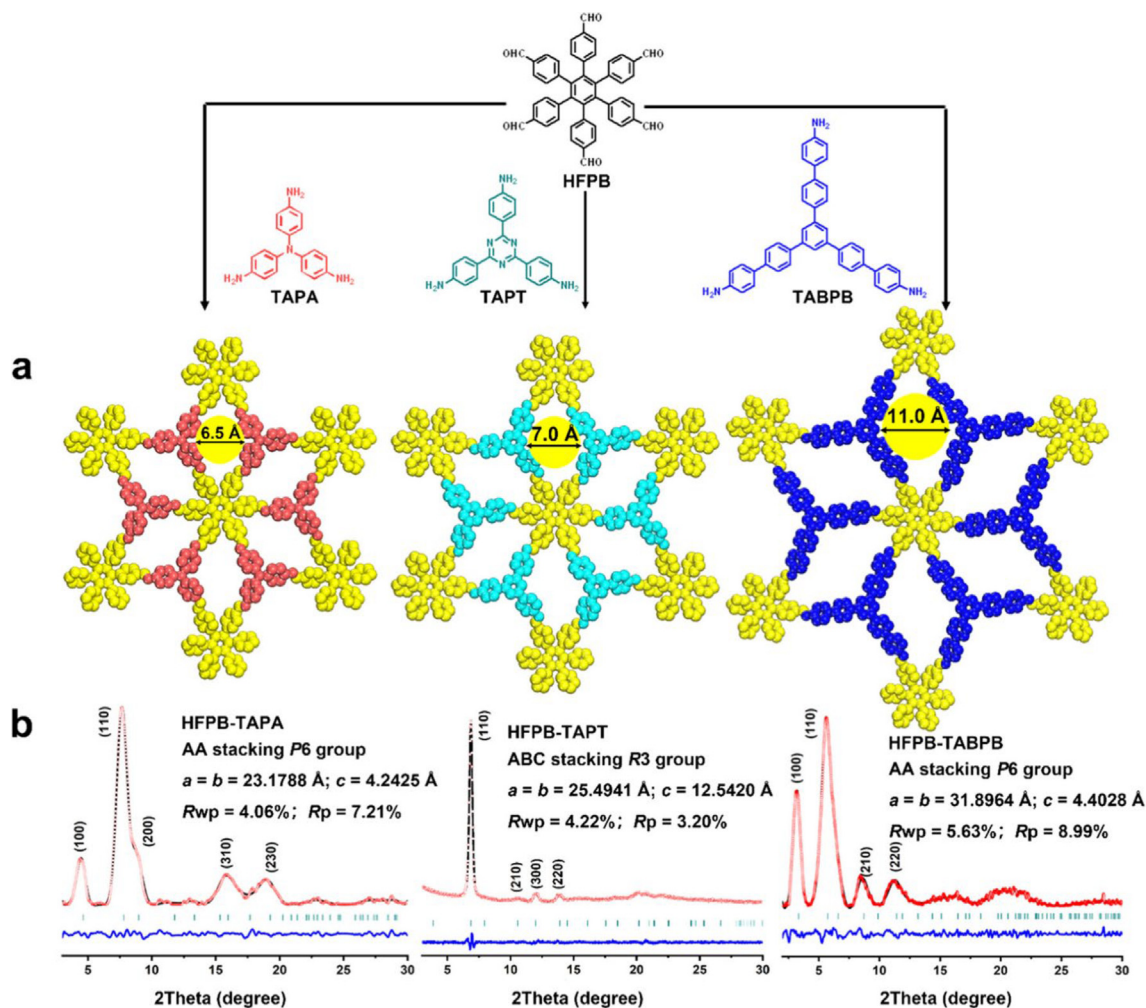


Fig. 5. (a) Synthesis and (b) XRD patterns of HFPB-TAPA, HFPB-TAPT, and HFPB-TABPB COFs. Reproduced from Ref. [160] with permission of the American Chemical Society.

3,3',5,5'-tetra(p-aminophenyl)-bimesitylene (BMTA) [158]. Interestingly, the 3D pcb COFs were constructed by traditional Schiff-base reaction of 5,10,15,20-tetra(4-aminophenyl)-porphyrin (TTEP) 8-connected building block with 1,4-diaminobenzene [159]. Zhang *et al.* prepared 2D HFPB – TAPA, HFPB – TAPT, and HFPB – TABPB COF with tunable pore size and kgd Topology the reaction of hexa(4-formylphenyl)-benzene (HFPB), with tris(4-aminophenyl)amine (TAPA) or tris(4-aminophenyl)triazine (TAPT), and 1,3,5-tris[4-amino(1,1-biphenyl-4-yl)]benzene (TABPB), as building units, as presented in Fig. 5 [160].

5.2. Mechanochemical synthesis

In this approach, manual grinding simply using a pestle and a mortar is gaining popularity since it is an easy, quick, solvent-free, and ecologically friendly process done at room temperature [161]. For example, Banerjee's group [162] used the mechanochemical method (MC) to prepare low porosity and crystallinity and high stability of three COFs materials in strong base, strong acid, and boiling water (TpBD, TpPa-1, and TpPa-2), as shown in Fig. 6. The same group revealed that the crystallinity of resulting COFs increased by adding liquid during the grinding method [163]. Also, Wang and his group constructed high porosity, sheet structures, and excellent thermal stability of TpAzo COF in 20

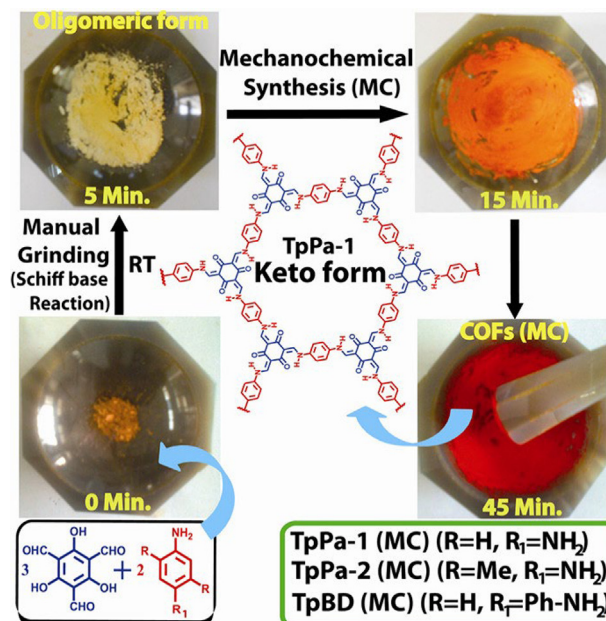


Fig. 6. Synthesis of TpPa-1, TpPa-2, and TpBD via MC grinding using a mortar and pestle. Reproduced from Ref. [162] with permission of the American Chemical Society.

mins using the MC method through condensation of Tp and 4,4'-azodianiline monomers [164].

5.3. Sonochemical synthesis

The sonochemical method is a different strategy besides solvothermal synthesis for COFs construction with a short time, large-scale synthesis, and high surface area [165]. In this approach, ultrasound is used to speed up the crystallization process by causing acoustic cavitation, which causes bubbles in solution to develop and burst, which is a reaction system [165]. For example, this method was employed by Ahn *et al.* to prepare both COF-1 and COF-5 in a short time (1 h), and they found that the obtained COF-5 had a high surface area (2122 m²/g) [166].

5.4. Microwave synthesis

A lot of research has been done on microwave irradiation as a different way to make COFs. Compared with the solvothermal method, microwave irradiation has a lot of advantages, including cleaner materials, quicker reaction times, and the ability to monitor phase behavior while dynamically controlling temperature and pressure [167]. Additionally, the microwave procedure allows for increased surface area by eliminating pollutants that have become trapped in COF pores. The various COFs materials with imine, and ketoenamine linkages prepared through microwave irradiation [168,169].

5.5. Light-induced synthesis

In 2019, Choi *et al.* [170] prepared and constructed crystalline hcc-COF that had an extended conjugated structure and high electrical conductivity of $2.22 \times 10^{-3} \text{ S m}^{-1}$ through the reaction of 1,2,4,5-benzenetetramine tetrahydrochloride (BTA) and hexaketocyclohexane octahydrate (HCH) in acetic acid and water under the simulated sunlight irradiation with wavelength at 200–2500 nm.

5.6. Vapor-assisted synthesis

Liu *et al.* prepared uniform nanofibrous-like structures of COFs through the reaction of 2,6-dihydroxynaphthalene-1,5-dicarbaldehyde (DHNDA) and 2,4,6-tris(4-aminophenyl)pyridine (TAPP) using a vapor-assisted solid-state approach [171]. Furthermore, BDT-COF and COF-5 film was prepared using this method [172]. For more details, the monomers are dissolved in a polar solvent, and the resulting mixture is drop-cast onto a glass substrate. The reaction solvent-filled vessel in the desiccator is immediately filled with the substrate, and the desiccator is sealed at room temperature. Finally, a COF layer is applied to the glass substrate for three days.

5.7. Interfacial synthesis

Free-standing polymer thin films have been successfully constructed at the gas-liquid and liquid-liquid interfaces [173,174]. For example, Fig. 7 showed the synthesis of 2D Imine-based Tp-Tta, Tp-Ttba, Tp-Bpy, and Tp-Azo by using an interfacial approach

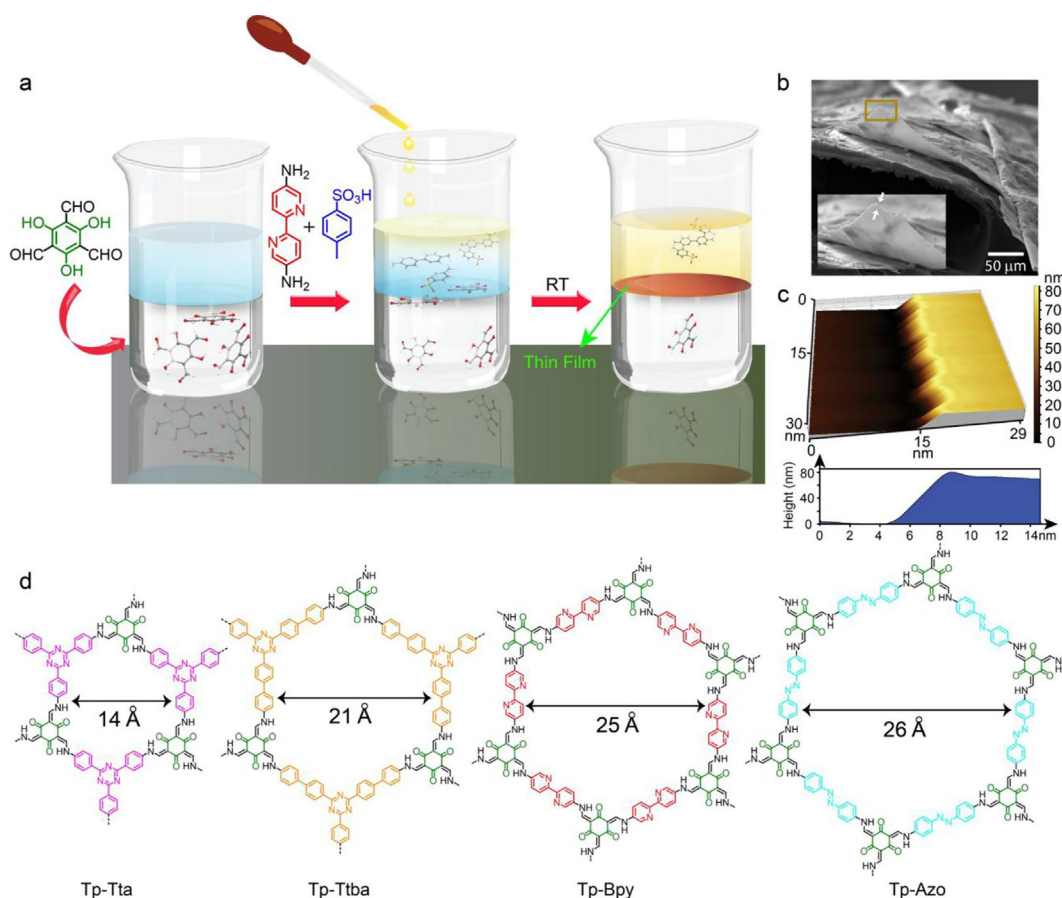


Fig. 7. Schematic of interfacial polymerization for the synthesis of thin films of Tp-Tta, Tp-Ttba, Tp-Bpy, and Tp-Azo. Reproduced from Ref. [175] with permission of the American Chemical Society.

between DCM and water Tp is soluble in DCM, and both PTSA and amine are dissolved in water or water/acetonitrile mixture [175]. Also, the synthesis of COF-TTA-DHTA film with thickness from 4 to 150 nm was done through immersion of an aqueous solution of 4,4,4-(1,3,5-triazine-2,4,6-triyl)trianiline (TTA), acetic acid, and Sc(OTf)₃ in 2,5-dihydroxyterthaldehyde (DHTA) [174]. Furthermore, A 2D COF monolayer was constructed via Langmuir-Blodgett (LB) method by Schiff base condensation reaction of the aromatic tetraamine and dialdehyde monomers at the air-water interface [176]. To prepare COFs, hybrid materials could be achieved through the integration of COFs materials onto the surface of metal-organic framework (MOF) and Fe₃O₄ nanoparticles [177,178]. The synthesis of few-layer 2D polymer crystallites with several micrometer sizes such as 2DPI was successfully done by using another strategy called a surfactant-monolayer-assisted interfacial method [179].

5.8. Post-Synthetic COF modifications

It is imperative to identify and regulate important COF aspects, including the inner structure and intrapore chemical behavior as the typical COF implementations entail the connections of exterior substances with the outer and interior interfaces of the intrapore and pore zones. COF modifications may be added before, after, or in place of synthesis. Before the material is synthesized, pre-synthetic alterations involve adding the right functional groups to the frameworks. The need to ensure the functional groups stability under-responsive circumstances and prevent them from obstructing the COF crystallization process, which might be difficult based on the functional groups. Substrates interacting with the developing COF and directly obstructing crystallization are the mainstay of in situ alterations. These structures serve as an anchor by being present throughout the early development phases, which enables the COF to polymerize surrounding them and produce a composite material that may be either organic or inorganic, based on the host. When compared to other polymer classes, COFs have the benefit of allowing for further functionalization processes even after they have been created. Due to inadequate solvent and reagent availability to the active reaction locations and constrained mass transfer mechanisms, post-synthesis reactions are challenging in non-porous polymer architectures. However, long porous networks and large surface areas in COFs give the majority of the solid preferential access to solvent and reagents, enabling simple post-functionalization, incredibly adaptable for various applications. The first phase is adding reactive sites in the initial monomers to accomplish a covalent post-synthetic functionalization. The COF must have sufficient chemical stability under the new post-synthetic reaction circumstances, which may ultimately lead to a challenging balance (boroxine or boronic ester type COFs, particularly susceptible to hydrolysis, making them extremely unstable in aqueous solutions). The functionalization procedure begins with the preparation of the COF and involves a heterogeneous reaction. The reaction must be advantageous, good yielding, and produce the fewest byproducts as possible. Additionally, COFs have a unique quality known as post-synthetic modification that has led to the classification of this class as both products and initial reagents for organic synthesis. Click reactions catalyzed by Cu(I) are another popular method for post-synthetic functionalization. Alkynyl groups are found in the structures of the monomers used. During the COF synthesis, alkynyl groups are not reactive; nevertheless, they are later activated, enabling addition reactions. The COF reacts with an organic azide with Cu(I), to generate a cycloaddition reaction that yields a heterocyclic 5-atom ring with the desired functional group. The incorporation of various functional compounds, like ethyl, acetate, hydroxyl, carboxyl, or amine groups, is made possible by click reactions, which can typically

be carried out under a moderate reacting environment and have a reasonable rate of yielding products. For introducing carboxylic groups (COOH) into COFs materials, for example, ring-opening reactions utilizing succinic anhydride are an alternative post-synthetic method. Constructed COFs When succinic anhydride is used to treat polymers made from monomers having OH functional groups, the hydroxyl groups react to form an ester and carboxylic acid groups. The post-synthetic functionalization of these groups is even more important since the existence of acidic groups might be potentially unfavorable to the normal COF crystallization mechanism. Adding amine groups to COF porous structure has also been investigated for various uses. The development and growth of COFs, notably imine or ketoenamine-type COFs, are typically hampered by the existence of such amine groups in COF preparation because they alter the projected symmetric structure. Utilizing monomers with nitro groups and using metal catalysts to convert them to NH₂ groups after producing the COF is a workable option. Since NH₂ groups may eventually serve as the reaction sites for further functionalization, treating the COF with SnCl₂ makes it simple to produce amine-functionalized COFs. The introduction of different groups such as quaternary amines, amidoxime, thiol, ether, and amide into COFs walls precursors have been reported through chemical conversion. Imine-based COFs can be modified to amide-base frameworks by oxidation reaction in the presence of 2-methylbut-2-ene, and sodium chlorite in a mixture of dioxane and AcOH. To synthesis of thiazole-type COFs through combing with sulfur; to benzoxazole-type COFs, by reaction with 2,5-diaminehydroquinone with water, DMF, and molecular oxygen. Yagi and his workers constructed ester-linked COF termed COF-120 and COF-121 with high surface area up to 2092 m²/g and hcb topologies by the reaction of 1,3,5-tris(4 hydroxyphenyl)benzene (THPB) with DPT and di(pyridin-2-yl) [1,1'-biphenyl]-4,4'-dicarboxylate (DPBP), respectively [180]. Cui and his group used Knoevenagel polycondensation of chiral tetrabenzaldehyde of dibinaphthyl-22-crown-6 with 1,4-phenylenediacetonitrile or 4,4'-biphenyldiacetonitrile to produce CCOF 17 and 18, respectively. Then, they prepared CCOF 17 and 18 with excellent stability in both base and acid medium and crystallinity through the reduction reaction of CCOF 17 and 18 in the presence of NaBH₄ and isopropyl alcohol for 7 days [181]. Zhao and his group prepared seven crystalline amide COFs through the oxidation of imine-linked frameworks with KHSO₅ as an oxidant under facile conditions and short time reaction (7 h) [182].

5.9. Multicomponent reactions method

Due to their distinctively sustainable features, MCRs have recently attracted enormous interest in creating a wide range of synthetic pathways to create COFs materials [183]. The MCRs approach has a lot of advantages in contrast to stop-and-go syntheses, such as facile workup processes, bond, step efficiency, high yield of the final product, reducing the time transformation, reducing the reaction steps, environmentally friendly media, and operational friendliness [184–186]. The MCRs reaction types include Povarov, Asinger, Debus–Radziszewski, Groebke–Blackburn–Bien aymé, Gewald, Mannich, Petasis, Strecker, and Ugi reactions [183]. Wang *et al.* [187] prepared imidazole-linked COFs through Debus–Radziszewski reaction by the condensation reaction of tert-butylpyrene tetraone, aromatic aldehyde in the presence of NH₄OAc, mesitylene, and dioxane for 5 days at 150 °C [Fig. 8]. Dong *et al.* [188] constructed crystalline COFs materials through the Povarov reaction of TAPB, DMTPA, and styrene in the presence both of BF₃OEt₂, and DDQ (Fig. 9). The ultrastable pyrimidazole-based COFs have been prepared through the Groebke–Blackburn–Bien aymé (GBB) reaction between aminopyridine, isocyanide, and aldehyde for 5 days at 120 °C, as presented in Fig. 10 [189]. Dong and

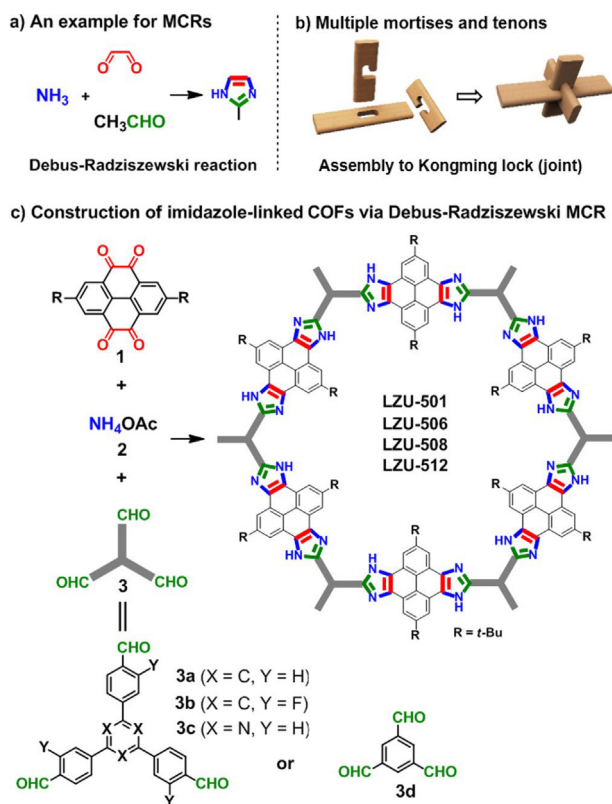


Fig. 8. Construction of imidazole-linked COFs via Debus-Radziszewski reaction. Reproduced from Ref. [187] with permission of the American Chemical Society.

coworkers [190] successfully prepared (R)-DTP-COF and (S)-DTP-COF with good yield using prochiral monomers (1,3,5-tris(4-amino phenyl)benzene (TAPB), 2,5-dimethoxyterephthaldehyde (DMTP), and phenylacetylene (PA)) in the presence chiral catalyst CuOTf-toluene/(R, R)-pybox and CuOTf-toluene/(S, S)-pybox, respectively [Fig. 11]. Cooper et al. [191] prepared Crystalline and ultrastable thiazole-linked COFs (TZ-COF1) were constructed through the free metal reaction of sulfur (S), naphthalene-

2,6-diamine, and 4,4,4'-(1,3,5-triazine-2,4,6-triyl)tribenzaldehyde in DMSO and AcOH. The obtained TZ-COF-1 had a higher surface area up to 1522 m²/g than the obtained TZ-COF-1 (1522 m²/g) by the two-step method [Fig. 12].

6. Hydrogen

In 2015, united nations (UN) proclaimed “Transforming our world: the 2030 Agenda for Sustainable development” which is a wake-up call for all the humankind to re-emphasize the importance of the ability to meet the present and future needs at the same time during our economic growth [192]. At the heart are the 17 sustainable development goals (SDGs), we could learn that the demand for environmentally friendly alternative energy is in an urgent need. As the demands for energy have escalated since the industrial revolution, more and more researchers dedicated themselves to investigate the abundant, sustainable, secure green energy for the future supply. Different from the conventional fuel, such as coal and natural gas, which generate the hazardous pollutants during the reaction, there is no greenhouse gases production but only water left after the combustion of hydrogen. Despite of the fact that hydrogen produces less contaminant than the conventional fuels, the energy density of hydrogen (142 MJ kg⁻¹) is much larger than either diesel fuel (45.5 MJ kg⁻¹) or gasoline (45.8 MJ kg⁻¹) [193]. Thereby hydrogen behaves as the most available sustainable energy in the future. Although hydrogen itself is colorless, it is commonly categorized by different colors to represent the production path and how clean it is. Nowadays, most of the hydrogen is produced from fossil oil, which is exceedingly environmentally unfriendly attributing the greenhouse gases formation. Brown hydrogen is carried out under the process of coal gasification to produce syn gas, which is a main-stream hydrogen production process during 19th century. With the process of the times, hydrogen production from steam reforming process, categorized as grey hydrogen, becomes dominate nowadays because of its economical efficient and large-scale production. To overcome the emissions of greenhouse gases contributing to global climate change, scientists subsequently emphasized on the blue hydrogen featuring the extra carbon capture and storage after the previous brown and grey hydrogen production. However, as the trend of reducing the carbon footprint, the fact of CO₂ emission

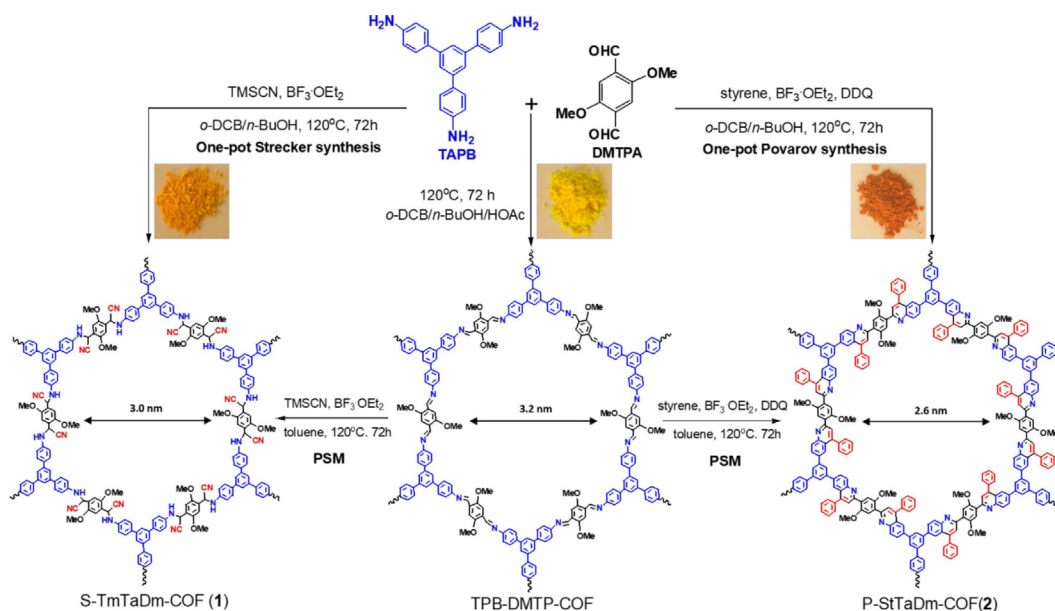


Fig. 9. Synthesis of TPB-DMTP-CMP, S-TmTaDm-COF and P-StTaDm-COF. Reproduced from Ref. [188] with permission of the American Chemical Society.

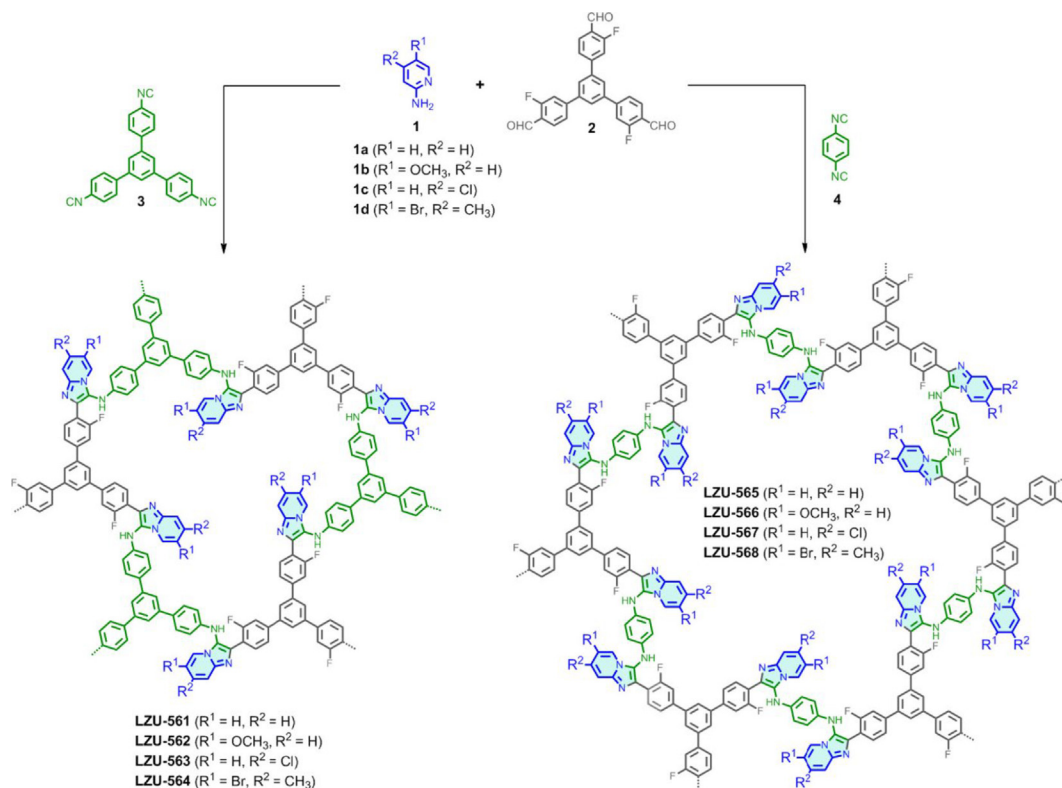


Fig. 10. Synthesis of Pyrimidazole-Based COFs. Reproduced from Ref. [189] with permission of the American Chemical Society.

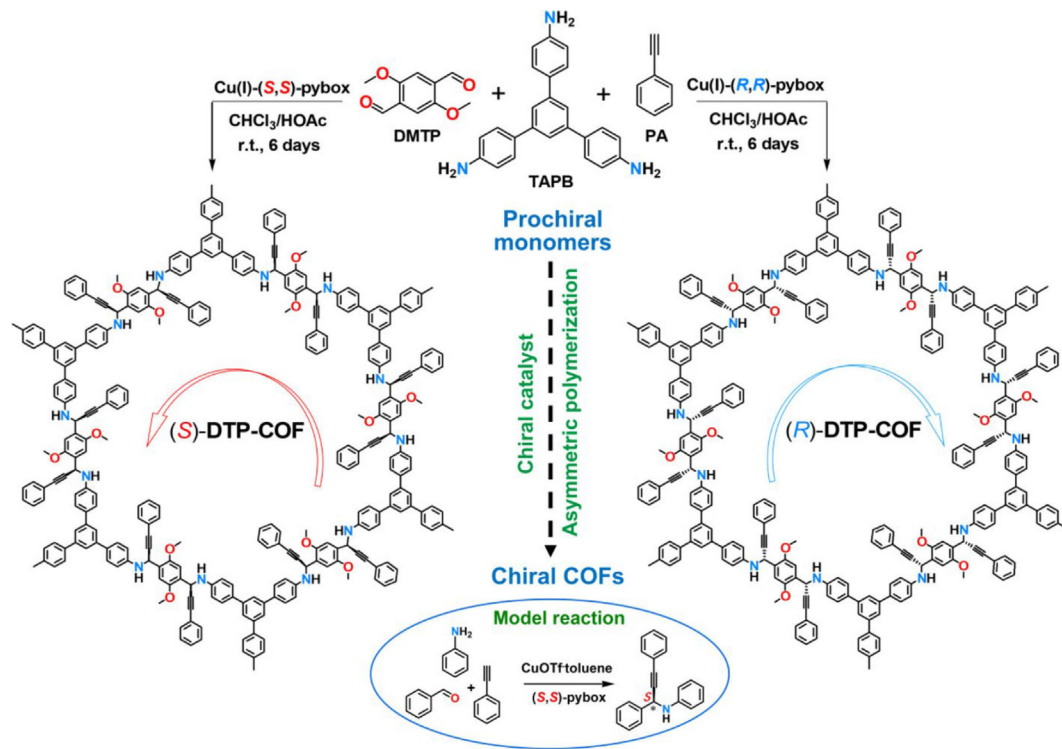


Fig. 11. Synthesis of (S)- and (R)-DTP-COFs via catalytic asymmetric polymerization. Reproduced from Ref. [190] with permission of the American Chemical Society.

becomes a critical defect for the ideal zero-emission green hydrogen. Therefore, to fulfill the ultimate goal of producing clean hydrogen energy, the development of green hydrogen is a promising path in the near future. Green hydrogen is directly produced and collected on the cathode through the electrolysis of water. The electricity

required during the process have to be generated from renewable energy sources, such as wind, solar, hydro, biomass, geothermal energy, etc. [194]. Although low-carbon alternative energy namely wind and solar power are used in practice, many people see the resource inconsistency as Achille' heel which indicates that some of

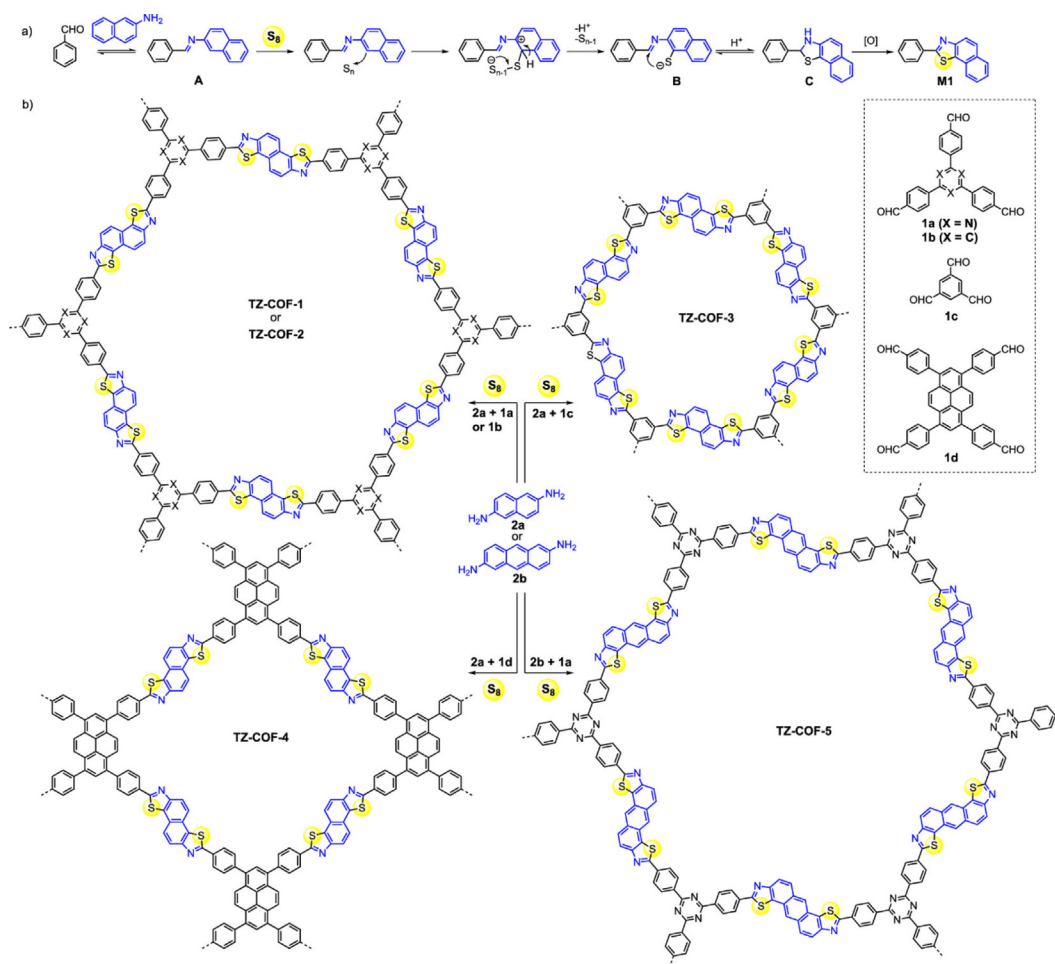


Fig. 12. Construction of thiazole-linked COFs by a Multicomponent Reaction. Reproduced from Ref. [191] with permission of the American Chemical Society.

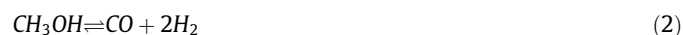
the renewable energy is limited by the weather requirements. Therefore, the energy storage plays an essential enabler during the energy transition period. Nowadays, there are a variety of types of energy storage technologies, including mechanical, electrical, biological, chemical energy storage, etc. [195]. Among all, pumped-storage hydroelectricity categorized in mechanical energy storage is the most widely used technique. The energy is stored in the form of gravitational potential energy from low elevation to high elevation during the off-peak power period, and the electricity is generated when the water is released through the turbines [196]. Besides, power-to-gas (PtG) technique has received increasing attention in the recent years [197]. It is a technique to take use of the excess electrical energy to electrolyze water leading to producing hydrogen and oxygen and deposit the gas-phase or liquid-phase hydrogen for energy storage. Yet, when the energy is relatively scarce, the reverse direction of power-to-gas processes would be operated to generate the energy. The hydrogen energy from reverse-PtG processes have been economically feasible in areas where renewable energy accounts for a large proportion calculating by the profit models, which indicates that power-to-gas technique has a bright prospect for the future energy storage [198].

6.1. Hydrogen production by using MOFs and MOF-derived catalysts

6.1.1. Hydrogen production from steam reforming reaction

There are a variety of original reactants used in steam reforming reaction, including natural gas, methanol, ethanol, etc. However, among all the studies, methanol has been most widely used in

hydrogen production through methanol steam reforming (MSR) by using MOF and MOF-derived catalysts [199–202]. To understand the reaction thoroughly, taking a glance on the reaction equation is indispensable. Shown below, the overall MSR process (Eq. (1)) consists of two sequential reactions: methanol decomposition (Eq. (2)) and water–gas shift (WGS) (Eq. (3)) [203].



Practically, the product of the overall MSR is a mixture of hydrogen, carbon dioxide, a minority of carbon monoxide, and some unreacted reactants. However, as the desired hydrogen product is produced, carbon monoxide can act as a poison for the anode of the hydrogen fuel cell at low temperatures [204]. Thus, the catalyst of MSR plays an essential part in simultaneously increasing the hydrogen selectivity and decreasing the selectivity of carbon monoxide compared with carbon dioxide. Moreover, the thermodynamics behind the MSR process is essential to be mentioned because it will be closely related to not only the reaction temperature during the process but also the reaction selectivity during different competitive conditions. The overall MSR process is an endothermic reaction based on the standard enthalpy is + 49.4 kJ mol⁻¹, which can be viewed as the addition of the enthalpy of methanol decomposition (+92.0 kJ mol⁻¹) and WGS process (-42.6 kJ mol⁻¹) [205,206]. However, side reactions referred to as

Table 1
Summary of MOF-derived catalysts applied for steam reforming reactions.

Entry	Catalyst	MOF/MOF precursor	Reactant	Reactant conversion	H ₂ selectivity	CO selectivity	Reaction condition	Stability	Ref.
1	Pt-SnO@MIL-101(Cr)	MIL-101(Cr)	methanol	92 %	89 %	3.4 %	300 °C, 1 atm, N ₂ /H ₂ O/CH ₃ OH 1:2:1 M ratio, WHSV = 1.8 h ⁻¹	300 °C, 30 h	[199]
2	Pd/Al ₂ O ₃ (A)	A520 MOF(Al)	methanol	97 %	99 %	2.6 %	300 °C, 1 atm, CH ₃ OH/H ₂ O/Ar 1:2:1 M ratio, WHSV = 8.5 h ⁻¹	250 °C, 30 h	[200]
3	CuO-CeO ₂	HKUST-1	methanol	97 %	–	0.5 %	270 °C, H ₂ O/CH ₃ OH 1.5:1 M ratio with 1.5 mL h ⁻¹	350 °C, 24 h	[201]
4	Cu/Ce-Cu(BDC)	Cu(BDC)	methanol	96 %	94 %	2.0 %	250 °C, 32 h, 1 atm, WHSV = 9.2 h ⁻¹	320 °C	[202]
5	Ni ⁰ /ZIF-8	ZIF-8(Zn).PEG	ethanol	88 %	66 %	17 %	450 °C, 4 h, 1 atm, H ₂ O/C ₂ H ₅ OH 4:1 M ratio with 5.6 mL/h	450 °C, 10 h	[215]

reverse water–gas shift (RWGS) reaction during the endothermic process is necessary to avoid due to its coke formation and carbon monoxide generation, leading to the deactivation of catalysts [207]. Accordingly, in conclusion, designing materials with both high thermal and high chemical stability turns out to be an essential goal for the future catalytic steam reforming reactions, especially for MOF in this case. An overview of various MOF and MOF-derived catalysts applied for steam reforming reactions are summarized in Table 1.

6.1.2. The influence of metal selection on catalysts

Running through mountains of research, copper and group IIX-X transition metals are found to be the two primary catalytic metals used substantially in methanol steam reforming (MSR) reactions [208]. By comparison, copper-based catalysts have better hydrogen production performance and are superior in the ample resources; namely, they have more catalytic activity and are less expensive [209]. On the other hand, sintering and metal agglomeration come to light during the evaluation of temperatures approximately 300 °C owing to their low thermal stability [210]. Therefore, facing the obstacles of thermal agglomeration becomes a crucial issue for copper based catalytic MSR reaction. The other is group IIX-X transition metal which platinum and palladium are commonly used. It has to be mentioned that group IIX-X is more thermally stable compared to copper-based catalysts [211]. However, expensiveness and higher carbon monoxide yield become fatal drawbacks as catalysts. Apart from this, nickel and cobalt are also chosen to be applied to catalysis in steam reforming reaction instead of platinum and palladium among transition metals because of their affordable prices, which would be dominant in future commercial mass production processes [212]. First of all, Kamyar et al.'s study, which is the first investigation of MOF-supporting catalysts applied to the MSR process [199]. In their study, Kamyar demonstrated a new MSR catalyst by using *cis*-PtCl(SMe₂)₂(SnCl₃) complex as a single precursor instead of two separated metals to control the stoichiometric ratio of bimetallic Pt/Sn 1:1 precisely. By impregnating the different amounts of precursor on MIL-101(Cr) as a support, they synthesized respectively 10.2 %, 19.7 %, and 28.9 % metal loading of Pt-SnO@MIL-101(Cr). The bimetallic catalysts contain platinum as the active metal for MSR reaction and tin as a promoter in order to prevent platinum from sintering and coke formation, which has been investigated in the case of glycerol steam reforming [213]. In order to get further insight on Pt-SnO@MIL-101(Cr), they analyzed the characterizations by sorts of instruments. From BET data, the significant specific surface area of Pt-SnO@MIL-101(Cr) catalysts imply the inheritance of a high surface area from the mother MOF. Transmission electron microscope (TEM) indicates small metal particle size and high dispersion of nanoparticles on MOF. Eventually, by comparing the results of three different metal loading catalysts, it shows the increase of both H₂ and methanol selectivity and the

decrease of CO selectivity as the number of active nanoparticles increases. In conclusion, they successfully achieved a high H₂ selectivity (89 %) and methanol conversion (92 %) with low CO selectivity (3.4 %) by using Pt as their active metal, SnO as their promoter and MIL-101(Cr) as their support, which is an excellent beginning in the future MOF-supporting catalytic MSR reaction field. Next, instead of using noble metals as the active sites, this is an example of copper-based catalysts applied for MSR reaction. A novel route to the synthesis of MOF-derived bimetallic oxide catalysts (Fig. 13) was reported by Chen et al. [201]. Different from two main approaches to synthesizing MOF-derived bimetallic oxide, which is an impregnation metal on MOF as the support and subsequently undergoes a calcination process, and the straight path of bimetallic MOFs pyrolysis. Chen's group determined to use MOF-derived metal oxide as the precursor adsorbed on another metal oxide for the purpose of accomplishing the goal of bimetallic catalysts. In their work, they first prepared polyvinylpyrrolidone (PVP)-encapsulated CeO₂ abbreviated to CeO₂@PVP. Subsequently, they stirred suspended CeO₂@PVP and a slurry of HKUST-1, which benefits its relatively easy preparation compared to other Cu-based MOF, at room temperature in order to set up an environment for HKUST-1 crystallization as well as the adsorption effect of PVP, which led to the formation of HKUST-1-CeO₂. Ultimately, the desired catalyst CuO-CeO₂ is synthesized by calcinating HKUST-1-CeO₂. For comparison, they synthesized another conventional catalyst labeled CuO-CeO₂-I by using impregnation and calcination. They claimed that the performance of CuO-CeO₂ catalyst in the MSR process is better than conventional CuO-CeO₂-I catalyst on both hydrogen production and CO selectivity. From the material analysis, there came cogent evidence from H₂-TPR that a lower reduction temperature peak of CuO-CeO₂ was detected, corresponding to the relative high CuO dispersion because of the

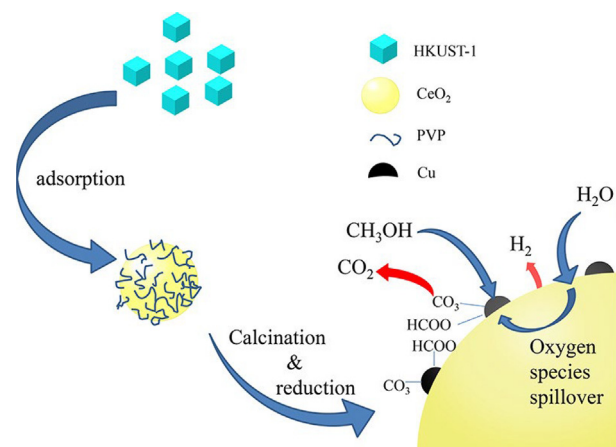


Fig. 13. Schematic representation for the synthesis of HKUST-1 derived CuO on CeO₂. Reproduced from Ref. [201] with permission of the Elsevier.

abundant oxygen defects formed during the preparation, which could be proven by Raman spectra analysis. In this case, by using HKUST-1-derived CuO-CeO₂ catalysts, they achieved 97 % methanol conversion and 2.3 % CO selectivity in the methanol steam reforming process.

6.1.3. The influence of thermal stability on catalysts

Since the steam reforming reaction is endothermic, the reaction is generally carried out under a high-temperature environment ranging approximately from 200 °C to 500 °C [214]. Thus, the property of high thermal stability turns out to be one of the most critical conditions for the catalyst design. Some researchers fixed their eyes on the inborn high thermal stability nature MOF as the catalysts [199–202,215]. In addition, taking MOFs as sacrificial precursors to derive metal oxides by processing heat treatment is another promising route to synthesize high thermal stability substrates [200]. In this review, we summarized some catalysts applied for the steam reforming reaction by using MOF catalysts: the Pt-SnO@MIL-101(Cr) catalysts from Kamyar's group, the Ni⁰/ZIF-8 catalysts from Razavian's group, and the Cu/Ce-Cu(BDC) catalysts from Varmazyari's group [199–202,215]. From the previous conclusion, it can be seen that both the decomposition temperature of MILs and ZIFs analogs are suitable for the steam reforming reaction, which could be proven in practice as well [160]. When it comes to the thermal stability of MOFs, Healy et al.'s work must be introduced [40]. After a series of TGA experiments, the thermal decomposition temperature (T_d) data they summarized, shown in Fig. 14, indicates the resemblance within each group according to the similar decomposition mechanism they claimed. Instead of looking into the decomposition mechanism of MOF they proposed, we will put emphasis on the outcome and the applications of MOF under the heat treatment process in the future. It is evident from Fig. 14, that hybrid ultra-microporous materials (HUMs) exhibit the poorest thermal stability out of the low decomposition temperature at 300 °C or below, which represents that HUMs are not suitable for catalytic substrates in SR reaction. HKUST and MIL-100 analogs share better thermal stability performance based on the decomposition temperature being 400 °C or below, which are available in some moderate temperature conditions in SR reaction. Isorecticular MOFs (IRMOFs), pyrazoles, and UiOs analogs are all approximately limited below the temperature at 500 °C, whereas ZIFs and UiOs show a significant temperature range from 300 °C to 500 °C. However, compared to all the other categories of

MOFs, Healy et al.'s found an outstanding thermal stability MOF called ultralight MOF (ULMOF), which decomposed at almost 600 °C. Instead of directly using MOF catalysts, here comes a study focusing on the effects of catalytic thermal performance by using MOF-derived catalysts. Khani et al. paid attention to alumina as their support because of not only its well-known high thermal stability but also mechanical stability in the process of MSR [200]. Thus, Khani's group chose one of the aluminum-containing MOFs called A520 among several alumina materials because of its relatively high porosity, high specific surface area, and most importantly, mass-produced feature as a potential factor in industrial production scale. Based on those conditions, they synthesized six different catalysts by alternating catalytic metals and supports, including Pd/A520 MOF, Cu/A520 MOF, Pd/Al₂O₃(A), Cu/Al₂O₃(A), Pd/Al₂O₃(M), and Cu/Al₂O₃(A) where Al₂O₃(A) and Al₂O₃(M) representing alumina derived from A520 and commercial alumina purchased from Merck respectively. Judging from the results, the performances of hydrogen and CO selectivity along with coke formation are dominated by both metallic differences and supports. To be more specific, Pd-based catalysts perform better than Cu-based catalysts on the same support; however, when comparing the same active metal with different support, the catalysts supported on Al₂O₃(A) perform better than Al₂O₃(M) in DRM reaction. Hence, they reported that Pd/Al₂O₃(A) attained the highest methanol conversion (97 %), the highest H₂ yield (99 %), and the lowest CO selectivity (2.6 %) by using MOF-derived alumina supporting catalyst.

6.1.4. The influence of chemical stability on catalysts

As was mentioned how vital thermal stability was in the previous section, we will focus on another subject in this section. As the scaling-up hydrogen production process develops, the deactivation problem of catalysts becomes more and more inevitable as long as the reaction time is expended, which is included poisoning, fouling, metal sintering, coking, etc. [216]. Prevention from the formation of coke for hydrocarbon steam reforming reaction has been investigated for decades. In this review, we will discuss the main approaches to exhibit the coke formation. Firstly, the addition of promoters is efficiently valid in suppressing the formation of coke. Varmazyari et al. moved a big step forward on the MSR reaction by discussing metal promoters on MOF-supporting catalysts [202]. The catalyst is prepared by a three-stage impregnation process which are the impregnation of Cu(BDC) on monoliths, the impregnation of promoter(X) on Cu(BDC)/monolith, and lastly, the impregnation of Cu on Cu/X-Cu(BDC) supported on the monolith. By impregnating seven different promoters, they examined the catalytic activity of Cu/X-Cu(BDC) (X = Ce, Zn, Gd, Sm, La, Y, Pr) catalysts. After the experiments, the results showed the difference in the case of MSR reaction under the following order of Cu/X-Cu (BDC): Ce > Sm > Y > La > Pr > without promoters > Zn > Gd. Driven by curiosity, Varmazyari et al. were dedicated to investigating what made Cu/Ce-Cu(BDC) the most suitable catalyst. According to the characteristic technique called H₂-TPR analysis, which could speculate the CuO dispersion, Ce, Y, Sm, Pr, and La metal promoters show lower reduction peak temperature in ascending order but Zn and Gd act conversely. As the paper mentioned, the copper oxide reduction temperature occurs at higher temperatures by weakening the interaction between the metal oxide and the support, which may result in poor metal oxide distribution leading further to undesired catalytic performance. Besides, there is other direct evidence to prove the higher metal dispersion and smaller nanoparticle size from TEM micrographs. It is worth mentioning that the oxygen storage capacity of cerium oxide. By changing Ce³⁺ to Ce⁴⁺, cerium oxide releases the oxygen from the surface and the lattice without destroying the structure, contributing the effect on decreasing coke formation via oxidizing the carbon

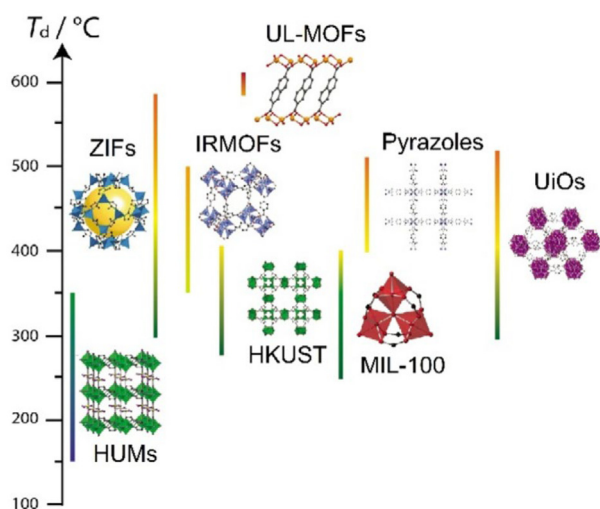


Fig. 14. Observed thermal decomposition temperature (T_d) values for a range of MOF family. Reproduced from Ref. [40] with permission of the Elsevier.

deposit to carbon dioxide [217]. Additionally, there are more oxygen defects on the catalysts decorated with promoters Pr, Sm, and Y as well, contributing to a tendency of higher H₂ selectivity and lower CO selectivity through the MSR process. The addition of Ce as a promoter had a major influence on MSR performance, in which 96 % methanol conversion, 94 % H₂ yield, and 2.0 % CO selectivity were attained for Cu/Ce-Cu(BDC). What is more, there is an exciting approach to alleviate coke formation by decorating MOF. Razavian et al. reported another possible path to accomplish not only high hydrogen yield but also the hamper of coke formation by using MOF-supporting catalysts [215]. To the best of our knowledge, this is the first study of ZIF-8 as catalytic support in ethanol steam reforming (ESR) reaction. It should be mentioned that Razavian et al. modified ZIF-8 by adding a linear polymer named polyethylene glycol (PEG) for the purpose of increasing the mesoporous volume after the thermal removal process characterized by the relevant BJH pore size distribution profile, leading to impeding the occupation of coke during the process. As observed in the NH₃-TPD analysis, which helps us to identify the acidity of materials, the higher desorption temperature from ZIF-8.PEG demonstrates the acidity strength of ZIF-8.PEG is stronger than ZIF-8's even though the total acidity is equivalent. In comparison with the conventional Ni/ γ -Al₂O₃ catalyst, Ni/ZIF-8.PEG made significant progress in both ethanol conversion (88 %), hydrogen selectivity (66 %) and CO selectivity (17 %), arising from the high specific surface area, high dispersion of active sites, outstanding thermal stability, and lower acidity strength compared to Ni/ZIF-8 and conventional Ni/Al₂O₃.

6.2. Hydrogen production from the dry reforming reaction

The escalating global warming problem has grabbed attention world-widely. Therefore, the dry reforming reaction of methane (DRM) involves the rearrangement between two greenhouse gases (methane and carbon dioxide) to form valuable synthetic gas comprised of carbon monoxide and hydrogen as alternative energy resources (see Eq. (4) below) [218]. Furthermore, the stoichiometric equivalence between CO and H₂ has been extensively used in generating various hydrocarbons depending on the catalysts via the Fischer-Tropsch process [219,220].



The standard enthalpy of DRM is + 247 kJ mol⁻¹, representing that the DRM reaction is highly endothermic [218]. Compared with steam reforming reaction, the DRM is usually carried out under a higher-temperature environment ranging from 600 °C–800 °C, demonstrating that DR reaction consumes more energy than SR reaction [221]. However, DR reaction is still a promising green preparation for syngas and hydrogen production because of its

environmentally friendly greenhouse gas consumption. An overview of various MOF and MOF-derived catalysts applied for the dry reforming reactions are summarized in Table 2.

6.2.1. The influence of metal selection and thermal stability on catalysts

At present, the catalysts introduced in dry reforming (DR) reaction with supported noble metals such as platinum, palladium, ruthenium, iridium, or rhodium are active and stable [222]. However, one cannot have it both ways because of the lethal disadvantages of the industrial scale-up process being expensive and rarely available. Instead, researchers shift the focus to the transition-metal-based catalysts (nickel, cobalt, iron, etc.) applied to DR reaction; nickel is commonly used because of its high catalytic activity and relatively low cost [223]. As we mentioned before that DR is an endothermic reaction, DR reaction is required to carry out under high-temperature conditions over 600 °C, which exhibits the reaction is exceedingly energy-intensive [221]. Thence, high-temperature resistance materials, namely MOF-derived metal oxides under this circumstance, are one of the best options for catalytic supports because of their distinguished high surface area from mother MOF. Karam et al. from Sorbonne university of Paris and the University of Balamand dedicated themselves to highly dispersed nickel nanoparticles embedded on MOF-derived support for DRM reaction [224–226]. At the beginning of the investigation, they aimed to compare the difference in DRM performance between two preparation routes of nickel-based alumina catalysts: MOF-derived approach and evaporation-induced self-assembly (EISA) one-pot approach, which are labeled with A and B, respectively [Fig. 15] [224], in the following figure. In the A route, aluminum-containing MOF named MIL-53(Al) features the anchoring points for Ni²⁺ ions after the nickel impregnation process owing to the aluminum-hydroxyl nodes linked by organic structuring ligands. After the thermal calcination and sequent reduction process, highly dispersed reduced nickel nanoparticles on γ -Al₂O₃ catalysts are obtained through this procedure. The B route is a so-called one-pot synthesis stemming from the direct combination of nickel and aluminum precursors, organic ligands, and solvents in the synthesis gel, leading after the evaporation triggers the self-assembly process leading to the formation of hexagonal hybrid nickel-aluminum materials. After the thermal calcination, the organic linkers are removed to release the porosity so that the mesoporous nickel-alumina supports are obtained. Then, the well-dispersed Ni⁰ nanoparticles on γ -Al₂O₃ catalysts are finally obtained after reduction from Ni²⁺ to Ni⁰. The similarity between these two approaches is that the nickel aluminate intermediate (NiAl₂O₄) directly proven by XRD and TPR characterizations after the calcination process would significantly enhance the dispersion

Table 2
Summary of MOF-derived catalysts applied for dry reforming of methane reactions.

Entry	Catalyst	MOF/MOF precursor	Reactant	Reactant Conversion	CO ₂ Conversion	H ₂ /CO ratio	Reaction condition	Stability	Ref.
1	Ni _{5wt%} -Al ₂ O ₃ -MOF	MIL-53(Al)	methane	76 %	79 %	1.03	650 °C, 13 h, 1 atm, GHSV = 72 L g ⁻¹ h ⁻¹	650 °C, 13 h	[224]
2	Ni ⁰ /Al ₂ O ₃	MIL-53(Al)	methane	74 %	80 %	1.03	650 °C, 100 h, 1 atm, CH ₄ /CO ₂ /Ar 5:5:90 M ratio, GHSV = 72 L g ⁻¹ h ⁻¹	650 °C, 100 h	[225]
3	NiCo@C/ Al ₂ O ₃	Ni-Co-MOF	methane	52 %	76 %	0.87	700 °C, Flow rate: 5 vol% methane, 5 vol% CO ₂ , 90 vol% N ₂	700 °C, 8 h	[229]
4	Ni-Co@CMOF-74	MOF-74(Ni, Co)	methane	57 %	65 %	0.82	750 °C, 7 h, 5 bars, CH ₄ /CO ₂ /N ₂ 1:1:1 M ratio, GHSV = 18 L g ⁻¹ h ⁻¹	700 °C, 10 h, 5 bars	[228]
5	PtNP@UiO-67	UiO-67(Zr)	methane	56 %	43 %	1.10	11 W, CH ₄ /CO ₂ 1:1 M ratio, feed flow rate: 100 mL min ⁻¹	11 W, 2 h	[232]
6	Ni ⁰ /Al ₂ O ₃ -PET	MIL-53(Al)	methane	70 %	75 %	1.00	800 °C, 2 h, 5 vol% H ₂ /Ar, 30 mL min ⁻¹	650 °C, 13 h	[226]

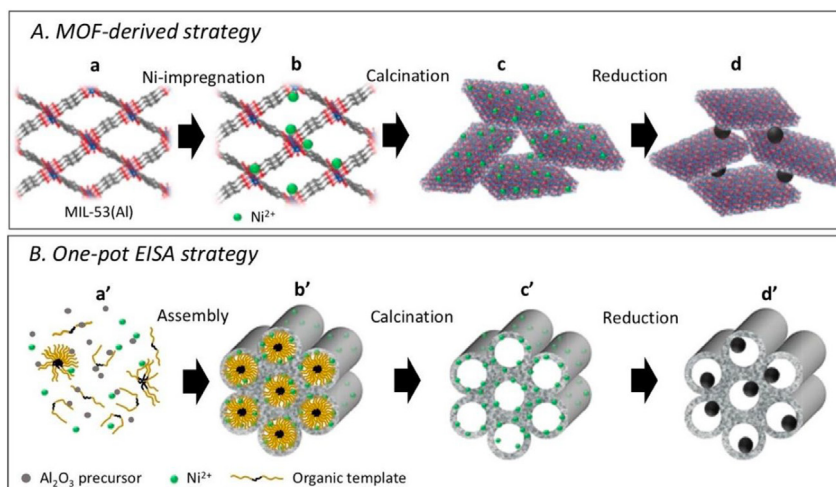


Fig. 15. Schematic representation of the (A) MOF-derived and (B) one-pot EISA synthesis routes. Reproduced from Ref. [224] with permission of the MDPI.

of nickel nanoparticles and diminish nickel mobility by strengthening the interaction between metal nanoparticles and support, which contributes to the well catalytic stability and performance in DRM reaction. From the catalytic performance of the $\text{Ni}_{5\text{wt}\%}\text{-Al}_2\text{O}_3\text{-MOF}$ and $\text{Ni}_{5\text{wt}\%}\text{-Al}_2\text{O}_3\text{-EISA}$ catalysts in DRM reaction, we can tell that both catalysts do a remarkable job in reactant conversions and H_2/CO ratio. Nonetheless, Karam et al. confirmed that the MOF-derived catalysts still performed merely better catalytic results, which could be attributed to two main reasons. Firstly, the higher specific surface area provides easier approachability to active nickel sites, which could directly be proven through BET analysis. Secondly, smaller metal nanoparticles and better Ni^0 dispersion were performed in MOF-derived catalysts because of the strong nickel-alumina interaction resulting from the nickel aluminate spinel intermediates (NiAl_2O_4) in the calcined materials. The X-ray diffractogram results showed the prominent peaks of NiAl_2O_4 in the case of calcinated $\text{Ni}_{5\text{wt}\%}\text{-Al}_2\text{O}_3\text{-MOF}$. Meanwhile, the higher reduction temperature of $\text{Ni}_{5\text{wt}\%}\text{-Al}_2\text{O}_3\text{-MOF}$ was exhibited compared with $\text{Ni}_{5\text{wt}\%}\text{-Al}_2\text{O}_3\text{-EISA}$'s in TPR profiles which represented that nickel oxides were embedded more homogeneously due to the nanocrystalline spinel. Likewise, the elucidation was in line with the XRD results. Comparing the DRM performance between $\text{Ni}_{5\text{wt}\%}\text{-Al}_2\text{O}_3\text{-MOF}$ and $\text{Ni}_{5\text{wt}\%}\text{-Al}_2\text{O}_3\text{-EISA}$, the conversion of methane is 76 % and 71 %, the conversion of CO_2 is 79 % and 75 %, and H_2/CO ratio is 1.03 and 1.09, respectively. In the further investigations of $\text{Ni}_{5\text{wt}\%}\text{-Al}_2\text{O}_3\text{-MOF}$ denoted as $\text{Ni}^0\text{Al}_{\text{MIL}}$ catalysts in this work applied to practical large-scale steam reforming reaction of methanol, there is an increasing emphasis on the importance of its stability and reaction duration [225]. Thereby, Karam et al. remeasured the catalytic performance, such as reactant conversions and H_2/CO ratio with the exclusive prolonged reaction duration from 13 h to 100 h and other consistent parameters to demonstrate the overwhelming reaction stability from the catalyst. From the conversions and H_2/CO ratio to the time diagram they plotted, we could learn that $\text{Ni}^0\text{Al}_{\text{MIL}}$ not only remained stable over 100 h of reaction duration and still kept in the initial stage but also nearly approached the calculated thermodynamic equilibrium conversions regarded as the maximum conversions, which were contributed to the homogeneous metal nanoparticles dispersion leading to barely deactivation. According to the TGA profiles, there was nothing to trace weight loss of the spent $\text{Ni}^0\text{Al}_{\text{MIL}}$, which indicated that side reactions resulting in coke formation were well inhibited. Extending the reaction time from 13 h to 100 h shows that methane conversion decreases from 76 % to 74 %, CO_2 conversion increases from 79 % to 80 %, and H_2/CO ratio increases from

1.01 to 1.03 in the DRM reaction. Afterward, with the goal of fulfilling a circular economy, Karam et al. aimed to improve the catalyst synthesis recipe to a more sustainable preparation via fabricating MIL-53(Al) by using PET plastic waste as the source of terephthalic acid as solutions for the growing environmental problem [226]. Consequently, in this study, Karam et al. comprehensively evaluated four catalysts followed by different preparation routes, including $\text{Ni}^0\text{-Al}_2\text{O}_3\text{-PET}$, $\text{Ni}^0\text{-Al}_2\text{O}_3\text{-BDC}$, $\text{Ni}^0\text{-Al}_2\text{O}_3\text{-BDC}_{\text{MW}}$, and $\text{Ni}^0\text{-Al}_2\text{O}_3\text{-COM}$, in catalytic performance as well as the stability. They highlighted the fungibility of PET-derived catalysts instead of sacrificing the previous overpriced organic linker. Among these four catalysts, it shows a pronounced tendency that $\text{Ni}^0\text{-Al}_2\text{O}_3\text{-BDC}_{\text{MW}} > \text{Ni}^0\text{-Al}_2\text{O}_3\text{-PET} > \text{Ni}^0\text{-Al}_2\text{O}_3\text{-BDC} > \text{Ni}^0\text{-Al}_2\text{O}_3\text{-COM}$ within both CH_4 and CO_2 conversion and H_2/CO ratio as well, which indicates the PET-derived catalysts displays not only a better environmentally friendly materials but also alternative catalysts in DRM reaction in the future. It is noteworthy that the best performance catalysts denoted as $\text{Ni}^0\text{-Al}_2\text{O}_3\text{-BDC}_{\text{MW}}$ is a microwave-based preparation fabricated by route A I mentioned previously. In this case, PET-derived $\text{Ni}^0/\text{Al}_2\text{O}_3$ displays 70 % methane conversion, 75 % CO_2 conversion, and 1.00 H_2/CO ratio.

6.2.2. The influence of chemical stability on catalysts

As opening up new horizons for the utilization of transition-metal-based catalysts applied to DRM reaction, the catalytic deactivation problems swept under the carpet finally came to the fore. There are two main drawbacks for industrial applications: firstly, metal sintering effects at high temperatures may lead to agglomeration; secondly, the formation of coke deposits occurs due to the decomposition of methane as a side reaction, which both result in the significant loss of active sites [227]. Liang et al. proposed novel bimetallic MOF-derived catalysts by an in-situ process of mixing nickel and cobalt precursors, functionalized $\text{H}_2\text{-BDC-NH}_2$, alumina in DMF, and acetic acid as a means to set up the environment for Ni/Co-MOF hydrothermal synthesis growing on alumina support [228]. Finally, the MOF-derived catalysts denoted as $\text{NiCo@C}/\text{Al}_2\text{O}_3$ are acquired after the pyrolysis and reduction operation. As the results of the catalytic performance experiments, MOF-derived $\text{NiCo@C}/\text{Al}_2\text{O}_3$ were regarded as high-efficiency catalysts for DRM reaction based on its high conversions, high H_2/CO ratio, low amounts of coke deposits, and high turnover frequencies (TOF). In order to figure out what made the MOF-derived alloy-carbon composites high-performance catalysts, Liang et al. [228] analyzed catalysts from different aspects. They found that the carbon shell covering metallic sites synthesized during the pyrolysis

process (shown in Fig. 16) functionalized as spacers to prevent metal from gathering, which represents that the carbon shell alleviates the sintering problem. Besides, the amorphous carbon also acted as a barrier to reduce the diffusion rate of methane to the active metal site, thereby suppressing coke formation due to rapid methane carbonization. Moreover, the addition of cobalt was determined by CO₂-TPD that there was an increase of basicity on the surface of catalysts, leading to stronger adsorption to CO₂, which was beneficial to the DRM reaction. To summarize, they proposed a MOF-74 derived Ni-Co metals on Al₂O₃ applied for dry reforming of methane, and the results show 52 % methane conversion, 76 % CO₂ conversion, and 0.87 H₂/CO ratio. Khan et al. brought over another MOF-derived catalyst treated after the thermal carbonization process featuring the benefits of Ni-Co-MOF as precursors for DRM reaction [229]. They prepared a bimetallic heterogeneous catalyst with the same active metals, but a different class of MOF named MOF-74 by carbonizing the as-synthesized Ni-Co MOF-74/CPO-27 via nitrogen pyrolysis condition. Finally, Ni-Co@CMOF-74 was obtained after the passivation process under a 5 % oxygen environment. It is interesting that Khan's group noticed the pressure problem of the carbon-shell-protected catalysts. Initially, they attempted to implement the catalytic performance under atmospheric pressure to establish the baseline for the latter experiments. However, surprisingly, none of the MOF-derived catalysts showed the activity for methane and carbon dioxide. It turned out to be the impendence caused by carbon shells required an extra pressure gradient so that the gas-phase reactants could be adsorbed by active metals by penetrating over the carbon shells; thereby, the experiments were performed under 5 bars to show their catalytic performance, including methane conversion (57 %), CO₂ conversion (65 %), and H₂/CO ratio (0.82) were attained for Ni-Co@CMOF-74.

6.2.3. The nonthermal-activated dry reforming reaction

In spite of the fact that thermal catalytic dry reforming reaction of methane (DRM) is known as the promising approach to producing syngas by consuming the escalating emission of greenhouse gases day by day, the intensive energy consumption becomes an obstacle on the path to green process because of its thermodynamics. There is more and more attention to the non-thermal activated dry reforming reaction to cope with the energy problem [230,231]. In this case, Vakili et al. proposed a plasma-assisted catalytic DRM process by using UiO-67 MOF-based catalysts [232]. During the non-thermal plasma process, delocalized electrons accelerated by

the electric field collide with the neutral atoms leading to the formation of ions and radicals, which are unstable but reactive. It was measured that the collisions did not cause an apparent temperature rise because of their insignificant collision momentums, which was an appealing benefit compared to the thermal-assisted catalytic process [232]. Now turning to the catalyst design, as discussed in the thermal stability of MOF above in the steam reforming section, UiO analogs with a wide range of thermal decomposition temperatures are available for plasma-assisted DRM. Herein, Vakili and co-workers [232] demonstrated the DRM catalytic performance over three materials: ZrO₂, UiO-67(Zr), and PtNP@UiO-67(Zr). Before proceeding to examine the performances of DRM reaction, it will be necessary to figure out the mechanism of plasma-assisted DRM reaction, which is shown in Fig. 17; there are two initial paths of plasma dissociation from CH₄ and CO₂ to produce CH_x (x = 1, 2 and 3) and O radicals, respectively. They mentioned that electron energy dominated the selectivity of hydrocarbon in previous studies. To be more specific, high electron energy would result in the formation of C₂H₂ and vice versa; more C₂H₆ and C₃H₈ would be formed with low electron energy conditions. The results showed higher light hydrocarbons (C₂H₂/C₂H₄) selectivity but lower C₂H₆ selectivity on UiO-67 in non-thermal plasma-assisted DRM reaction plasma-alone and ZrO₂ results, which indicated that the high porosity nature and specific surface area of UiO-67 benefits the formation of the filamentary micro discharges and surface discharges respectively. Additionally, the well-performance capacity of CO₂ and CH₄ adsorption benefits the conversions of CO₂ and CH₄ as well. Moreover, in this case of DRM reaction, the PtNP@UiO-67 with the addition of active metal nanoparticles could efficiently promote the catalytic performance in both selectivity and conversion attributed to the dissociation of reactants which in-situ DRIFTS characterizations could prove. In this case, PtNP@UiO-67(Zr) achieved 56 % methane conversion, 43 % CO₂ conversion, and 1.10 H₂/CO ratio in the non-thermal plasma-assisted DRM reaction. Although the catalytic performance, in this case, seems to be in the shade compared with other catalysts in the dry reforming process, the apparent advantage is its low-required energy which is beneficial to future green hydrogen production.

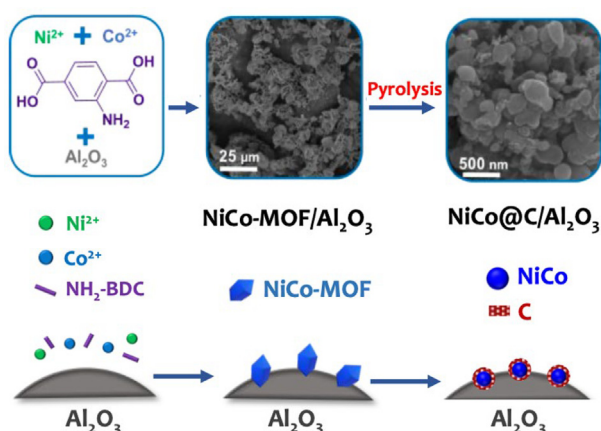


Fig. 16. Schematic representation for the synthesis of NiCo-MOF and derived NiCo@C nanocomposites on Al₂O₃. Reproduced from Ref. [228] with permission of the American Chemical Society.

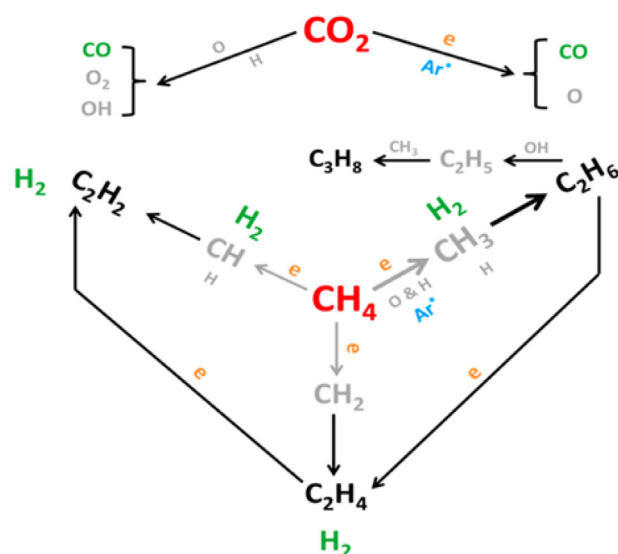


Fig. 17. Main reaction pathways in plasma-assisted catalytic DRM. Products and intermediates are shown in black (or green) and gray, respectively. Metastable Ar is shown in blue. Reproduced from Ref. [232] with permission of the Elsevier.

7. Photo and/or electrocatalytic systems for hydrogen evolution, oxygen evolution, and overall water splitting assisted by covalent organic frameworks

Covalent organic frameworks (COFs) are highly crystalline materials that offer an excellent platform for constructing unique photo and/or electrocatalytic systems for hydrogen production, oxygen production, and overall water splitting. According to our knowledge, this is the first review report on developing hydrogen evolution strategies for the covalent Organic Framework, including water reduction, oxygen generation and overall water splitting through photocatalysis, electrocatalysis, and photoelectrochemical processes, respectively. Water splitting by photocatalysis involves HERs and oxygen evolution reactions [233]. A photocatalytic material is ultraviolet–visible with ultraviolet, visible, or ultraviolet–visible (UV–Vis) light, which creates photo-excited electrons and holes, causing water to be reduced/oxidized into hydrogen and oxygen (Fig. 18(a)). It is, however, difficult to further make the efficient HER because of recombination of electrons and holes. A sacrificial electron donor (SED) such as triethanolamine (TEOA), triethylamine (TEA), diethylamine (DEA), and ascorbic acid (AA) plays a vital role in photocatalytic hydrogen evolution by participating in reduction or oxidative quenching [234]. A typical photochemical system consists of PSs, electronic relays (ERs), semiconductor electrolytes (SEDs), and catalysts (PS⁺) [235]. By SED, it is reduced to PS⁻ (reduction quenching mechanism) or oxidized to PS⁺ by ER (oxidative quenching mechanism). In addition, PS⁺ can react directly with SED to generate PS for the oxidative quenching pathway. In contrast, PS can respond with ER to generate PS as part of the reductive quenching pathway. Additionally, both the reduced ER⁻ and the catalyst can be applied to the proton reduction reaction to generate H₂. Additionally, it is worth noting that the catalyst and PS in a three-component photocatalytic system can be directly used for the photocatalytic response without ER [235–237]. In a photoelectrochemical system, the COF can also be deposited onto an electrode to serve as a working electrode instead of a SED. Electrons will be extracted from the counter electrode oxidative reaction to fill the holes in the VB (Fig. 18(b)) [238].

7.1. COFs for photocatalytic HER, OER, and overall water splitting

Achieving hydrogen production through photocatalytic water splitting using water and sunlight, two sustainable and infinite resources on this planet, is thought to be the essence and of fundamental importance to address the global energy crisis and issues with global warming [239]. Hydrogen is widely regarded as the

best alternative to fossil fuels. The field of photocatalytic hydrogen evolution using COFs as photocatalysts has recently attracted more study interest and is becoming a potential area [240–242]. Enhancing the ability to absorb visible light, enabling electron-hole separation, and suppressing photocorrosion over a long period of time are all examples of how to design and modify photocatalysts for increased performance. COFs as a versatile platform show promising applications in photocatalysis, and numerous ways for improving their activity based on pristine COFs and modified COFs have been devised. The most straightforward technique to boost visible-light absorption and decrease recombination of photogenerated electrons and holes is through the intricate insertion of functional building blocks to adjust the optical and electrical properties of COFs [66]. COFs' physical and chemical characteristics may be altered by changing the building blocks, allowing for molecular control of their band gap configuration. Band gap engineering may be accomplished by incorporating anions and cations into the framework in order to improve light harvesting performance and tune redox band potentials. It is crucial for photocatalytic processes to effectively utilize solar energy throughout a broad range. Incorporating sensitizers is another intriguing technique for increasing photocatalytic activity by broadening light absorption to a larger wavelength range. Furthermore, COFs with various functional groups and π stacking nanosheets [Fig. 19] serve as an excellent platform for the synthesis of hybrid materials including various semiconductors. The formation of COF-based hybrid photocatalysts is regarded as a feasible and compelling strategy for improving photocatalytic activity, with the benefits of increasing visible light absorption, facilitating electron transfer between composites, and improving the separation efficiency of photogenerated electron-hole pairs.

7.1.1. COFs for photocatalytic HER

Currently, for photocatalytic water splitting, only a limited number of COF materials have been examined. Using rigorous molecular engineering, Seki and his co-workers developed a number of 2D isorecticular COFs as shown in Fig. 20(a). To establish a structure–property–activity relationship for COFs to identify key factors for efficient photocatalytic H₂ production, Donor – acceptor (D – A) conjugation, torsional angles, and reaction conditions were varied to realize the effect of light absorption, electronic band position, exciton migration, charge carrier generation and transport, layer stacking, crystallinity, surface area, and morphology over photocatalytic activity. As a result, the COFs exhibited different photocatalytic H₂ production under visible light. Light absorption, charge carrier formation, and transport

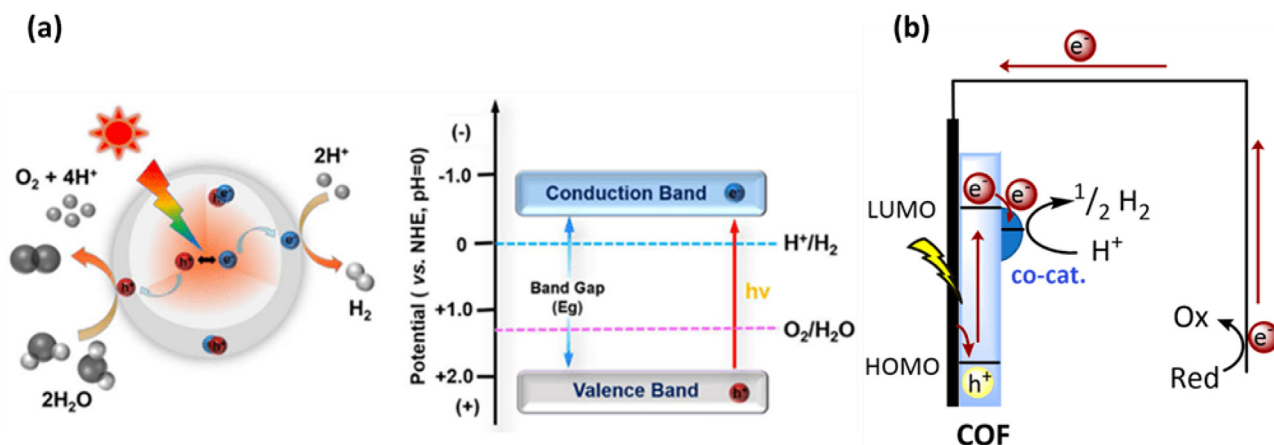
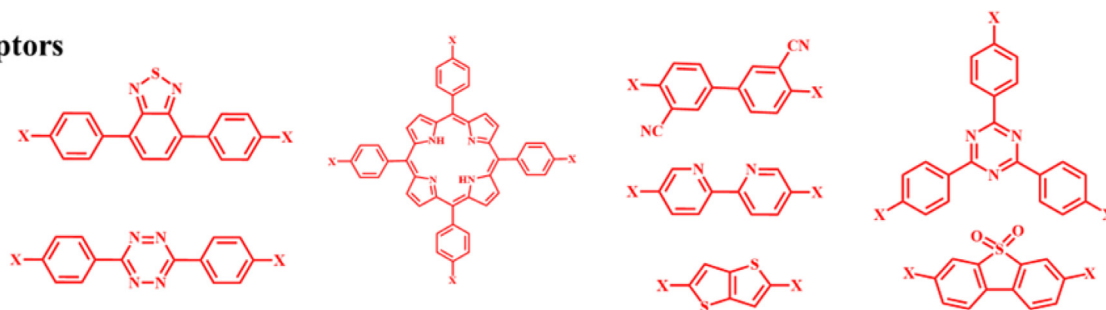
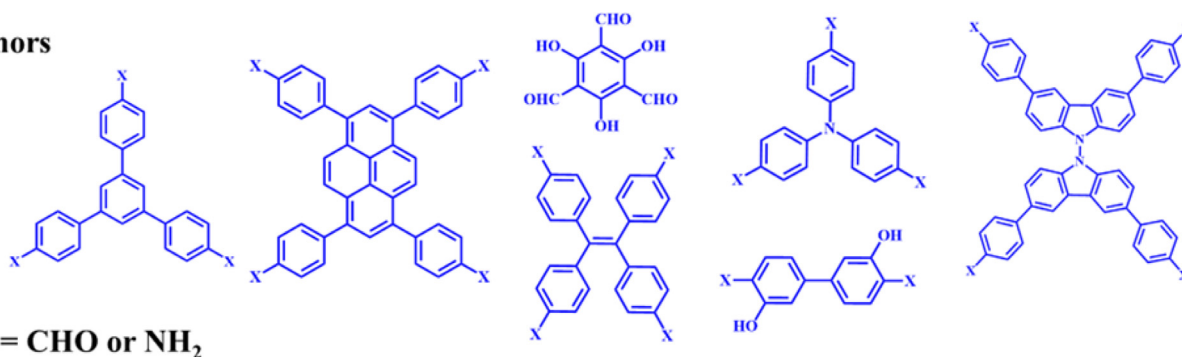


Fig. 18. (a) General Mechanism of photocatalytic water splitting of semiconductor materials and (b) photochemical Mechanism for H₂ generation. Reproduced from Ref. [238] with permission of the MDPI.

Acceptors



Donors



X = CHO or NH₂

Fig. 19. Structures of some the reported COF building blocks; donors and acceptors; used for photocatalytic water splitting.

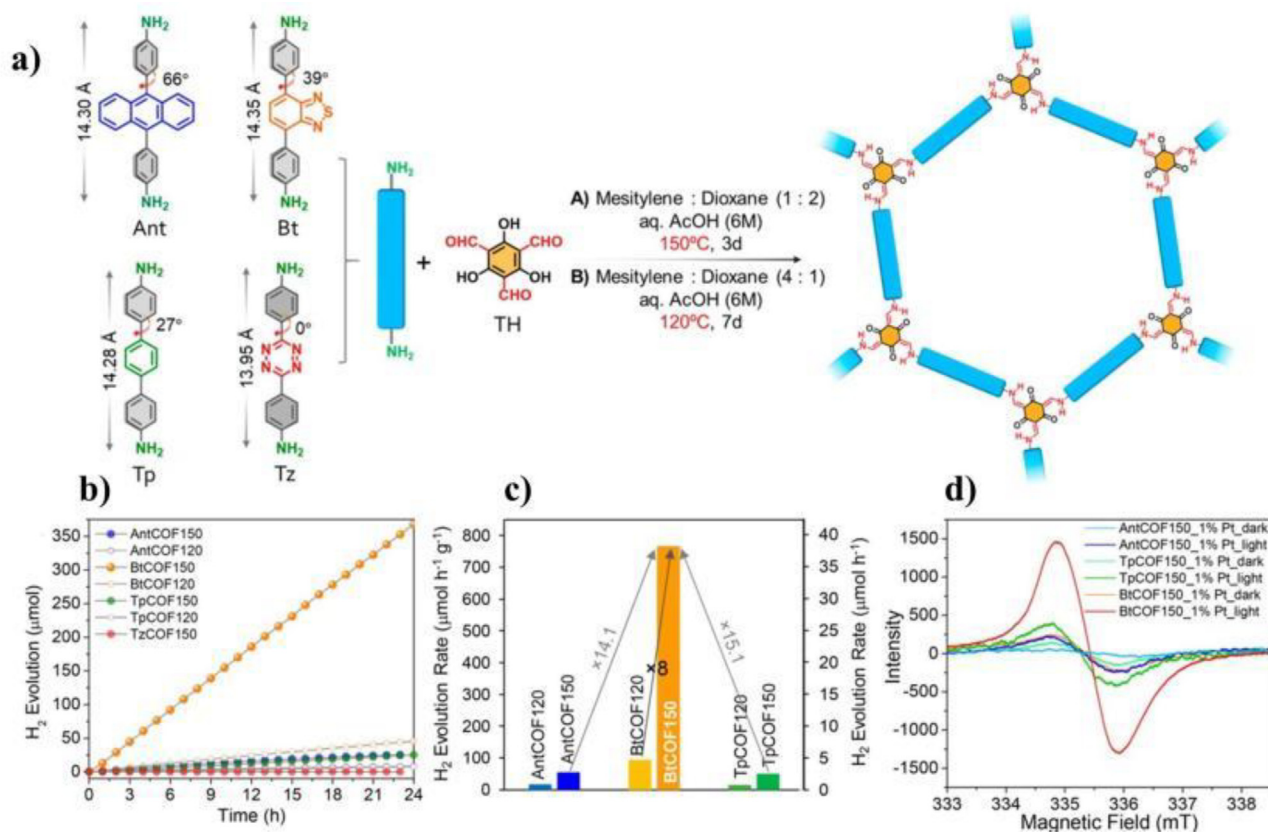


Fig. 20. (a) Chemical Structures of the Building Blocks along with Corresponding Molecular Lengths and Torsional Angles. (b) Time course for photocatalytic H₂ production under visible light (≥ 400 nm) of all of the prepared COFs (20 mg COF, 1 wt% Pt, water – TEOA (4:1, 100 mL, pH 11). (c) Comparison of photocatalytic hydrogen evolution rates. (d) EPR spectra of AntCOF150, TpCOF150 and BtCOF150 loaded with 1 wt% Pt under light and dark conditions. Reproduced from Ref. Ref. [243] with permission of the American Chemical Society.

were found to have a stronger effect on photocatalytic H₂ evolution than other parameters. Thus, in the presence of a low metallic Pt (1 wt%) cocatalyst, BtCOF150 demonstrated the highest rate of H₂ evolution [Fig. 20(b-d)] [243]. In the past few years, researchers have been studying how different functional groups connected to the backbone of COFs influence the effectiveness of photocatalytic H₂ evolution in recent years. Sun et al., have investigated the effect of donating and withdrawing functional groups attached in the backbone of COFs on the photocatalytic H₂ evolution activity, by synthesized a variety of ketoenamine-based COFs with the same host framework as model system, including TpPa COF X (X = -H, -(CH₃)₂, and NO₂) [Fig. 21(a)]. They observed that the donating group has a beneficial influence on photocatalytic activity, and that electron donating groups can develop strong conjugations effect, which can improve light absorption and charge carrier mobility, hence boosting photocatalytic activity [Fig. 21(b)]. On the other hand, the withdrawing group has a detrimental influence on photocatalytic activity. TpPa COF (CH₃)₂ has an H₂ evolution rate of 8.33 mmol g⁻¹ h⁻¹ and does not noticeably decrease after 30 h of irradiation [Fig. 21(c)], which is approximately 6 times and 38 times greater than TpPa COF and TpPa COF NO₂, respectively [244]. The incorporation of halogen atoms into the acceptor moiety of a donor-acceptor COF system might be a potentially beneficial technique for increasing the photocatalytic capabilities of COFs. Chen and his co-workers proposed photoactive benzothiadiazole (BT) based COFs (BT-COFs) as a modular example due to the strong electron-deficient acceptor unit of BT and the efficient intramolecular charge transfer induced by the D-A alternating skeletons via polycondensation of 4,4',4'',4'''-(pyrene-1,3,6,8-tetrayl)tetrabenzaldehyde (Py-CHO) with terphenyl based diamines (XTP-BT-NH₂) annulated with fluorinated, chlorinated or non-halogenated BT units under solvothermal conditions [Fig. 21(d)]. Powder X-ray diffraction measurements were used to investigate the crystallinities of Py-XTP-BT-COFs as shown in Fig. 21(e) and (f). Py-CITP-

BTCOF demonstrated significantly higher photocatalytic H₂ evolution rates (HER = 177.50 μmol h⁻¹) than that of Py-FTP-BT-COF (HER = 57.50 μmol h⁻¹) and the non-halogenated Py-HTPBT-COF (HER = 21.56 μmol h⁻¹), suggested that the facilitated charge separation and reduced energy barrier for H₂ formation in these halogenated BT-COFs are the primary reasons accounting for the enhanced photocatalytic performances [Fig. 21(g-i)]. Chlorine modification at the photoactive benzothiadiazole moiety can suppress charge recombination more effectively and greatly lower the energy barrier associated with the generation of H intermediate species (H*) on the COF surface [245]. Researchers have used metal-based catalysts to increase the performance of COF-based hydrogen evolution photocatalysts since it has been shown that metal-based catalysts improve charge recombination in several types of semiconductor-based photocatalysts. Metal-decorated COFs have recently received more interest in hydrogen evolution. Sun et al., synthesized a series of COF (TpPa-2) composite materials modified with nickel hydroxide (Ni(OH)₂-X%/TpPa-2), which show the highly enhanced photocatalytic H₂ evolution activity from the original COF (Fig. 22(a)). In this work, nickel is used as a co-catalyst which is an efficient material that improves charge separation and visible light absorption. The photocatalytic hydrogen evolution studies under visible light illumination demonstrate that the optimal photocatalytic H₂-evolution rate for Ni(OH)₂-2.5%/TpPa-2 is up to 1895.99 μmol h⁻¹ g⁻¹ [Fig. 22(b) and (c)]. The considerable increase in the charge separation capabilities in this instance is due to the coexistence of Ni(OH)₂ and metallic Ni, which also results in improved photocatalytic performance that is comparable to the Pt co-catalyst [Fig. 22(d)] [246]. In another report, Deng et al. constructed a covalent organic framework photocatalyst with a neighboring hydroxyl group and an imine bond in each constitutional unit to achieve high dispersion in situ photodeposition of Pt clusters on the 2D COF surface layer (Fig. 22(e)). On the covalent organic framework, the widespread platinum clusters reveal a con-

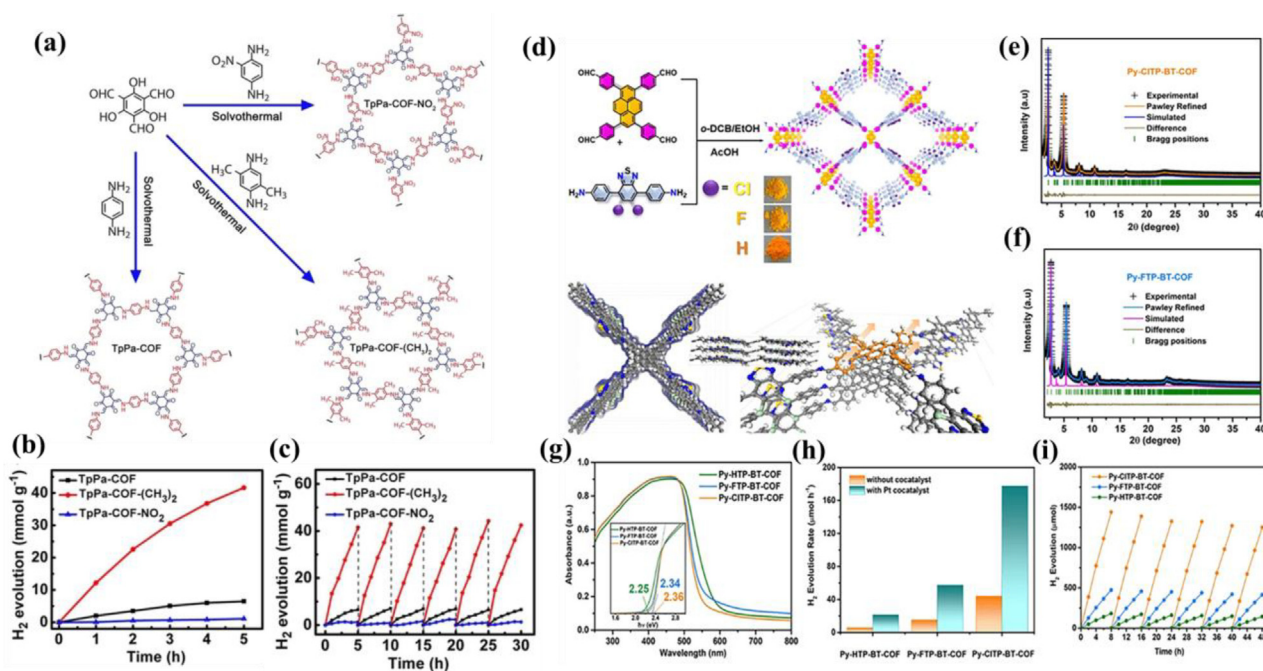


Fig. 21. (a) Schematic illustration of the synthesis of TpPa COF X, (b) The photocatalytic H₂ evolution activities and (c) The photocatalytic stability of TpPa COF X. d) Synthetic routes of Py-XTP-BT-COFs under solvothermal conditions and Top view (left), side view (middle) and partial enlarged detail (right) of AA stacking mode of Py-CITP-BT-COF, which indicate the armchair conformations of the central pyrene moieties. e), f) Experimental and simulated PXRD patterns of Py-FTP-BT-COF and Py-CITP-BT-COF. g) UV-vis and Tauc plot of Py-HTP-BT-COF, Py-FTP-BT-COF and Py-CITP-BT-COF, h) hydrogen evolution rate of Py-HTP-BT-COF, Py-FTP-BT-COF and Py-CITP-BT-COF with and without Pt-cocatalyst, i) Time course stability of Py-HTP-BT-COF, Py-FTP-BT-COF and Py-CITP-BT-COF for 48 h. Reproduced from Ref. [244,245] with permission of the John Wiley and Sons.

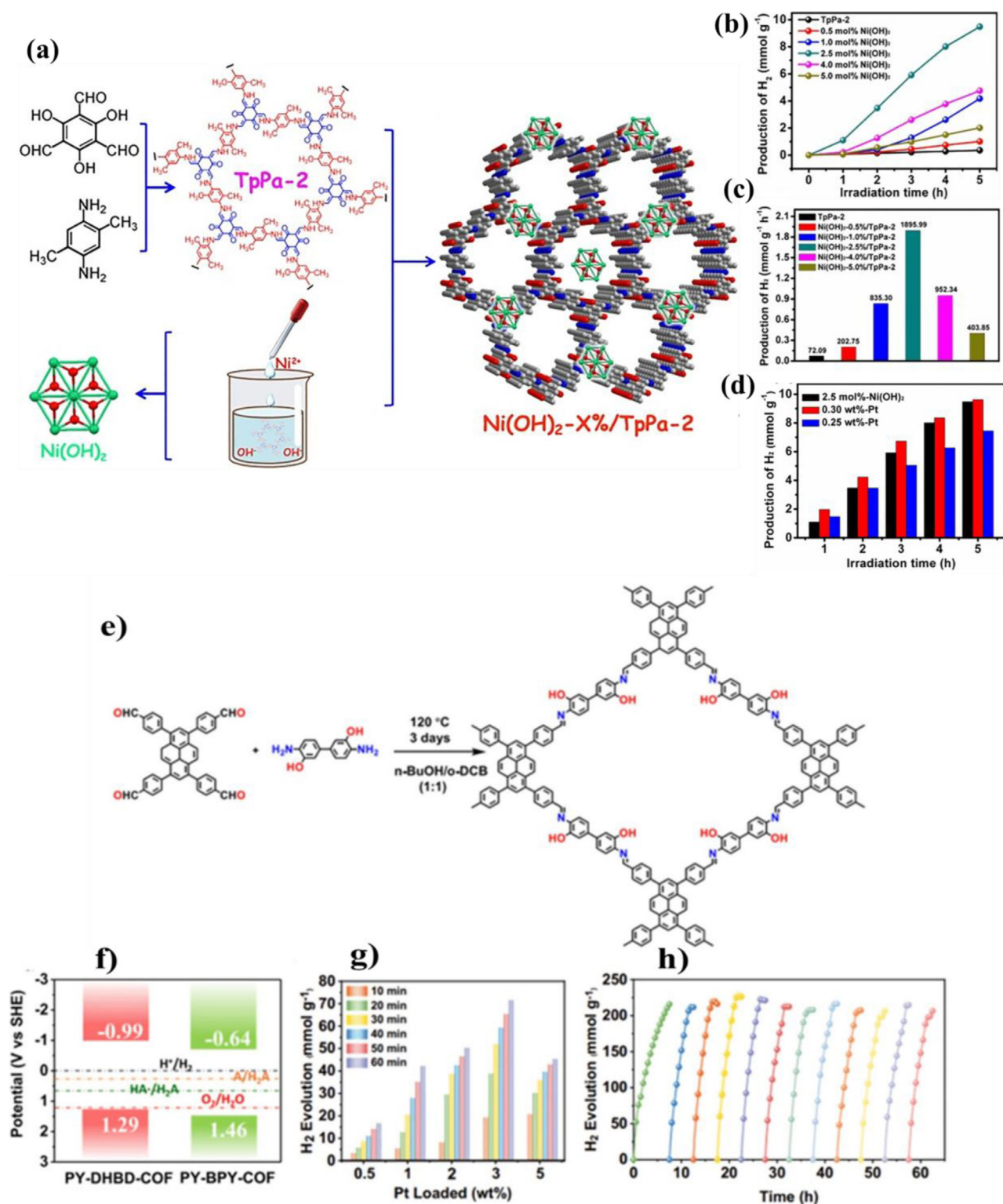


Fig. 22. (a) Schematic synthesis of a series of Ni(OH)₂-X%/TpPa-2 composite materials. (b-c) Comparison of photocatalytic H₂ evolution activity of series of Ni(OH)₂-X%/TpPa-2 and TpPa-2. (d) The photocatalytic stability of Ni(OH)₂-2.5%/TpPa-2. (e) Synthesis process and structure of PY-DHBD-COF. (f) Energy band positions of COFs. (g) Time dependent hydrogen evolution for PY-DHBD-COF with different Pt loading amount. (h) Long-term hydrogen production for 3 wt% Pt loaded PY-DHBD-COF. Reproduced from Ref. [246] with permission of the Elsevier.

siderable active surface and substantially simplify the electron transport. This study shows how to take full use of the designable and customizable pore structure of a COF to create an effective photocatalyst by controlling the deposition of photocatalytic co-catalysts at the atomic level. The neighboring imine-N and regu-

larly spaced hydroxyl groups on the structural units help to provide the best adsorption sites for the Pt precursor, resulting in the uniform in situ photodeposition of Pt co-catalysts at lengths ranging from single atoms to tiny clusters and nanoparticles, considerably enhancing the spatial charge transfer between the COF

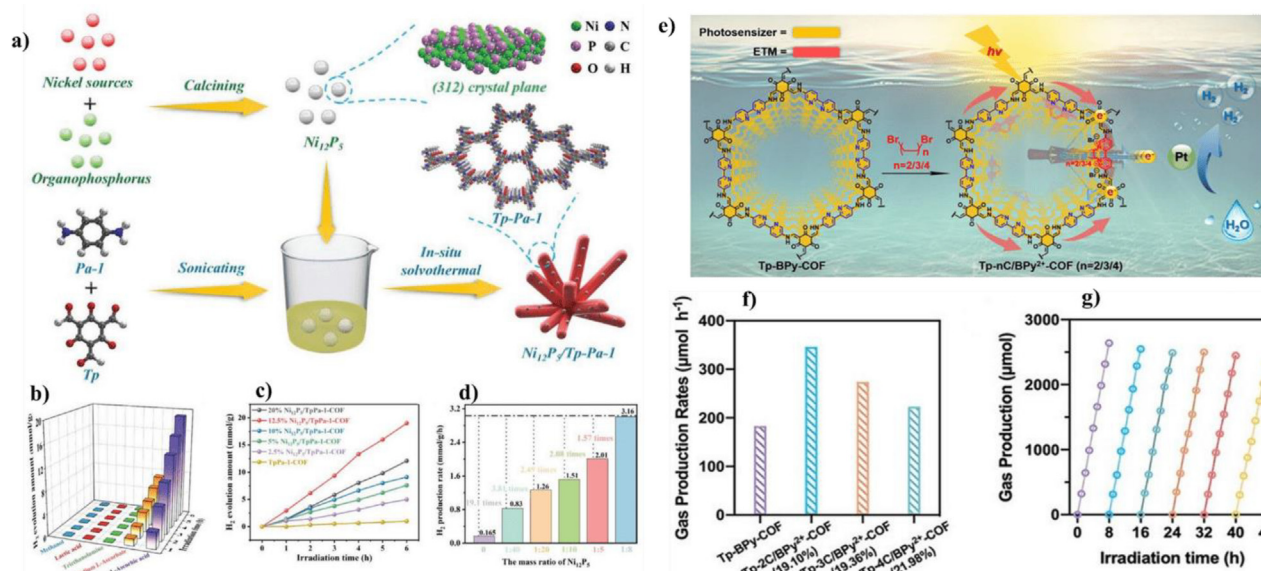


Fig. 23. (a) Schematic of the synthetic process for the $\text{Ni}_{12}\text{P}_5/\text{TpPa-1-COF}$ composite. (b) Photocatalytic hydrogen evolution efficiency of 12.5% $\text{Ni}_{12}\text{P}_5/\text{TpPa-1-COF}$ under different sacrificial systems. (c) Photocatalytic H_2 evolution amount comparison for the series of $\text{Ni}_{12}\text{P}_5/\text{TpPa-1-COF}$ composites under different times. (d) Photocatalytic H_2 production rates for TpPa-1-COF and TpPa-1-COF composites containing different amounts of Ni_{12}P_5 . (e) Schematic diagram for BPY^{2+} -accelerated photocatalytic hydrogen evolution from water splitting by virtue of electron-transfer effect. (f) 8-h HERs of Tp-BPy-COF and three quaternized $\text{Tp-nC/BPy}^{2+}\text{-COFs}$ ($n = 2, 3, 4$) with roughly 20 mol.% of cyclic diquats. (g) Photocatalytic hydrogen generation with $\text{Tp-2C/BPy}^{2+}\text{-COF}$ (19.10 %) upon a 48 h visible irradiation ($\lambda > 420 \text{ nm}$). Reproduced from Ref. [247] with permission of the John Wiley and Sons.

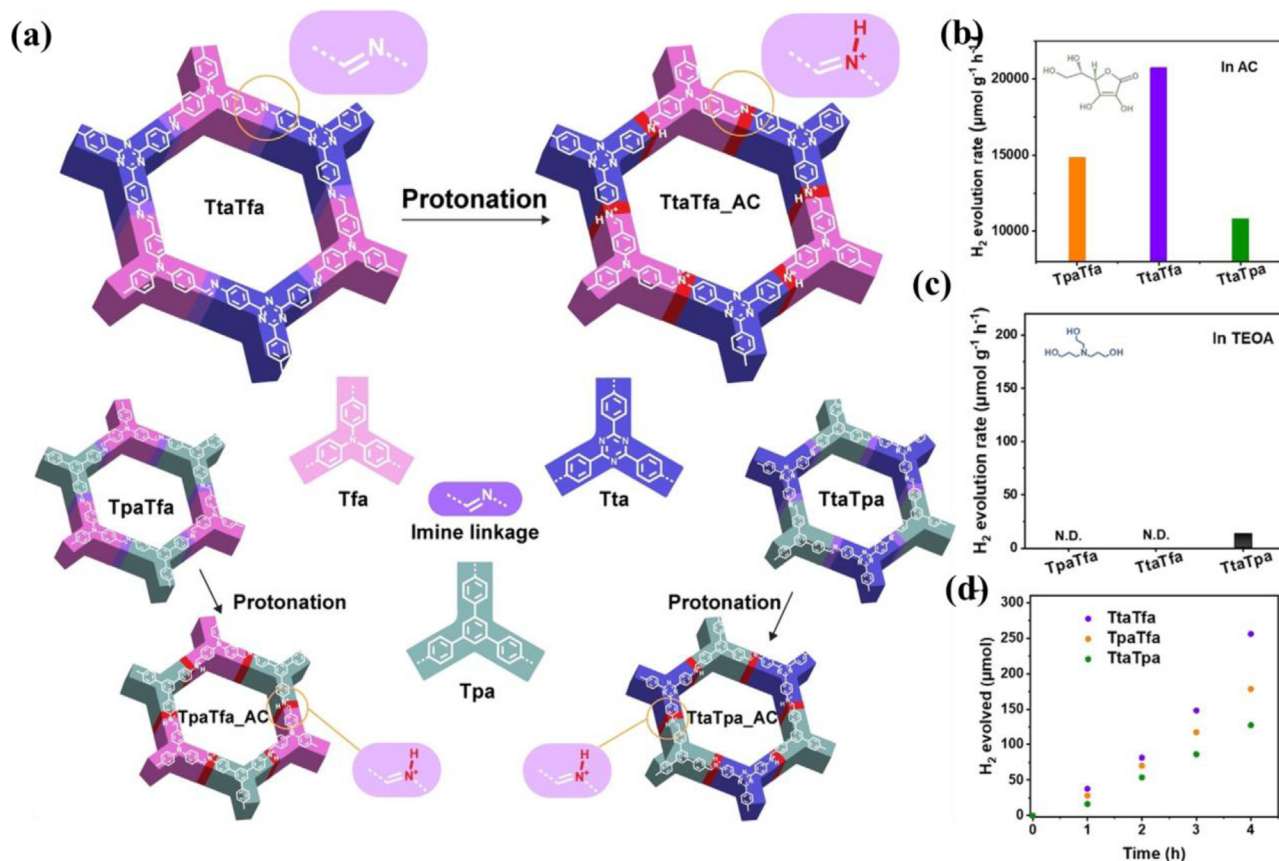


Fig. 24. (a) Synthesis of the COFs studied in this work. Scheme of synthesis of TtaTfa, TtaTfa AC, TpaTfa, TpaTfa AC, TtaTpa, and TpaTpa AC. AC = ascorbic acid modification. (b) Time course of photocatalytic H_2 evolution for TtaTfa, TpaTfa, and TtaTpa using AC as SED (3 mg catalyst, 16 mL 0.1 M AC aqueous solution, 3 μL H_2PtCl_6 (8 wt%), $\lambda > 420 \text{ nm}$, 20 °C). Comparison of photocatalytic HER rates of the above COFs using (c) AC as SED and using (d) TEOA as SED (5 mg catalyst, 16 mL water, 2 mL TEOA, 5 μL H_2PtCl_6 (8 wt%), $\lambda > 420 \text{ nm}$, 20 °C). Reproduced from Ref. [249] with permission of the John Wiley and Sons.

and co-catalyst (Fig. 22(f-h)) [241]. In order to achieve visible-light-driven water splitting, it is urgently necessary to investigate the alternatives to the noble metal co-catalysts and create effective noble-metal-free photocatalysts due to the disadvantages of high cost, limited resources, and easy accumulation for the noble metal co-catalysts (e.g., Pt, Au, Pd). The transition metal phosphides have been demonstrated to be a form of prospective non-noble metal co-catalysts and have the benefits of rich resources, numerous active sites, good charge transfer, and adjustable structure among other non-noble metal co-catalyst kinds. Ma et al. have successfully combined TpPa-1-COF with transition metal phosphide (TMPs) via a direct solvothermal approach to create a series of noble-metal-free photocatalysts called TMPs/TpPa-1-COF. The Ni_{12}P_5 /TpPa-1-COF demonstrates the highest activity for solar-driven water splitting and is equivalent to the Pt/TpPa-1-COF because it has more reactive sites than Ni_2P and CoP and lower energy barriers for H_2 production (Fig. 23a) [247]. Without the using of a noble metal co-catalyst, the Ni_{12}P_5 /TpPa-1-COF can effectively convert water to H_2 under visible light irradiation, with an H_2 production rate of up to $31.6 \mu\text{mol h}^{-1}$ (Fig. 23b-d). As well known, electron-transfer mediators (ETMs) have a dual role in accepting and donating electrons in a dynamic equilibrium, as well as sustaining electron-transfer processes to improve reaction efficiency. A post-synthetic approach to engineering the site-isolated ETM modules on a COF based on 2,2'-bipyridine has been proposed by Guo and co-workers (Fig. 23e). The distribution and content of implanted diquat-ETMs are meticulously managed, resulting in the advantageous site isolation arrangement. When compared to a single-module COF and a COF/ETM combination, the resultant materials demonstrate an elevated hydrogen evolution rate ($346 \mu\text{mol h}^{-1}$) with long-term photocatalytic activity for H_2 production (Fig. 23(f, g)) and sustained performances because they

combine photosensitizing units and ETMs into a single system. They are individually immobilized on the various sites and segregated from one another due to the combined impact of electrostatic repulsion and steric hinderance, which prevents the production of stable -stacked cationic radicals during the electron transfer process [248]. In 2021, Thomas and his co-workers investigated the impact of protonation on the efficiency of photocatalysts based on imine-COFs (Fig. 24a). In this work three 2D imine-linked COFs were constructed. When using an acidic SED (ascorbic acid), these imine COFs exhibit strong photocatalytic HER reactivity (Fig. 24b), while very little H_2 was generated in an alkaline condition (TEOA as SED) (Fig. 24c). The protonation of the imine linkage is responsible for the strong photocatalytic HER activity of these COFs (Fig. 24d) [249]. Linkage chemistry frequently impacts the chemical stability and electron transport of COFs, which is crucial for photochemical reactions. Yan and his team investigated the effect of different linkages on the HER activity using three COFs with the same triazine benzene as a junction and phenyl as a connector, with different linkages monomer (Fig. 25a). They were built as the imide-COF (PMDA-COF), imine-COF (DHTA-COF), and imine-COF (TPAL-COF), respectively. According to photocatalysis studies, PMDA-COF has a HER activity of $435.6 \mu\text{mol h}^{-1} \text{g}^{-1}$, which is much greater than the HER activities of DHTA-COF and TPAL-COF over a 20-hour exposure (Fig. 25b-d). It's worth mentioning, PMDA-COF is much better at separating photogenerated charge and light-absorption intensity than DHTA-COF and TPAL-COF based on their photochemical properties. These results revealed that PMDA and TAPT differ in energy, which forms a D-A heterostructure between them, allowing not only for the modification of the electronic band structure but also for the separation of reduction and oxidation sites. Furthermore, due to hydrogen bonds formed between carbonyl groups and water mole-

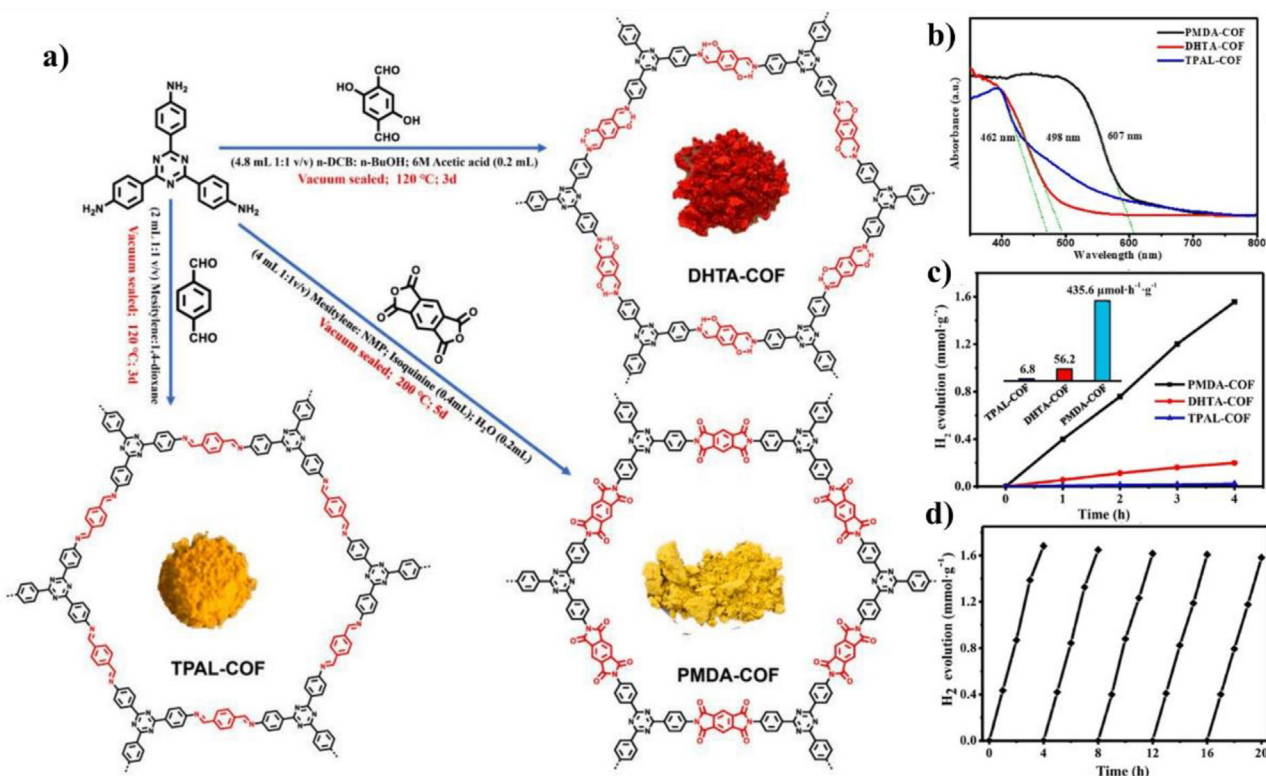


Fig. 25. (a) Schematic illustration of the synthesis of PMDA-COF, DHTA-COF, and TPAL-COF, (b) UV-vis diffuse reflectance spectra PMDA-COF, DHTA-COF, and TPAL-COF, (c) H_2 evolution rates of PMDA-COF, DHTA-COF, and TPAL-COF under visible light irradiation ($\lambda > 420 \text{ nm}$) using TEOA solution (10% in volume) as sacrificial agent and Pt (3 wt%) as co-catalyst. The inset is the comparison of H_2 evolution rate, (d) Typical time course of hydrogen production under visible light irradiation using PMDA-COF for 20 h. Reproduced from Ref. [250] with permission of the Elsevier.

cules in PMDA-COF, the photocatalytic reaction advances. Therefore, inhibiting the combination of electrons and holes [250]. Interestingly, the function of metal active sites in increased photocatalytic performance for H₂ evolution is not adequately discussed. Zhang et al. successfully synthesized a single-atom Pt anchored on -ketoenamine-linked TpPa-1-COF with 2D structural properties by integrating its microporous structure and unsaturated coordination toward water splitting to H₂ generation (Fig. 26a). The enhanced photocatalytic performance for H₂ evolution is attributed to excellent photogenerated charge separation and migration, as well as well-dispersed active sites of single-atom Pt (Fig. 26b-d) [251]. Recently, construction of 2D COFs for heterogeneous photocatalysis has been carried out using porphyrin and its derivatives, a class of conjugated macrocycles with distinctive photophysical and redox characteristics. The insertion of various metal ions into porphyrin units can rationally modify their photophysical and electrical characteristics, influencing the photocatalytic activity of related COFs. To investigate the structure–property–activity link in photocatalytic HER at the molecular level, Wang et al., presented the planned synthesis and characterization of four isostructural porphyrinic 2D COFs, which have a broad pore surface and a high crystallinity (Fig. 27a). It's interesting to note that the photo-

physical and electrical characteristics of the porphyrinic COFs may be changed by adding various transition metals to the porphyrin rings. These COFs demonstrated a variable rate of photocatalytic hydrogen synthesis, which is mostly attributable to their molecularly engineered charge-carrier dynamics. The amount of hydrogen evolution of ZnPor-DEATH-COF has higher efficiency than CoPor-DETH-COF and NiPorDETH-COF (Fig. 27b, c). Because the ZnPor-DETHCOF holes can freely travel through the macrocycle-macrocycle channel to the surface and transfer electrons through the Zn...Zn chain, resulting in a long-time charge separation state (Fig. 27d) [252]. Many synthetic factors play an invisible role in the crystallization of COFs, and the nature of the solvent is one of the most influential. Chou et al. investigated the influence of solvent polarity on the crystallinity of a COF synthesis product and its effect on photocatalytic H₂ evolution. According to PXRD, the formation of crystalline COFs is substantially facilitated when a highly polar organic solvent is used as the reaction medium. Therefore, the ease with which the COFs crystallize depends on the solvent's polarity or capacity to act as a hydrogen bond donor. This is due to the fact that the values of interaction energy (E_a) fall as the polarity of the solvents increases, which speeds up crystal formation. Such increased crystallinity COFs may be advantageous for improving hydrogen evolution rates when driven by visible light.

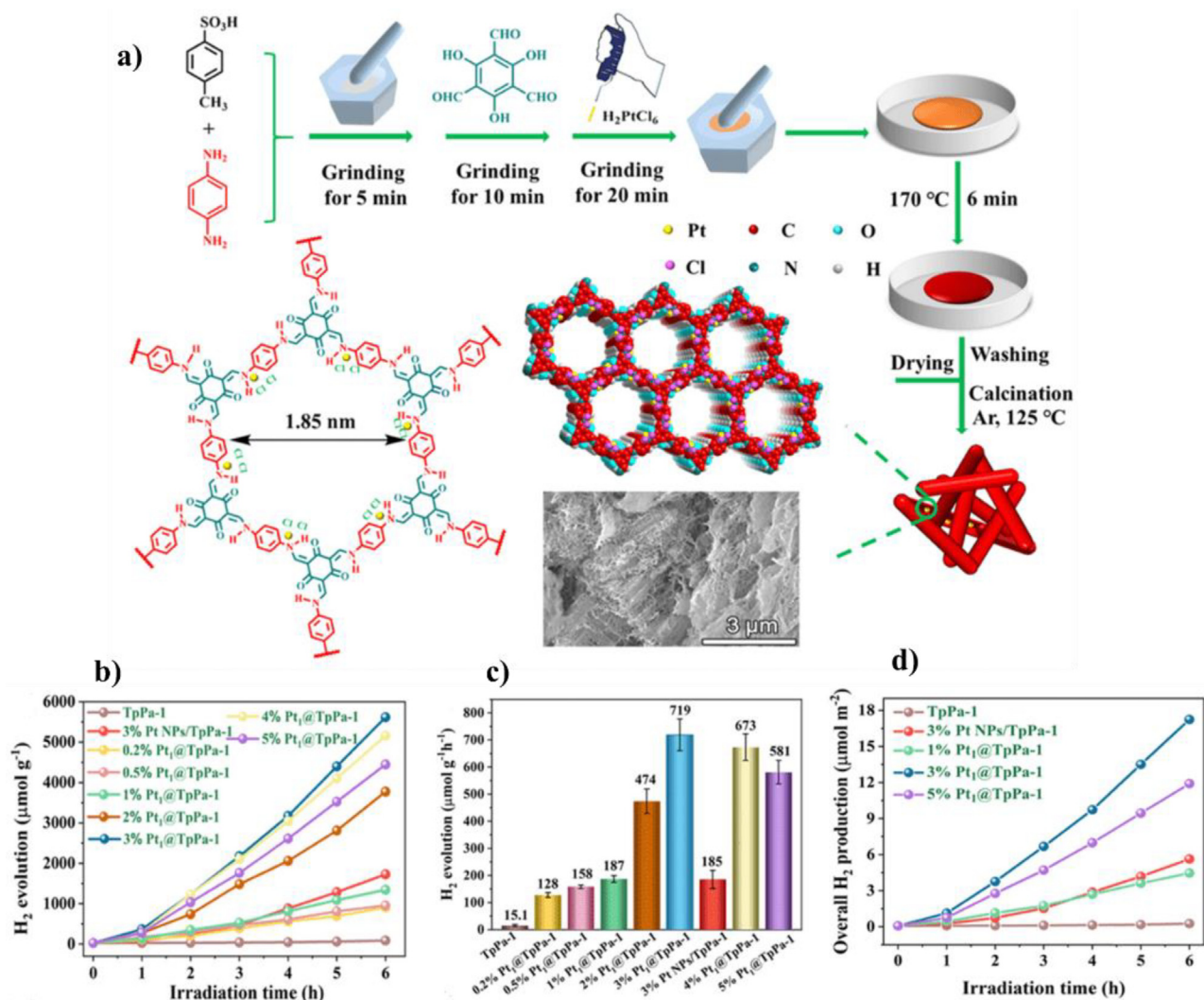


Fig. 26. (a) Schematic illustration for the Preparation of Single-Atom Pt Anchored on TpPa-1-COF (Denoted as Pt₁@TpPa-1). (b) Photocatalytic performance for H₂ evolution per unit mass. (c) Photocatalytic H₂ evolution bar chart of all samples with error bars. (d) Photocatalytic performance for H₂ evolution per unit surface area. Reproduced from Ref. [251] with permission of the American Chemical Society.

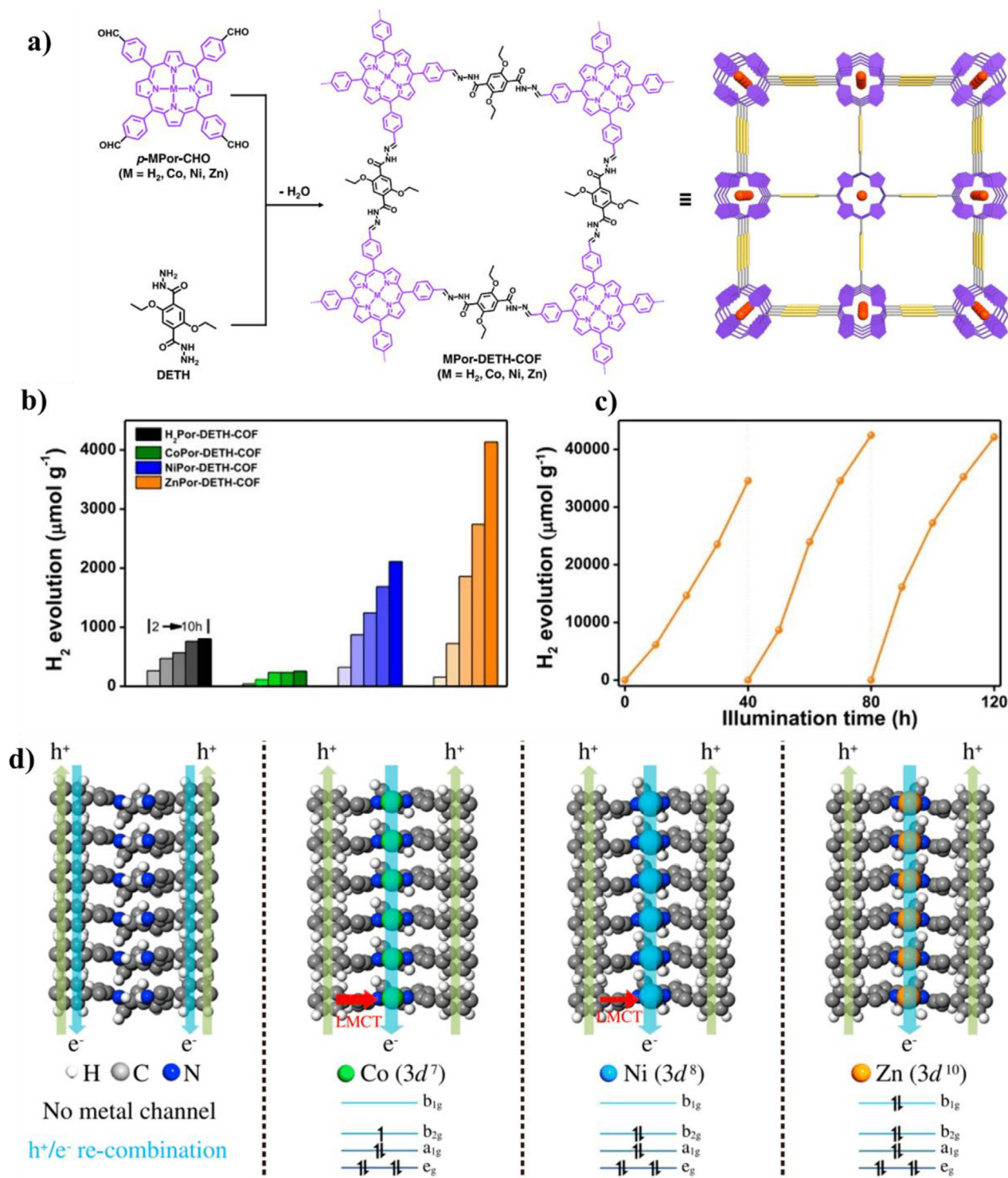


Fig. 27. (a) Schematic representation of the synthesis of MPor-DETH-COFs. (b) Time dependent H₂ photogeneration using visible light for H₂Por-DETH-COF, CoPor-DETH-COF, NiPor-DETH-COF and ZnPor-DETH-COF. (c) Long-term H₂ production using visible light for ZnPor-DETH-COF for 120 h (recycled every 40 h for three times). (d) The isosurface of the electron orbitals of blue VBM and magenta CBM (upper panel) and schematic illustrations of the hole-electron transport processes (lower panel) in MPor-DETH-COFs: H₂Por-DETH-COF; CoPor-DETH-COF; NiPor-DETH-COF, and ZnPor-DETH-COF. The balls in different colors represent different atoms: H, white; C, grey; N, blue; Co, olive green; Ni, light blue; Zn, orange. Reproduced from Ref. [252] with permission of the Springer Nature.

This study demonstrated that increasing the solvent polarity increased the crystallinity as well as the thermal stability and produced highly crystalline COFs in a shorter period of time (30 min) [253]. Various methods have been reported for the synthesis of new types of COF/MOF materials. Zou et al. investigated the com-

bination of COF and MOF for enhanced hydrogen evolution reaction activity using an in-situ ligand self-assembly technique (Fig. 28a). The in situ modified bonds act as a route for the quick transmission of photogenerated electrons without forming new chemical bonds, in addition to acting as nucleation sites for the

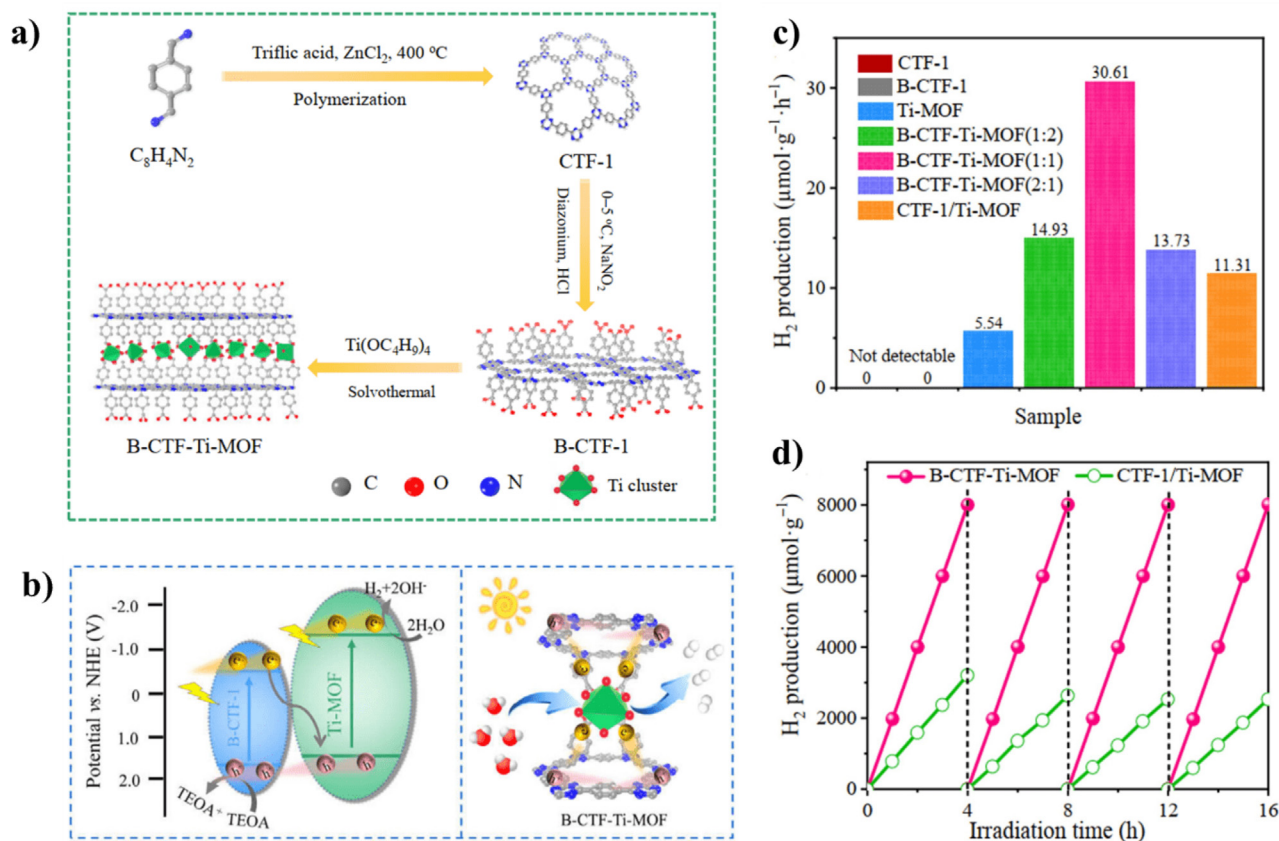


Fig. 28. (a) Schematic of B-CTF-Ti-MOF composite preparation process. (b) Photocatalytic H₂ production over the as-obtained samples under simulated sunlight irradiation without co-catalyst. (c) Recyclability of the H₂ evolution over B-CTF-Ti-MOF and CTF-1/Ti-MOF irradiated under simulated sunlight. (d) Possible photocatalytic mechanism for the H₂ evolution reaction over B-CTF-Ti-MOF under light irradiation. Reproduced from Ref. [254] with permission of the Elsevier.

production of Ti-MOF. A possible photocatalytic hydrogen generation reaction mechanism for B-CTF-Ti-MOF has been proposed and illustrated in Fig. 28b. When compared to the independently generated optical band gap (CTF-1/Ti-MOF) and its constituent components, the resultant B-CTF-Ti-MOF exhibits better activity and exceptional stability of hydrogen synthesis under simulated sunlight irradiation (Fig. 28c, d) [254]. Yang et al., synthesis of a cyano-containing COF (CYANO-COF) with ketene-cyano (D-A) pair for photocatalytic HER (Fig. 29a). The presented cyano group improves the optical properties (Fig. 29b, c). A significant thirtyfold increase in the H₂ evolution rate of CYANO-COF compared to BD-COF demonstrated the promoting effect of cyano groups in HER photocatalysis (Fig. 29d). CYANO-COF achieved an AQE of up to 82.6% at 450 nm, superior to all reported polymer semiconductors in photocatalytic HER so far (Fig. 29e-h). The high charge separation efficiency could be the main reason for the excellent HER photocatalytic activity of CYANO-COF as indicated by the temperature-dependent PL spectroscopy and fs-TA spectroscopy properties [255].

7.1.2. COF for photocatalytic OER

Based on topological techniques and first-principles computations, Yang et al., developed many experimentally viable 2D-COFs capable of splitting water by visible light. By synthesizing certain linkages and building blocks that have catalytic activity toward either HER or OER. The chemical reaction potentials of H₂/H⁺ and O₂/H₂O, which are capable of photocatalytic water splitting, are well matched by the locations of both CBM and VBM of nine 2D COFs. This study not only fulfills the computational design and

experimental results of 2D COF photocatalysts for water splitting, but also gives a path for constructing 2D process COFs as metal-free, single-material photocatalysts for water splitting from functional molecules under visible light (Fig. 30a-c) [256].

7.1.3. COF for photocatalytic overall water splitting

Photocatalytic overall water splitting has been identified as an optimal and promising technique to realizing a sustainable energy development plan that directly creates clean hydrogen (H₂) and oxygen (O₂) from water using sun energy as a driving force. The development of an efficient photocatalytic system for overall water splitting generally involves significant obstacles. firstly, a suitable bandgap is required to absorb the light. Second, large thermodynamic functions are required for the O₂ generation of multiple electron and proton transfers. Finally, the photogenerated electron-hole pairs must be efficiently separated and transferred to redox-active sites. Jin et al. investigated an innovative polycondensation procedure based on benzylamine-functionalized monomer to effectively manufacture crystalline CTFs and observed that the base reagent has a substantial influence on the crystalline structure of the CTFs. For the first time, CTF-HUST-A1 photocatalytic overall water splitting was obtained without the need of a sacrificial agent. Photocatalytic overall water splitting is performed by depositing dual co-catalysts in CTFHUST-A1, with H₂ evolution and O₂ evolution rates of 25.4 μmol·g⁻¹·h⁻¹ and 12.9 μmol·g⁻¹·h⁻¹ in pure water, respectively, without the need of a sacrificial agent (Fig. 31a-f) [257]. Table 3 summarizes of properties and H₂ evolution activity and quantum efficiency for COF-based photocatalytic systems [241,243,245,246,249-254,257-261].

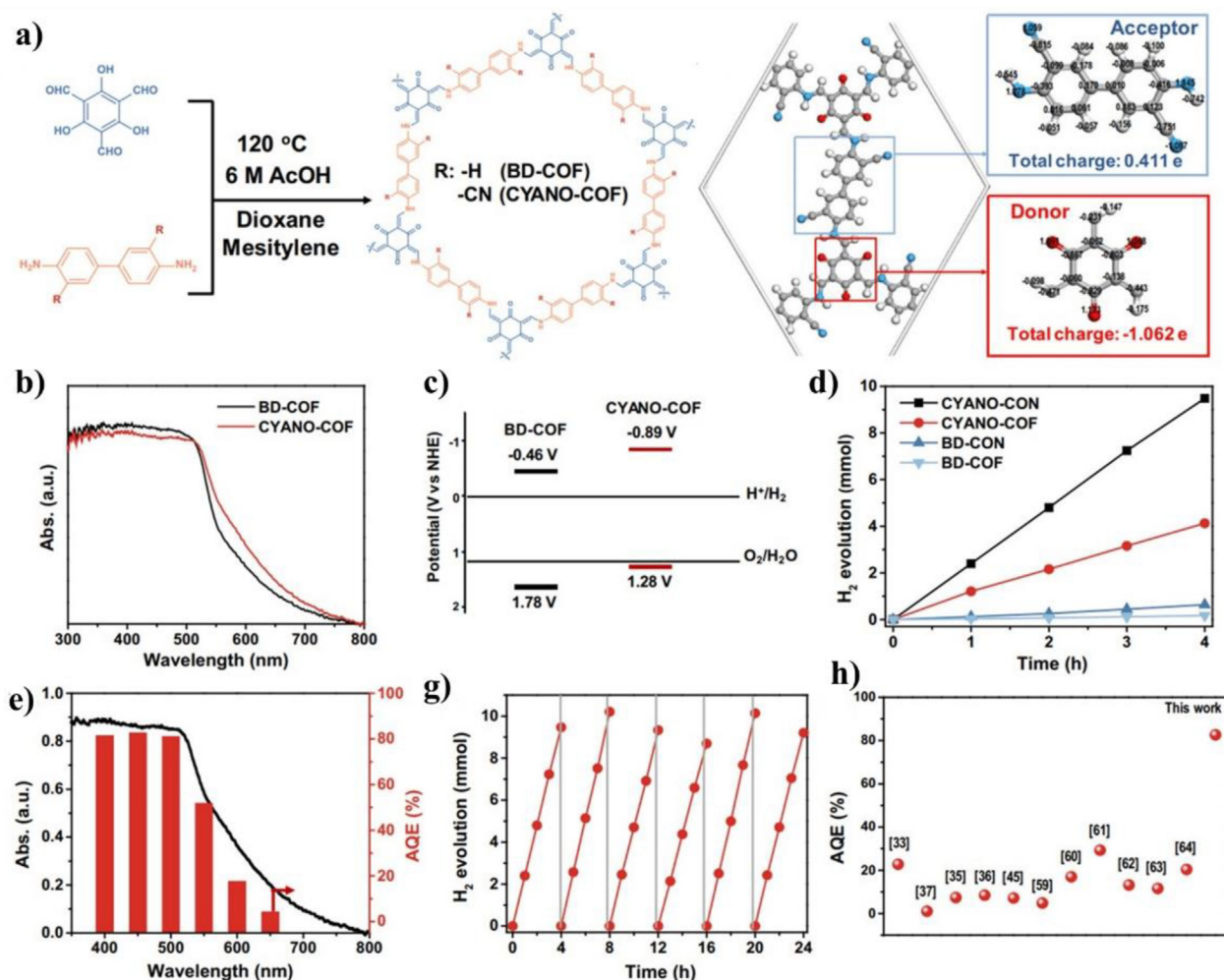


Fig. 29. (a) Synthesis of CYANO-COF and BD-COF. (b) Charge distribution in CYANO-COF structure. (c) UV-vis DRS spectra of BD-COF and CYANO-COF. (d) Schematic energy band structures of BD-COF and CYANO-COF. (e) Time course of photocatalytic H_2 production for different COFs and CONS. (f) Wavelength-dependent AQE of photocatalytic H_2 production for CYANO-CON. (g) Cycling stability for CYANO-CON in photocatalytic H_2 production. (h) AQE of HER for state-of-the-art representative COFs and conjugated polymers. Reproduced from Ref. [255] with permission of the Springer Nature.

8. COFs for electrocatalytic HER, OER, and overall water splitting

It has enormous potential for resolving the present energy crisis and environmental issues by using electrocatalytic water splitting to make hydrogen utilizing different renewable energy sources (such as wind or solar energy, etc.) [262,263]. Two half-reactions are involved: the oxygen evolution reaction (OER) at the anode and the hydrogen evolution reaction (HER) at the cathode. Prospective earth-abundant metal-based electrocatalysts for water splitting would typically have the following characteristics: 1) High-performance materials based on noble metals, 2) across a wide pH range, good catalytic activity, 3) high durability and consistent performance, 4) Eco-friendliness, 5) Cheap and abundant sources; 6) capabilities to incorporate both OER and HER in a cell [263,264].

8.1. COFs for electrocatalytic HER

A significant part of the water splitting process is composed of two half-reactions, namely hydrogen evolution and oxygen evolution. These reactions have been studied and optimized separately in many cases. Hydrogen and oxygen can be separated from water by applying a thermodynamic voltage of 1.23 V (25 °C). It is generally necessary to apply a voltage exceeding the thermodynamic potential due to existing resistances (such as solution and contact

resistances) and intrinsic activation barriers on electrodes. Overpotential is a term used to describe the excess potential that is needed. This overpotential must be decreased by using effective and reliable catalysts to accomplish efficient water splitting. HER electrocatalyst performance can also be evaluated by considering its current density, Tafel slope, stability, and faradaic efficiency, in addition to the overpotential. A catalyst's electrocatalytic activity is determined by its current density. Various voltages are applied to each sample to determine the current density, and then the current density is normalized by the mass of the sample or the geometric area of the electrode ($mA\ mg^{-1}$). For comparison purposes, the overpotential in HER at a current density of $10\ mA\ cm^{-2}$ (expected for a 12.3 % efficient solar water-splitting device) is intentionally provided to compare the activities of the electrocatalysts. The Tafel plot depicts the relationship between current density (j) and overpotential (η), and the Tafel equation ($\eta = b \log(j) + a$) is used to describe the linear portion of the Tafel plot, where the linear slope b is defined as the Tafel slope, and the values of b reflect the several catalytic mechanisms involved in electrode reactions. A stability test is performed to determine whether the HER catalyst is practical. Chronoamperometry and chronopotentiometry measurements are employed for characterizing electrocatalytic stability.³ Using a ratio of the theoretical to the experimental hydrogen production, the faradaic efficiency is calcu-

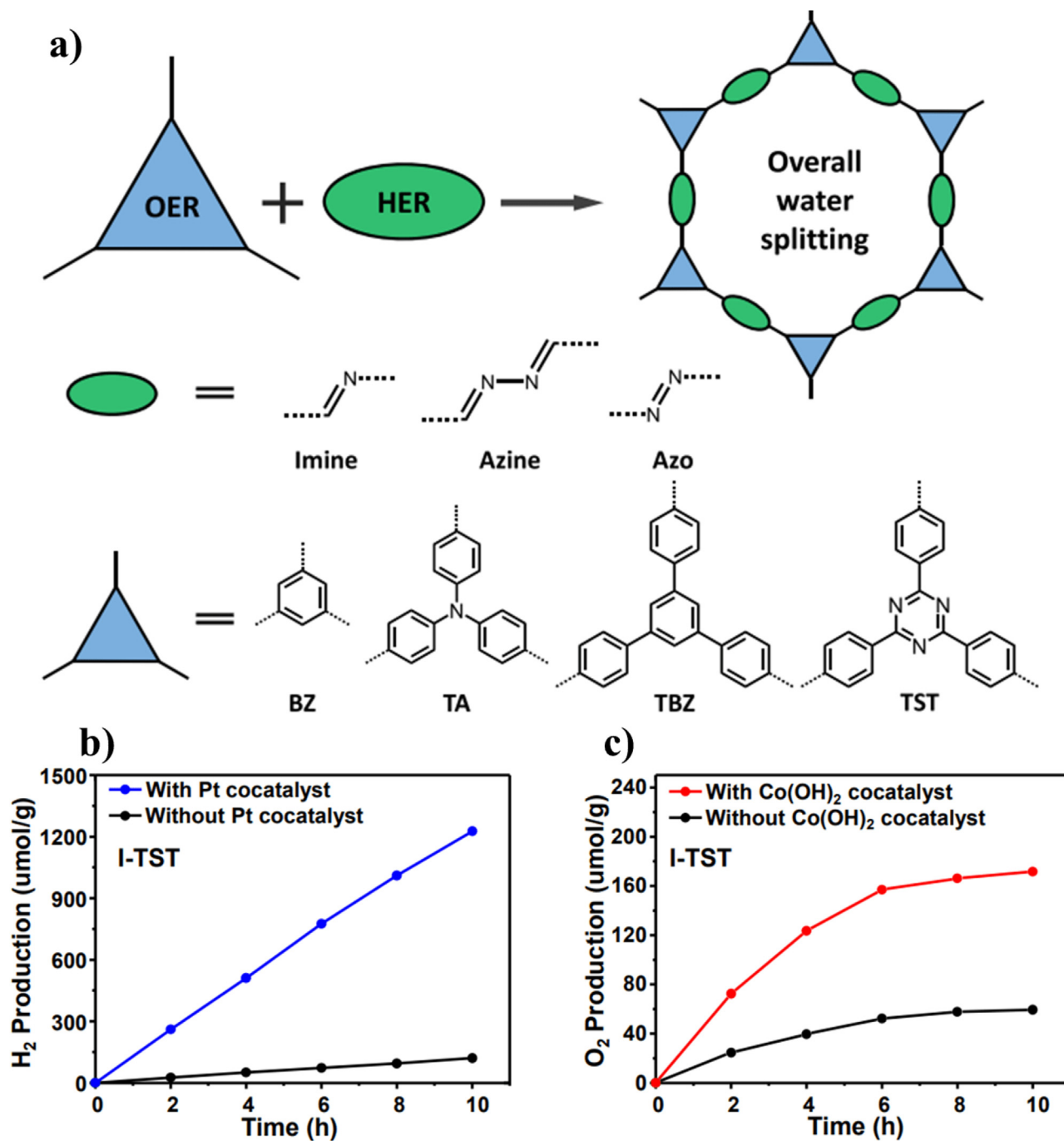


Fig. 30. (a) Schematic illustration of structure and design principles of 2D NL COFs for photocatalytic hydrogen and oxygen evolution. The photocatalytic water splitting performance of I-TST for (b) H₂ and (c) O₂ evolution. Reproduced from Ref. [256] with permission of the American Chemical Society.

lated, which describes the efficiency with which electrons are utilized to produce hydrogen. In both acidic and alkaline solutions, as shown in Table 4, the mechanism of the HER involves three steps. Protons, water, dihydrogen, and their intermediates are adsorbed, reduced, and desorbed on the catalyst surface during the H₂ evolution process. During proton reduction, hydrogen is adsorption on the catalyst surface (H*, where * represents an active site). Following the combination of hydrogen, either a Heyrovsky process or the Tafel process leads to the formation of molecule hydrogen. A nearly zero ΔG_H^* indicates that an optimal HER catalyst is described by the free energy of hydrogen adsorption, which is determined by DFT calculations. Based on theoretical and experimental studies,

a platinum-based electrocatalyst is determined to be the most efficient electrocatalyst for HER. Despite that, the high cost and scarcity of platinum make it difficult for the metal to be widely used. It is desirable to create HER electrocatalysts made of materials found on Earth to produce hydrogen at a low cost [265–267]. Materials such as transition metal dichalcogenides [268,269], carbon-based materials [270,271], single metal atom-doped materials [272–274], and polymeric materials [275–277] have been studied and applied for hydrogen production. In general, three active centers are found on COF-based electrocatalysts for the HER: N-dopant heteroatoms, single atom sites (e.g., Pt), and M–N–C hybrid structures obtained after carbonization. Recent reports suggest that

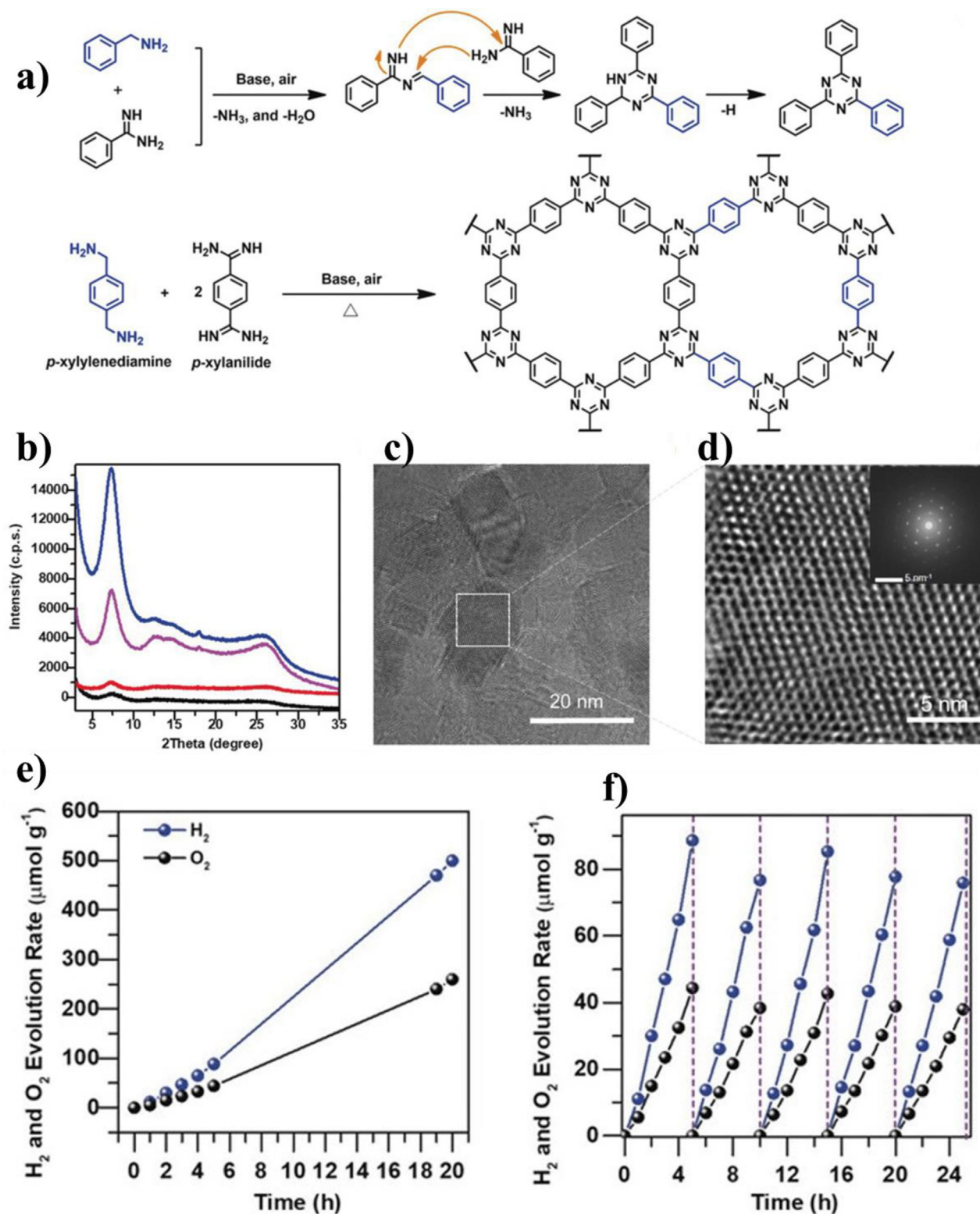


Fig. 31. a) Proposed mechanism for the synthesis of the triazine structure from benzylamine. b) Synthesis route of CTF-HUST-A1 from benzylamine-functionalized monomer and amidine monomer. c) PXRD pattern of CTF-HUST-A1 synthesized in different base reagents after treating with supercritical CO₂, CTF-HUST-A1-K₂CO₃ (black), CTF HUST-A1-KOH (red), CTF-HUST-A1-EtOK (pink), CTF-HUST-A1-tBuOK (blue). d) HR-TEM image of CTF-HUST-A1-tBuOK with a scale bar of 20 nm. f) HR-TEM image of CTF-HUST-A1-tBuOK with a scale bar of 5 nm (Inset: the FFT of CTF-HUST-A1-tBuOK). e) Time course of photocatalytic overall water splitting of CTF-HUST-A1-tBuOK under visible light irradiation ($\lambda > 420$ nm) in pure water. f) Recyclability test of CTF-HUST-A1 sample in the photocatalytic overall water splitting. Reproduced from Ref. [257] with permission of the John Wiley and Sons.

Table 3
Summary of properties and H₂ evolution activity and quantum efficiency for COF-based photocatalytic systems.

COF	BET (m ² g ⁻¹)	B _g (eV)	HER conditions	HER (mmol g ⁻¹ h ⁻¹)	AQY (%) at 420 nm	Ref.
TpPa COFTpPa COF (CH ₃) ₂	541.71	2.09	10 mg COF, 50 mL PBS 100 mg SA, 3 %Pt	1.56		[258]
TpPa COF NO ₂	348.88	2.06		8.33	n.a	
CTF	162.93	1.92		0.22		
P-COF-1	455	2.63	20 mg catalysts, 50 mL H ₂ O, 10 vol %TEOA	5.55	n.a	[259]
5 % P-COF-1/CTF	973	2.30		0.067		
PyTA-BC COF	497	2.52		14.1		
PyTA-BC-Ph COF	520	2.71	1 mg COF, H ₂ O /MeOH, 0.1 M AA	1.183	1.46	[260]
Py-HTP-BT-COF	1445	2.67		0.417	1.83	
Py-CITP-BT-COF	1841	2.25	20 mg COF, AA, 5 % Pt	1.08	n.a	[245]
PyFTP-BT-COF	1012	2.36		2.88	8.45	
CTF-HUST-A1	1016	2.34		8.88	n.a	
Ni(OH) ₂ -2.5 %/TpPa-2	644	2.35	50 mg COF, TEOA	9.20	7.4	[257]
BtCOF150	472.76	2.07	10 mg catalyst, PBS Buffer, SA	1.89		[246]
Tp-2C/BPy ²⁺ -COF (19.10 %)	554	2.1	20 mg COF, TEOA, 1 %Pt	0.75	0.20	[243]
TtaTfa	1359	2.16	10 mg COF, 0.1 M AA, 3 wt% Pt	3.46	6.93	[248]
Tta-TP	1258	2.52	3 mg COF, AA, Pt	20.7	1.43	[249]
PMDA-COF	961.68	1.73	5 mg catalyst, 0.1 M AA, 2.2 % Pt	6.28	0.64	[261]
3 % Pt1@TpPa-1	2450.2	1.99	10 mg catalyst, TEOA, 3 %Pt	0.435	n.a	[191]
H2Por-DETH-COF	326	1.94	40 mg COF, PBS buffer, SA	99.86	0.38	[192]
CoPor-DETH-COF	826	1.77		0.080	n.a	[193]
NiPor-DETH-COF	942	1.88	2.5 mg COF, TEOA, Pt	0.025	n.an	
ZnPor-DETH-COF	773	1.82		0.211	.a	
B-CTF	1020	1.88		0.413	0.32	
Ti-MOF	n.a	2.25	20 mg catalyst, TEOA, 3 %wt Pt	0.181	n.an	[195]
B-CTF/Ti-MOF	n.a	2.78		0.261	.a	
CYANO-CON	356	2.17	20 mg COF, 0.1 M AA, 1 %wt Pt	1.975	4.76	
CYANO-COF	559	2.17		134.200	82.6	[196]
PY-BPY-COF.	1893	2.28	10 mg catalyst, AA, 0.5 %wt Pt	60.850	n.a	
TpPa-1-COF	919	2.10	10mgCOF,AA,Ni ₁₂ P ₅	16.980	n.a	[181]
BT-Py _{BuOH} COF	1669	2.36	10mgCOF, AA, Ni ₂ P	3.160	n.a	[188]
BT-Cz _{EtOH} COF	100	2.70	10mgCOF, AA, CoP	1.132	n.an	
			1 mg COF, AA, Pt	0.215	.a	
				11.285	4.88	[194]
				4.546	2.41	

Table 4
Acidic and alkaline mechanisms.

	Acid	Alkaline	Tafel slope
Volmer	* + H ⁺ + e ⁻ → H*	* + H ₂ O + e ⁻ → H* + OH ⁻	b ≈ 120 mV dec ⁻¹
Heyrovsky	H ⁺ + e ⁻ + H* → H ₂	H ₂ O + e ⁻ + H* → H ₂ + OH ⁻ + *	b ≈ 40 mV dec ⁻¹
Tafel	2H* → H ₂ + 2*	2H* → H ₂ + 2*	b ≈ 30 mV dec ⁻¹
Overall	2H ⁺ + 2e ⁻ → H ₂	2H ₂ O + 2e ⁻ → H ₂ + 2OH ⁻	

COF-based electrocatalysts can boost the HER under acidic conditions. Here, we outline recent developments of COF-tailored electrocatalysts that are used in the HER process because of current research. COF-tailored HER electrocatalysts are summarized in Table 4.

8.1.1. Metal-free COFs for electrocatalytic HER

The advantage of advanced electrocatalysts can be attributed to their reaction kinetics and overpotential values. With respect to HER activity, noble metal-based materials generally exhibit a lower overpotential than other transition metal-based materials; for example, platinum (Pt) supported on carbon is regarded as the most effective catalyst for HER those exhibits high electrocatalytic performance. Nevertheless, its high cost makes this process unviable [278]. Noteworthy efforts have been made in the past few decades toward identifying active transition metals such as Fe, Co, and Ni that can be used in non-noble metal-based systems [277,279,280]. The problem with these metals is that they are frequently leached out of the matrixes, thereby rendering the electrocatalytic system toxic. Metal-free electrocatalysts are a promising

solution to overcome the above challenge and facilitate an eco-friendly method of producing high-purity clean energy. Generally, an organic system that is electrochemically active exhibits properties such as a low band gap, functional groups with active properties, and electron conjugation with the electronic component. To explore metal-free electrocatalysts, appropriately modulating these features is challenging. Recent studies have reported on the use of metal-free COF in HER by Bhunia *et al.* [281] Through a solvothermal approach, they have developed a two-dimensional quasi-dielectric COF (SB-PORPy-COF) (Fig. 32a) by reacting TAP (5,10,15,20-tetrakis (4-aminophenyl)porphyrin) with TFFPy (1,3,6,8-tetrakis (4-formylphenyl) pyrene). Porphyrin and pyrene blocks are alternately occupied on the vertex positions of the 3D triclinic crystal of this metal-free COF electrocatalyst, leading to a large specific surface area (~869 m²/g) and superior stability. SB-PORPy-COF demonstrated HER activity in an acid condition with a significantly low onset overpotential of only 50 mV and Tafel Slope of 116 mV dec⁻¹, which is the lowest overpotential value reported for various COF (Fig. 32b and c). It was also shown that the prepared SB-PORPy-COF exhibited good high ability in acidic conditions, exhibiting virtually no activity loss in terms of onset potentials or current densities at different possibilities after a continuous 500 cycle test conducted under acidic conditions (Fig. 32d). An additional study demonstrated the use of Schiff base condensation to prepare metal-free COF with N-doped porphyrin units (PAM (5,10,15,20-tetra(4-aminophenyl)-21H,23H-porphyrin)) and Tp (triformyl phloroglucinol) for electrocatalytic HER that has an area of 654 m²g⁻¹ with a pore size of 1.6 Å⁰ (Fig. 33a and b). With an overpotential of only 250 mV at a proton reduction current density of 10 mA cm⁻² (Fig. 33c) and a Tafel slope of 106 mV dec⁻¹, the obtained porous TpPAM electrocatalyst

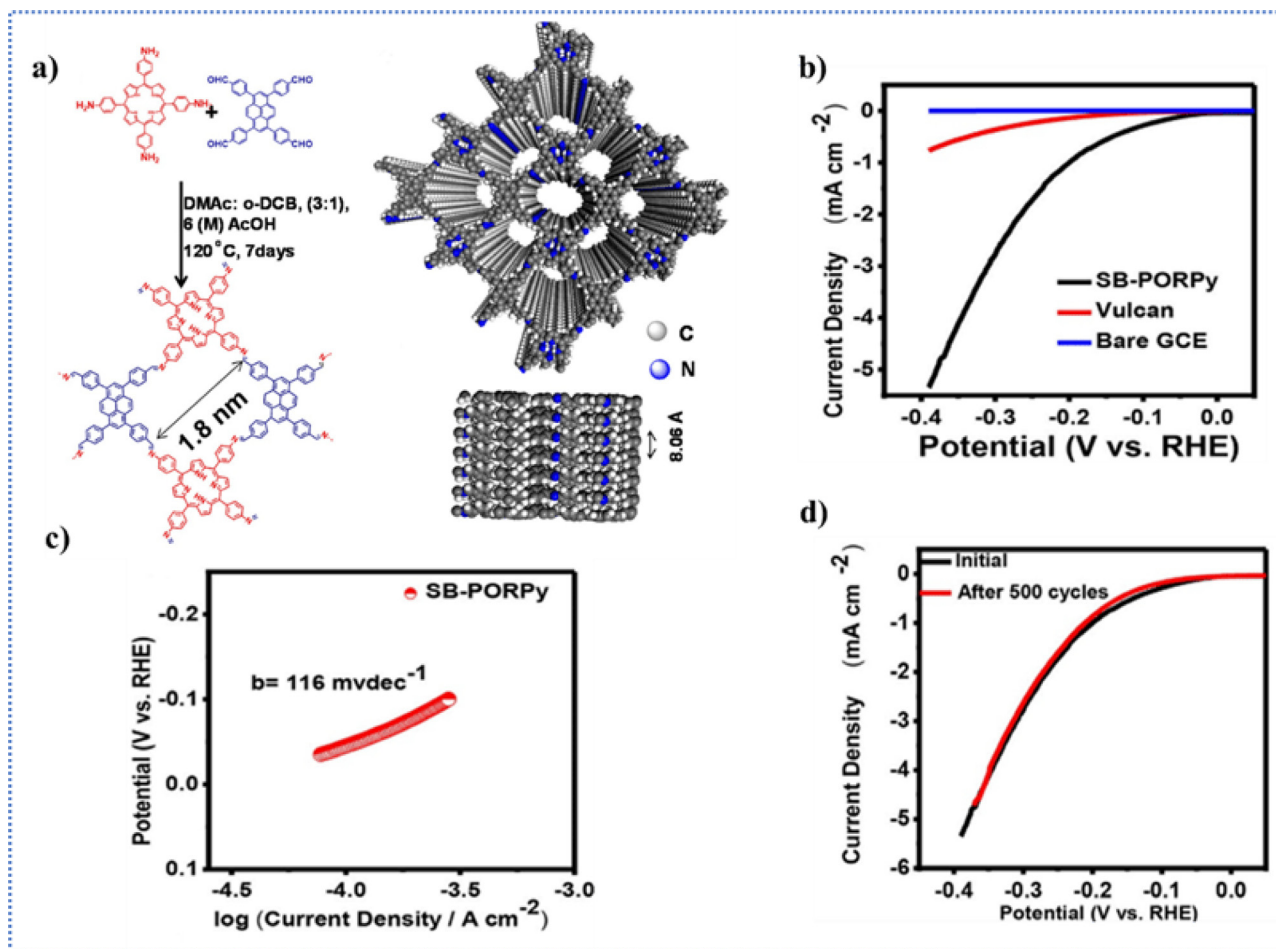


Fig. 32. a) Synthesis of 1,3,6,8-tetrakis(4-formylphenyl) pyrene (TFPPy), Synthetic scheme of the imine based COF (SB-PORPy), Top view, and side view of AA (eclipsed) stacking of SB-PORPy COF (gray, carbon; blue, nitrogen). b) Polarization curves for the hydrogen evolution reaction on bare GC (blue), Vulcan (red), and SB-PORPy-COF (black) electrodes. c) Corresponding Tafel plot of SB-PORPy-COF electrode. d) Stability of SB-PORPy-COF catalysts. Reproduced from Ref [281] with permission of the American Chemical Society.

demonstrated considerable HER activity. After a continuous 1000 cycles test, the TpPAM also exhibited outstanding HER long-term durability in operational conditions with a current density retention rate of 91 % (Fig. 33e). Furthermore, the lowest (ΔG^*) value (model C, Fig. 33f). HER activity was also correlated with the repeating structural unit (*meso*-tetra(4(benzylideneamino)phenyl)-porphyrin) of the TpPAM, as predicted by DFT-based theoretical calculations. According to Fig. 33e, the ΔG^* value of the repeating structural unit (0.08 eV) is slightly lower than that of the Pt electrocatalyst (0.09 eV), thus proving that metal free TpPAM has a higher electrocatalytic efficiency than other transition-metal HER catalysts [72]. The protonated porphyrin unit grabbed one electron and converted it into a π -cation radical. It has been revealed that the electrochemical study shows a chemically reversible process. Since protons can be reversibly reduced, H_2 is produced (Fig. 33h) [268]. Based on existing synthesis methods, thiophene-, bithiophene-, and triazine units were used to produce both metal-free COFs (TTT-DTDA COF and TTT-BTDA COF) [282] (Fig. 34a). These two COFs were synthesized by Fang et al [283] and renamed JLNU-301 and JLNU-302 for narrative purposes. The crystallinity and porosity of these materials were very high. A thiophene- A thiophene-based structure also has high conductivity and charge mobility, allowing the material to transfer electrons rapidly during the HER, improving its electrocatalytic activity. Thus, at a current density of 10 mA cm^{-2} , the overpotentials are

136 and 91 mV, respectively, with small Tafel slopes of 110.55 and $103.88 \text{ mV dec}^{-1}$ in alkaline media (Fig. 34b and c). JLNU-COFs showed long-term stability in an alkaline medium after 3000 CV cycles (Fig. 34e and f). JLNU-COFs efficiently implement HERs in solutions at all pH values. A density functional theory (DFT) calculation supports the experimental identification (Fig. 34d). Comparing the electrocatalytic performances of the obtained materials, particularly the HER performance under alkaline conditions, is superior to those reported previously for conjugated microporous polymers (CMPs) [284,285], COPs [268], MOFs [286], and all metal-free carbon fibers [281,287,288]. In Fig. 35a, C6-TRZ-TFP is synthesized by solvothermal polycondensation of 2-hydroxybenzene-1,3,5-tricarbaldehyde (TFP) and 4,4'-((1,3,5-triazine-2,4,6-triyl)tris[(1,1-biphenyl)-4-amine] [289]. The C6-TRZ-TFP exhibits considerable HER properties in electrochemical water splitting, with a very low overpotential of 200 mV at a current density of 10 mA cm^{-2} and a small Tafel slope of 82 mV dec^{-1} in 0.5 M aqueous H_2SO_4 (Fig. 35b and c). A density functional theory calculation indicates that electron-deficient carbon sites near nitrogen atoms are more effective toward HER than those near oxygen and nitrogen atoms (Fig. 35e and f). Tests of the durability of C6-TRZ-TFP COF were conducted using chronopotentiometry at a current density of 10 mA cm^{-2} . Over 50 h of continuous operation, the catalyst showed a very steady potentiometric curve with 94 % operational retention of potential [Fig. 35d].

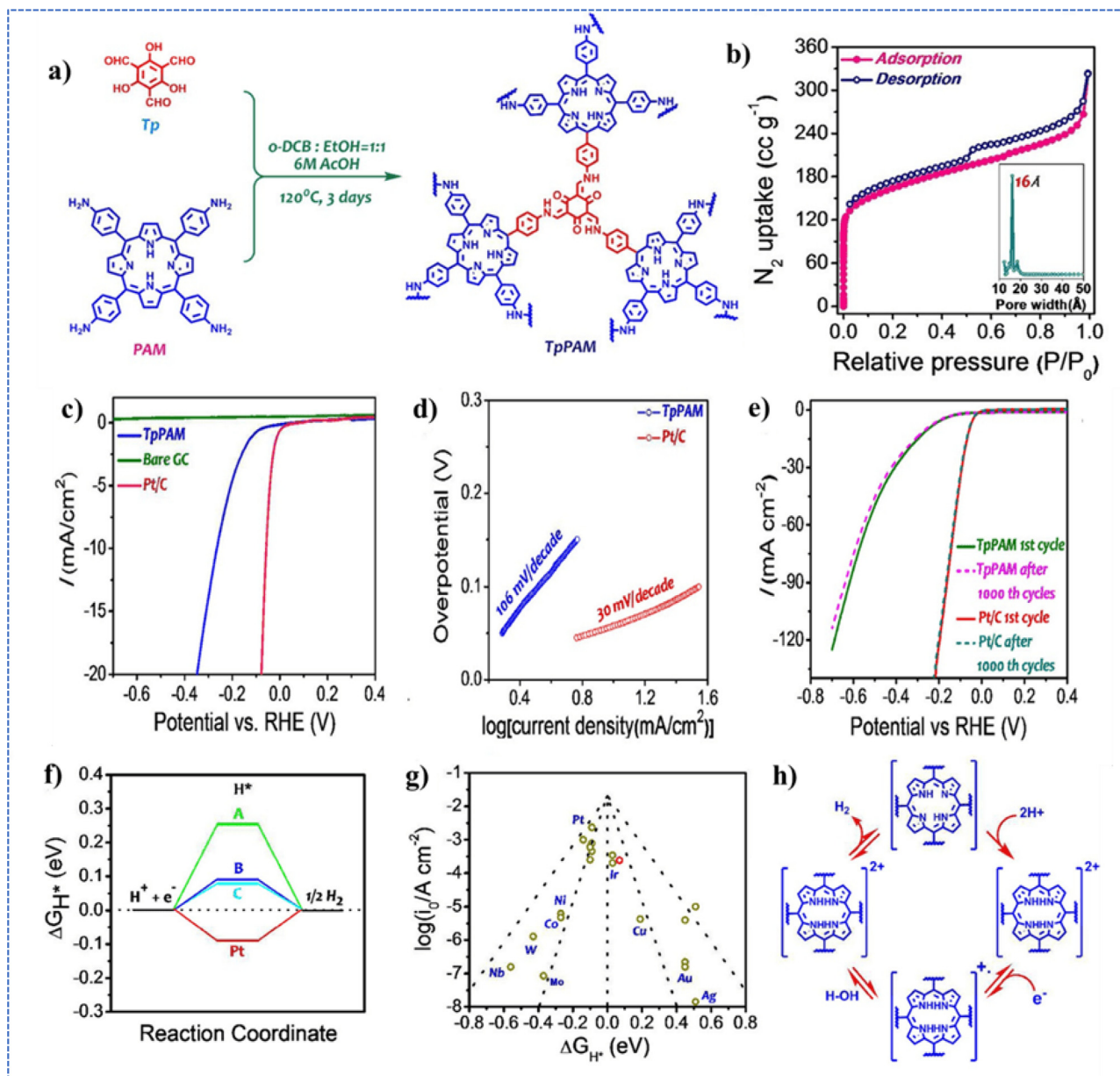


Fig. 33. a) Schematic diagram of the metal-free covalent organic polymer (TpPAM). b) N₂ adsorption-desorption isotherm with PSD (inset). c) LSV plots of TpPAM, Pt/C, and bare GC recorded at 1600 rpm in 0.5 M H₂SO₄. d) Tafel plots of TpPAM and Pt/C. e) LSV plots of TpPAM in its first and after 1000th cycles of test run. f) Calculated free-energy diagram of HER for metal-free porphyrin (model A), 5,10,15,20-tetra(4-aminophenyl)-porphyrin (model B), meso-tetra(4-(benzylideneamino)phenyl)-porphyrin (model C) and Pt at the equilibrium potential. g) Volcano plot of log i₀ vs ΔG_{H*} for model C (red circle) and transition-metal catalysts (dark yellow circle). h) HER mechanism (step 1): protonation of the porphyrin ring, (step 2): electron accumulation, (step 3): regeneration of the doubly charged porphyrin moiety, and (step 4): regeneration of the neutral porphyrin ring and H₂ evolution. Reproduced from Ref. [268] with permission of the American Chemical Society.

8.1.2. Metallic COFs for electrocatalytic HER

Due to their abundant redox states of metal centers, metallic COFs are more likely to be used as HER electrocatalysts than metal-free COFs. Porphyrin-based networks have been found to contain many metal atoms that enhance HER performance. In strong acidic media, Villagrán and co-workers reported electrocatalytic hydrogen generation using cobalt porphyrin-based COFs [290]. The porous channels and exposed metalloporphyrin active sites contribute to the high HER performance of the crystalline polymer (deposited on FTO glass slides using silver glue). Moreover, the improved electrocatalytic efficiency of the HER compared to the cobalt porphyrin monomer indicates that constructing an extended conjugated system can improve the electrocatalytic effi-

ciency and confirms that crystallinity and well-ordered channels within COFs contribute to the enhancement of electrocatalytic efficiency. According to Babu *et al.* [291], octahydroxy decorated metalloporphyrin and squaric acid were used as building blocks and metal-free catalysts for synthesizing 2D polymers linked by C—C bonds. The best HER performance was found in a bimetallic (Co and Ni) 2DP (2DP_{3A}), which showed a Tafel slope of 74.1 mV dec⁻¹ and a high FE of 97%. A further advantage of COFs is that they can be used as supports for the immobilization and stabilization of small nanoparticles with HER catalysts [292,293]. As cross-linkers, triazine (C₃N₃) units are used to synthesize covalent triazine frameworks (CTFs) [294–303]. In the study by Hu *et al.* [292], MoS₂ nanoparticles were in situ grown into the 1D channel

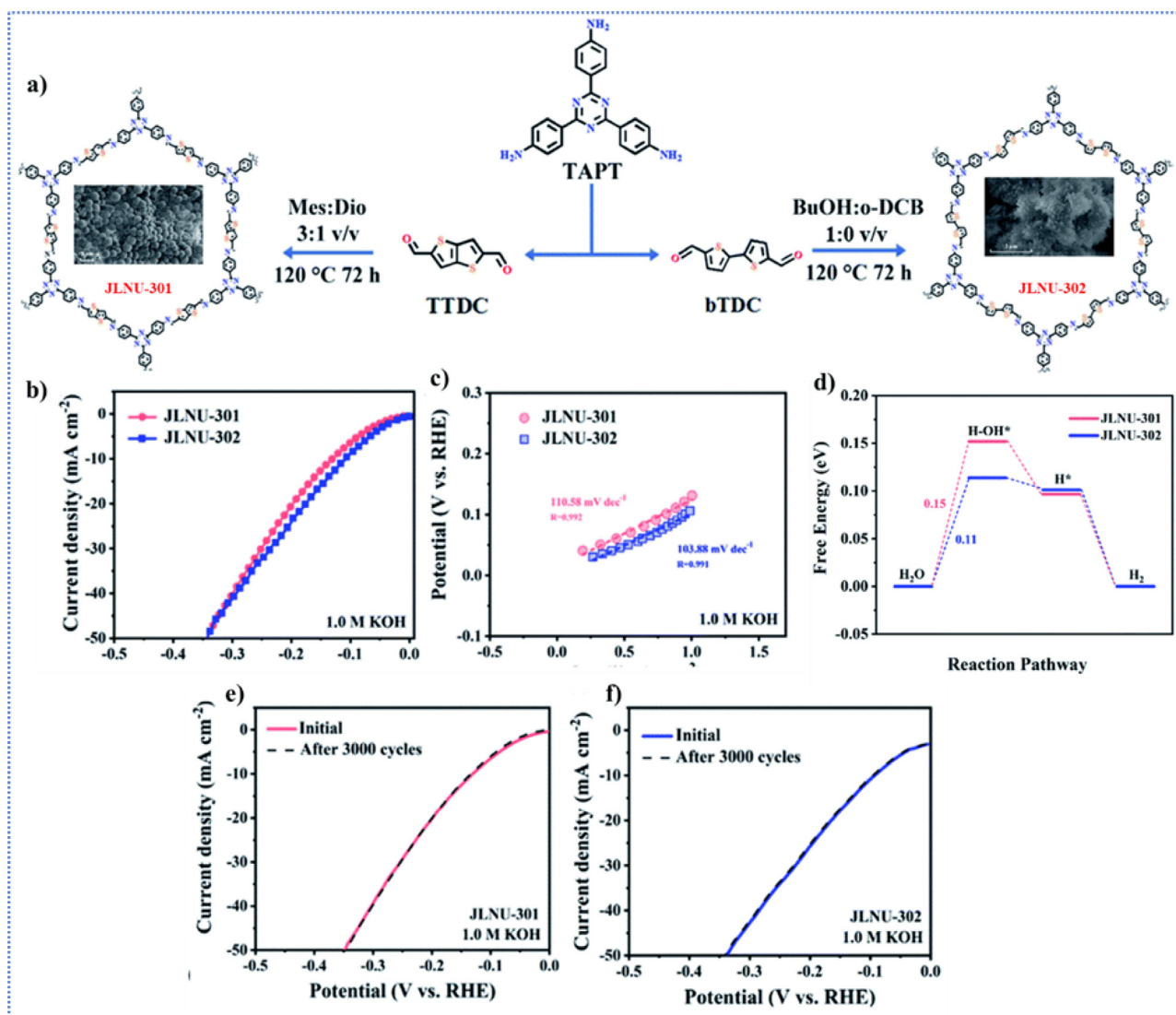


Fig. 34. a) Synthesis and structures of JLNU-301 and JLNU-302 and SEM image of JLNU-301 and JLNU-302. b) HER performance characterization in 1.0 M KOH: (a) polarization curves, (b) Tafel plots, (c) Nyquist plots, (d) chronopotentiometry plots for JLNU-COFs. (e) HER plots of JLNU-301 before and after 3000 cycles. (f) HER plots of JLNU-302 before and after 3000 cycles. c) Calculated free energy diagrams for JLNU-COFs. Reproduced from Ref. [283] with permission of the Royal Chemical Society.

arrays of CTFs (Fig. 36a). A study was conducted to determine the influence of the amount of MoS₂. It was demonstrated that CTF@MoS₂-5 (where 5 represents the mass ratio of CTFs)[thin space (1/6-em)]:[thin space (1/6-em)]MoS₂ exhibit catalytic kinetics with a voltage excess of 93 mV at 10 mA cm⁻² (Fig. 36b). As shown in Fig. 36c, the Tafel slope of 43 mV dec⁻¹, which is close to that of a benchmark catalyst (20 % Pt/C) and lower than that of CTFs or MoS₂ with different mass ratios. By stacking 2D in-plane porous layers, crystalline 1D channel arrays were suggested to enhance electron transmission, mass diffusion, and accessibility of MoS₂ active sites during H₂ evolution (Fig. 36). However, these COF-based catalysts, as well as those based on non-noble metals, and even metal-free catalysts, have lower electrocatalytic performances than Pt-based systems and many other non-noble metals HER systems. A significant bottleneck to achieving practical application for large-scale H₂ production is the poor conductivity and low stability of COFs. Consequently, the development of stable COFs should also be emphasized, along with new approaches to ensure intimate contact with conducting supports to improve the HER performance of COF-based electrocatalysts. The HER performance of most metallic-COFs has been demonstrated in Table 5 [268,281,283,291,298,300,302,303].

8.2. COFs for electrocatalytic (OER)

OER is the second half reaction in the water splitting procedure, including the four-electron transfer step, with slow kinetics and extreme overpotential; thus, it is the major bottleneck for the overall water splitting and sustainable hydrogen production. Table 6 shows the suggested pathways for intermediates that generate O₂ during the OER producer, including OH*, OOH*, and O* under the acidic and basic conditions [304]. As mentioned earlier, the binding energies for the intermediates seek strong correlation, especially for OOH* and OH*. The difficulty of the OER procedure arises from the bond breaking of hydroxyl group (O–H), subsequent bond making for oxygen molecule (O=O), and the loss of electrons from water molecules concerning the HER procedure (Table 6). As with HER, pointers such as overpotential, Tafel slope, efficiency, and Faradaic stability are commonly used to elucidate the electrocatalytic performance of a given OER catalyst, which are also crucial for understanding the OER mechanism. For instance, the most common method to control and evaluate the electrocatalytic performance of any electrocatalyst is the comparison of its overpotential at a current density equal to 10 mA cm⁻² with benchmark materials. The Tafel slope is another critical

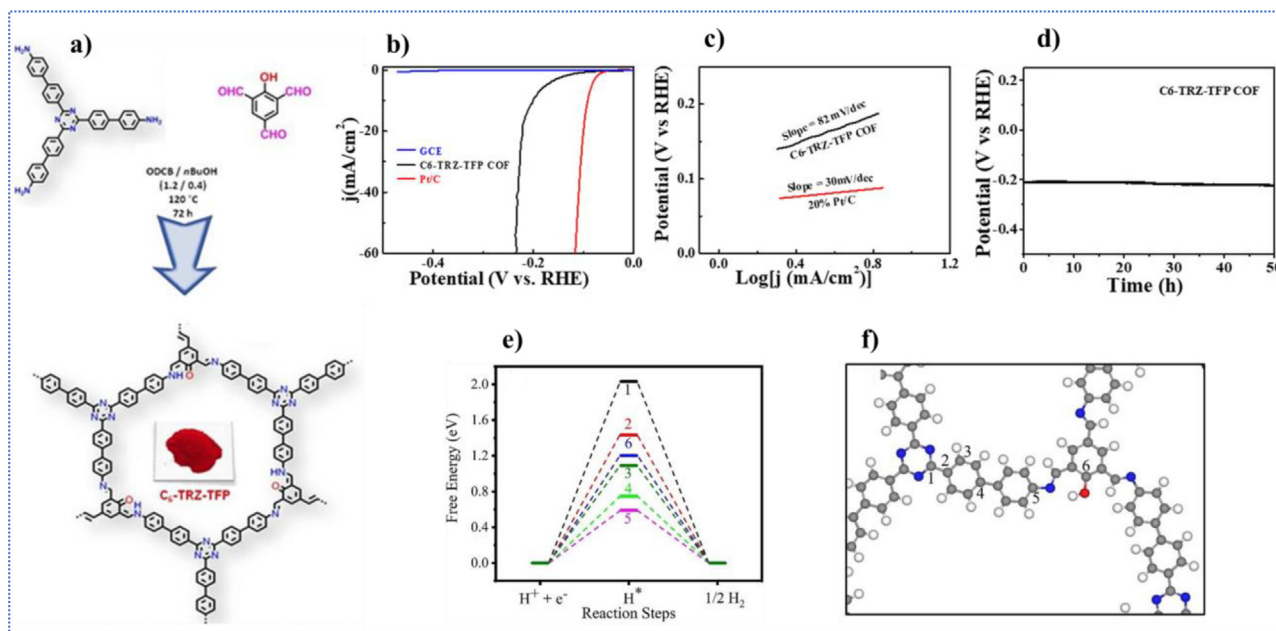


Fig. 35. a) Synthesis of C6-TRZ-TFP COF starting from 2-hydroxybenzene-1,3,5-tricarbaldehyde (TFP) and 4,4',4''-(1,3,5-triazine-2,4,6-triyl)tris[(1,1-biphenyl)-4-amine] (C6-TRZ-TRIAMINE). b) LSV polarization plot of the C6-TRZ-TFP COF, 20% Pt/C and blank GCE at a scan rate of 5 mV s^{-1} . c) Tafel plots of the C6-TRZ-TFP COF and 20% Pt/C. (c) Exchange current density plot of C6-TRZ-TFP COF. d) Chronopotentiometry measurement shows the stability of C6-TRZ-TFP COF. e) Free energy plots of HER on unique sites. f) Model structure showing the selected sites for H-atom adsorption. Gray, blue, red, and white spheres represent carbon, nitrogen, oxygen and hydrogen, respectively. Reproduced from Ref. [289] with permission of the John Wiley and Sons.

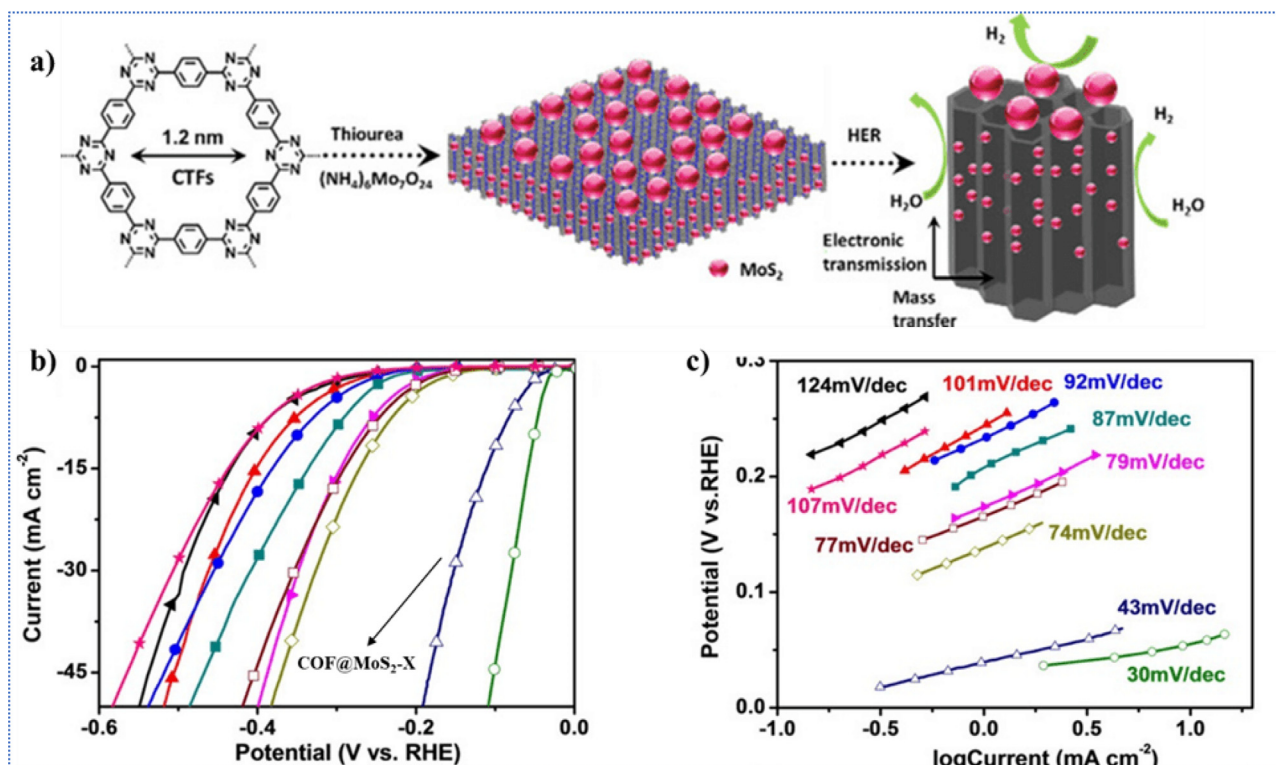


Fig. 36. a) The formation process of CTFs@MoS₂ and schematic structure of crystal 1D channel arrays derived from 2D in-plane porous layer stackings its electrocatalytic HER. b) LSV of CTFs@MoS₂ for HER catalysis in 0.5 M H₂SO₄, compared to those of other materials such as Pt/C (green), pure CTFs (black), MoS₂ (rose red) and CTF@MoS₂-X with different mass ratios. c) Tafel slope of all catalysts calculated from LSVs. Reproduced from Ref. [292] with permission of the Royal Chemical Society.

Table 5
Reported cofcs for electrocatalytic her.

Electrocatalysts	Electrolyte	$\eta@10 \text{ mA cm}^{-2}$ (mV)	Tafel slope (mV dec ⁻¹)	Stability	Ref.
SB-PORPy-COF	0.5 M H ₂ SO ₄	200@1 mA cm ⁻²	116	500 cycles	[281]
JLNU-301	1.0 M KOH	136	110.55	3000 cycles	[283]
JLNU-302	1.0 M KOH	91	103.88	3000 cycles	
C-Fe ₂ Co-COF	1.0 M KOH	330	100	-	[298]
TPPAM	0.5 M H ₂ SO ₄	250	106	5 h	[268]
Co-2DP(5)	1 M KOH	367@1 mA cm ⁻²	126	-	[299]
COP	1 M KOH	425	202	-	[300]
CoCOP		310	161	7000 s	
2DP1	0.1 M H ₂ SO ₄	314	156.1	12 h	[291]
2DP2		287	262.2	12 h	
2DP3A		105	74.1	12 h	
2DP1 + 2DP2		518	436.1	-	
FCoP@CNT	0.5 M H ₂ SO ₄	576@1 mA cm ⁻²	126	7 h	[302]
CoSAs/PTF-400	0.5 M H ₂ SO ₄	188	104	-	[303]
CoSAs/PTF-500		58	91	-	
CoSAs/PTF-600		94	50	10 h	

Table 6
Mechanisms of OER in acidic and alkaline mediums.

Half reaction	In acidic solution	In alkaline solution
Anode reaction	$2\text{O} \rightarrow \text{O}_2 + 4\text{H}^+ + 4\text{e}^-$	$4\text{OH}^- \rightarrow 2\text{O}_2 + 2\text{H}_2\text{O} + 4\text{e}^-$
Mechanisms	$* + \text{H}_2\text{O} \rightarrow \text{OH}^* + \text{H}^+ + \text{e}^-$ $\text{OH}^* \rightarrow \text{O}^* + \text{H}^+ + \text{e}^-$ $2\text{O}^* \rightarrow 2^* + \text{O}_2$	$* + \text{OH}^- \rightarrow \text{OH}^* + \text{e}^-$ $\text{OH}^* + \text{OH}^- \rightarrow \text{O}^* + \text{H}_2\text{O} + \text{e}^-$ $2\text{O}^* \rightarrow 2^* + \text{O}_2$
	$\text{O}^* + \text{H}_2\text{O} \rightarrow \text{OOH}^* + \text{H}^+ + \text{e}^-$ $\text{OOH}^* \rightarrow * + \text{O}_2 + \text{H}^+ + \text{e}^-$	$\text{O}^* + \text{OH}^- \rightarrow \text{OOH}^* + \text{e}^-$ $\text{OOH}^* + \text{OH}^- \rightarrow * + \text{O}_2 + \text{H}_2\text{O} + \text{e}^-$

Where * stands for an active site on the electrocatalyst surface.

parameter used to judge the activity of the OER process, which is defined as the relationship between the current density and overpotential (i.e., number of involved electrons in the electrocatalytic reaction). Predictably, a slighter Tafel slope is estimated to suggest decent electrocatalytic kinetics of an OER catalyst. As a result, any small change in the overpotential affords a quick increase in the current density value. Because OER operates at a high applied voltage (V), chemical stability is a crucial consideration when evaluating the degradation of OER catalysts. Some parameters are normally used to assess electrocatalyst stability, such as chemical composition, crystallinity, micro- and macro-scale morphology, and electrochemical performance. Noble metal oxides such as RuO₂ and IrO₂ are considered as the most satisfactory OER cata-

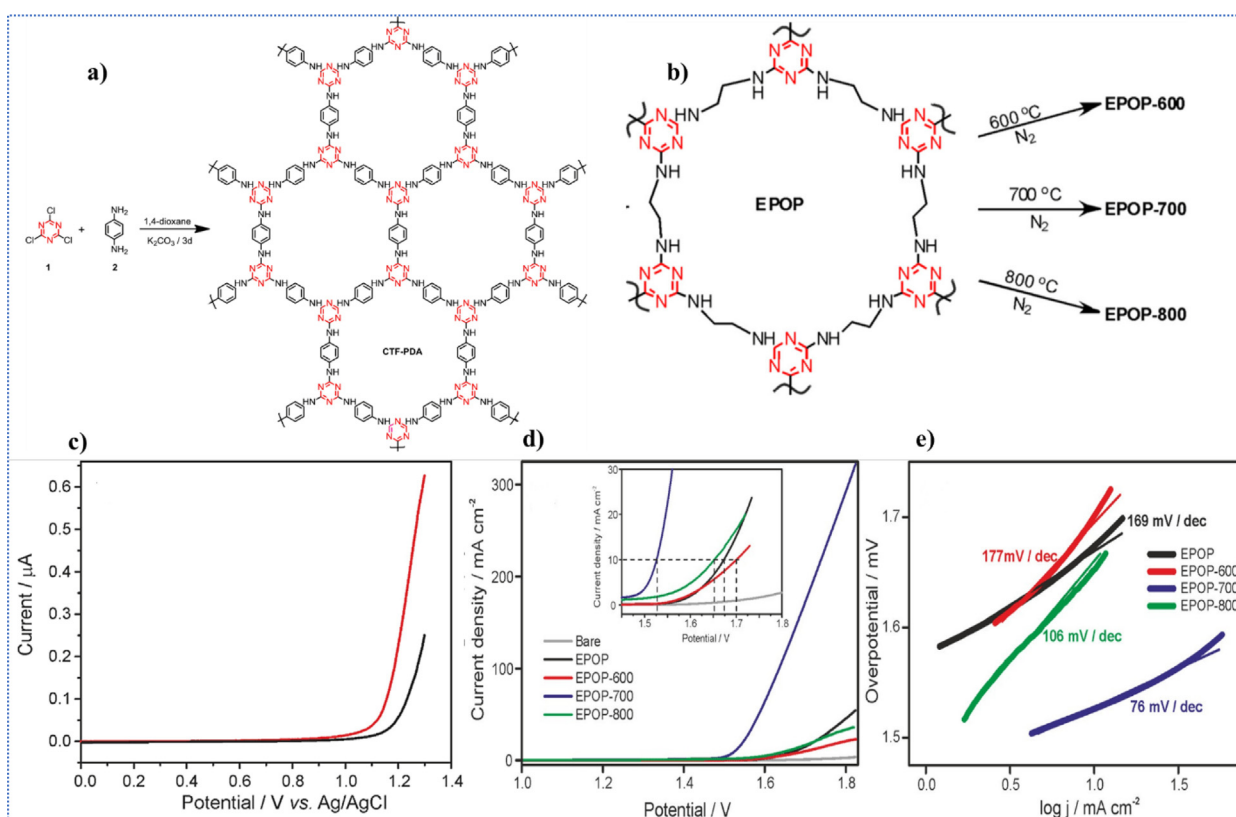


Fig. 37. a) Synthesis of PD-CTF, b) Synthesis of EPOP and Its Carbon Composites toward OER. (c) OER in 1 M KOH, red -PD-CTF/GC electrode, black- GC electrode, Electrochemical performance of EPOP and its carbon composites toward OER. (d) LSV; (e) Tafel plots in 0.1 M KOH solution at 2 mV/s. Reproduced from Ref. [312,313] with permission of the MDPI and American Chemical Society.

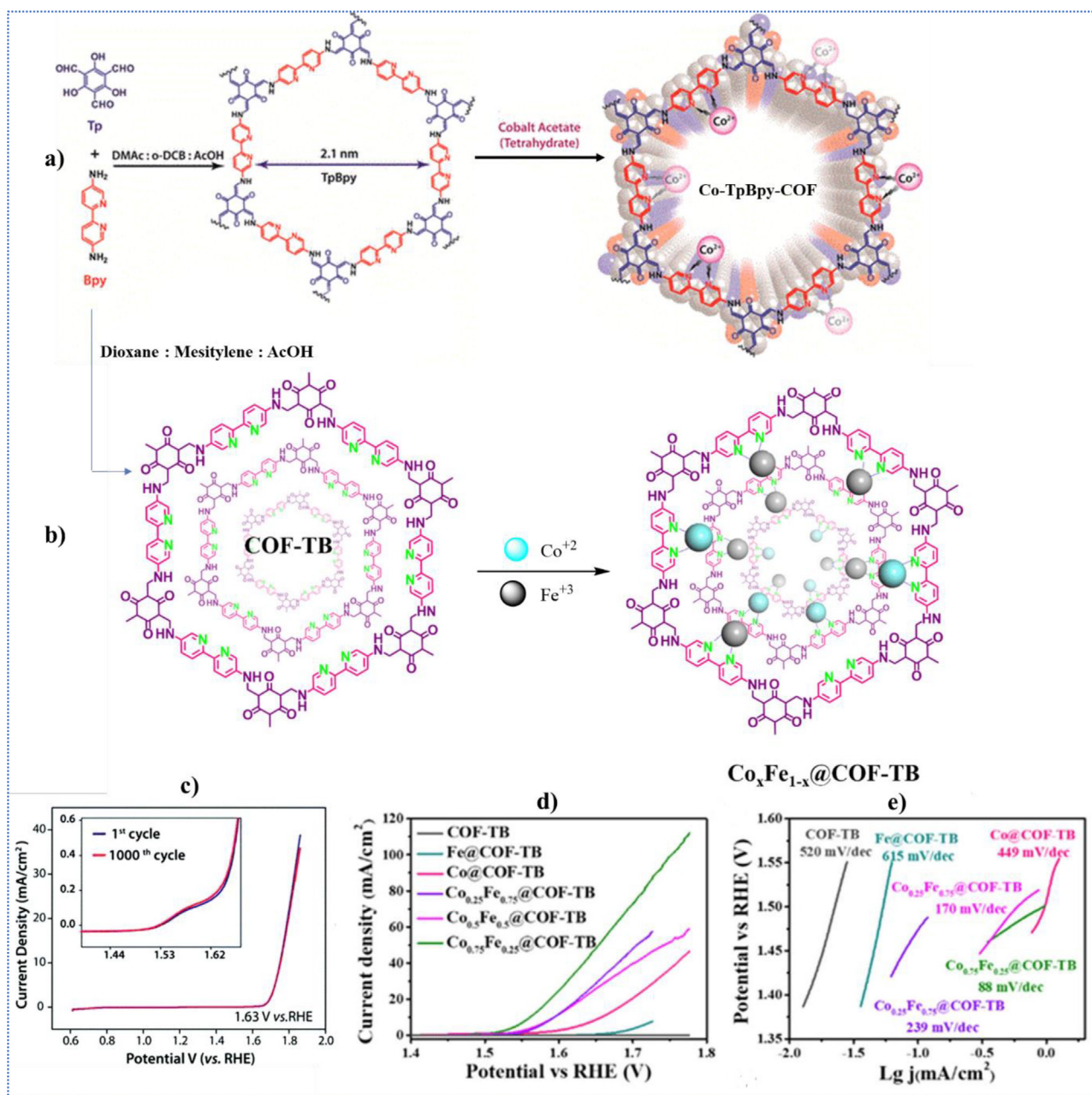


Fig. 38. (a) Synthesis of Co-TPBpy-COF, b) Synthesis of $\text{Co}_x\text{Fe}_{1-x}@COF-TB$; c) LSV profiles of Co-TPBpy before and after 1000 cycles from 0.6 V to 1.8 V in a phosphate buffer (pH 7.0). Inset: An enlarged view of the LSV profile. d) (a) LSV curves toward OER of COF-TB, $\text{Co}_x\text{Fe}_{1-x}@COF-TB$ ($x = 0, 0.25, 0.5, 0.75, 1$); (b) Tafel slopes of the prepared materials. Reproduced from Ref. [314,317] with permission American Chemical Society and MDPI.

lysts, despite limitations such as high cost and unavailability. So, enormous efforts have been taken to design and create low-cost alternative electrocatalysts, such as single-atom systems [305,306], transition metal oxides and their derivatives [307–309], and carbon-based materials [310,311].

8.2.1. Metal-free COFs for electrocatalytic (OER)

The electrocatalytic activity of metal-free COFs for the OER process is generally small; this may be attributed to the limited active site and lack of electrical conductivity. Kathiresan *et al.* [312] reported a type of covalent triazine framework (CTFs), which is based on 1,4-phenylenediamine (PD-CTF) via the reaction of cyanuric chloride and 1,4-phenylenediamine in a basic environment (Fig. 37a). The PD-CTF gives rise to low electrocatalytic performance with an onset potential of + 1108 mV (vs Ag/AgCl) for the

OER under alkaline conditions. The presence of triazine moiety causes electrocatalytic activity for this material (PD-CTF) because the N-doped sites are one of the most critical factors for any material to work as an electrocatalyst, as mentioned above. There are many trials to enhance the catalytic activity via the post-carbonization phenomenon to solve this dilemma for the metal-free COFs, mainly based on CTFs. In another study, the porous CTFs were prepared by the cyanuric chloride reaction with ethylene diamine and then carbonized at different temperatures, including 600, 700, and 800 °C, respectively (Fig. 37b) [313]. The carbonized porous-COF showed a significant increase in OER catalytic activity concerning the original COF. The results proved that the carbonized-COF at 700 °C, which was coated on carbon paper, demonstrated an onset potential of 1.527 V and an overpotential of 297 mV to achieve a 10 mA cm⁻² current density and low Tafel

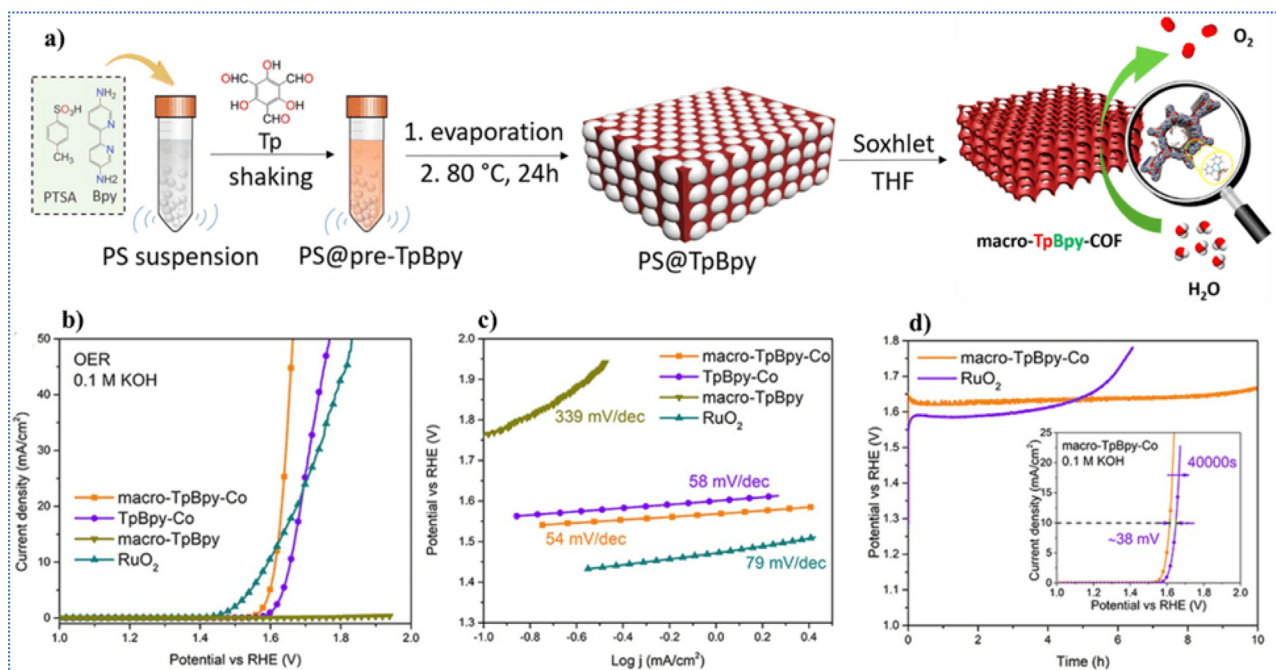


Fig. 39. a) Schematic representation of macro-TpBpy fabrication in the presence of PSs and its OER, b) a) OER polarization curves and (c) corresponding Tafel plots for macro-TpBpy, macro-TpBpy-Co, TpBpy-Co, and a commercial RuO₂ catalyst, d) Chronopotentiometry test of macro-TpBpy-Co and RuO₂ catalysts at a constant current density of 10 mA cm⁻². Inset: OER polarization plots of macro-TpBpy-Co before and after 40 000 s. Reproduced from Ref. [61] with permission American Chemical Society.

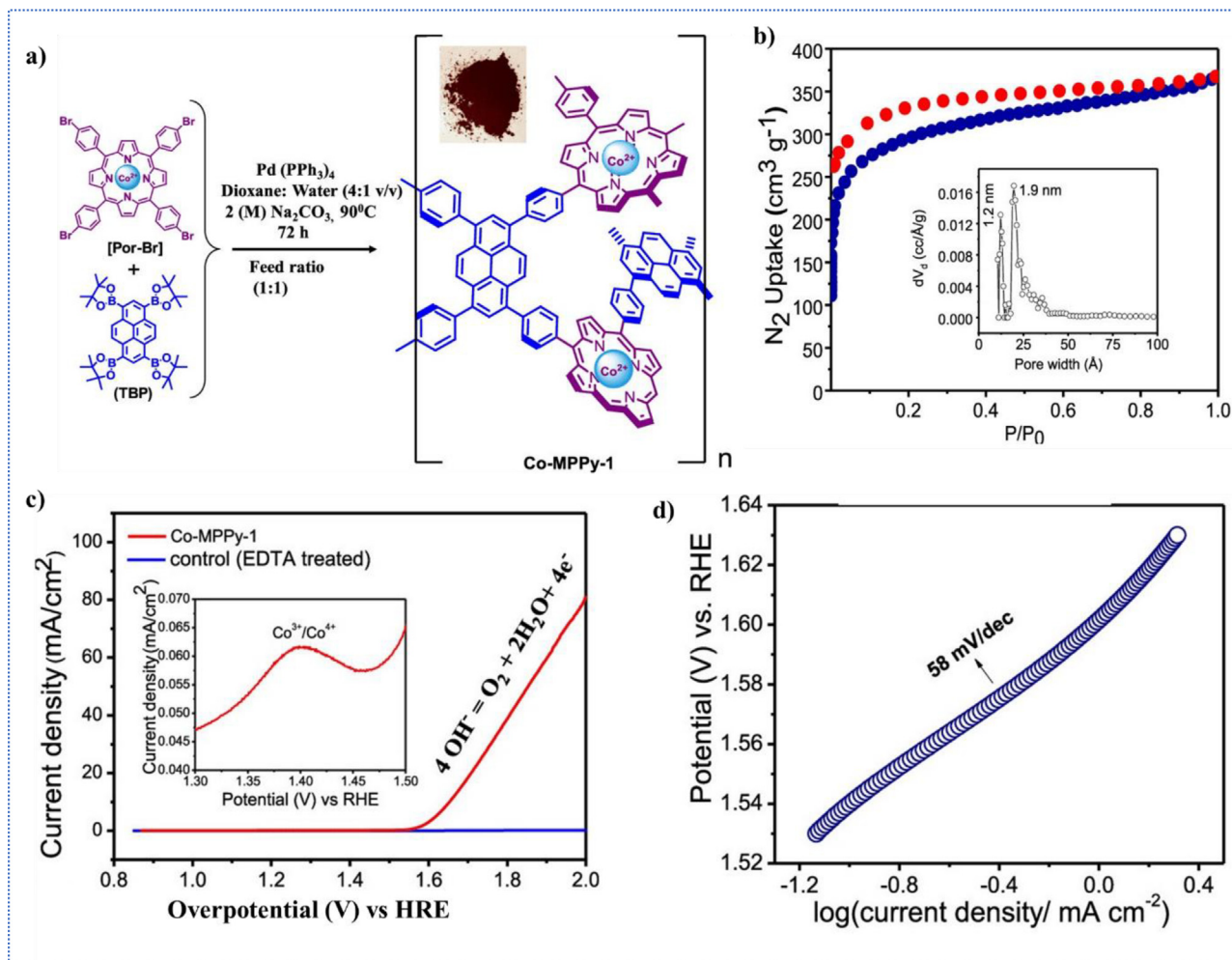


Fig. 40. a) Formation of Co-MPPy-1, b) N₂ adsorption/desorption isotherm and NLDFT pore size distribution (inset), c) LSV of Co-MPPy-1 (red line) and control catalyst (blue line) in 1 M NaOH solution at the scan rate of 2 mV/s. d) Tafel slope of Co-MPPy-1. Reproduced from Ref. [323] with permission American Chemical Society.

Table 7

Comparison of the reported OER catalytic performance of COFs and other catalysts.

Electrocatalysts	Electrolyte	η_{10} (mV)	Tafel slope (mV dec ⁻¹)	Refs
CoNP-PTCOF	0.1 M KOH	450	–	[333]
Ag/Ag ₂ O@MCOF(Co)	1.0 M KOH	260	48	[334]
COF-Ni(OH) ₂	0.1 M KOH	487	89.3	[335]
COF-Co(OH) ₂ 91.4	0.1 M KOH	402	91.4	[335]
2D-Co-MOF 74	1.0 M KOH	263	74	[336]
COF-TpDb-Tz-Co	1.0 M KOH	390	82	[337]
Co@COF-Pyr	1.0 M KOH	450	100	[338]
Co _{0.75} Fe _{0.25} @COF-TB	1.0 M KOH	331	88	[320]
Co _{0.5} V _{0.5} @COF-SO ₃	1.0 M KOH	318	–	[318]
Ni _{0.5} Fe _{0.5} @COF-SO ₃	1.0 M KOH	308	83	[339]
Co@N-C-800	1.0 M KOH	350	99	[340]
COF-366-Co@CNT	1.0 M KOH	358	62	[341]
C ₄ -SHz COF	1.0 M KOH	320	39	[342]
macro-TpBpy-Co	0.1 M KOH	380	54	[61]
Ni/Fe-COF@CNT ₉₀₀	0.1 M KOH	320	61	[343]
Co-MPPy-1	1.0 M NaOH	420	58	[323]
CoS ₂ -NiCo ₂ S ₄ /NSG	1.0 M KOH	272	62.8	[344]
Fe ₃ C-Co/NC	1.0 M KOH	340	–	[345]
FeCo(1:3)@SNC	1.0 M KOH	288	40	[325]

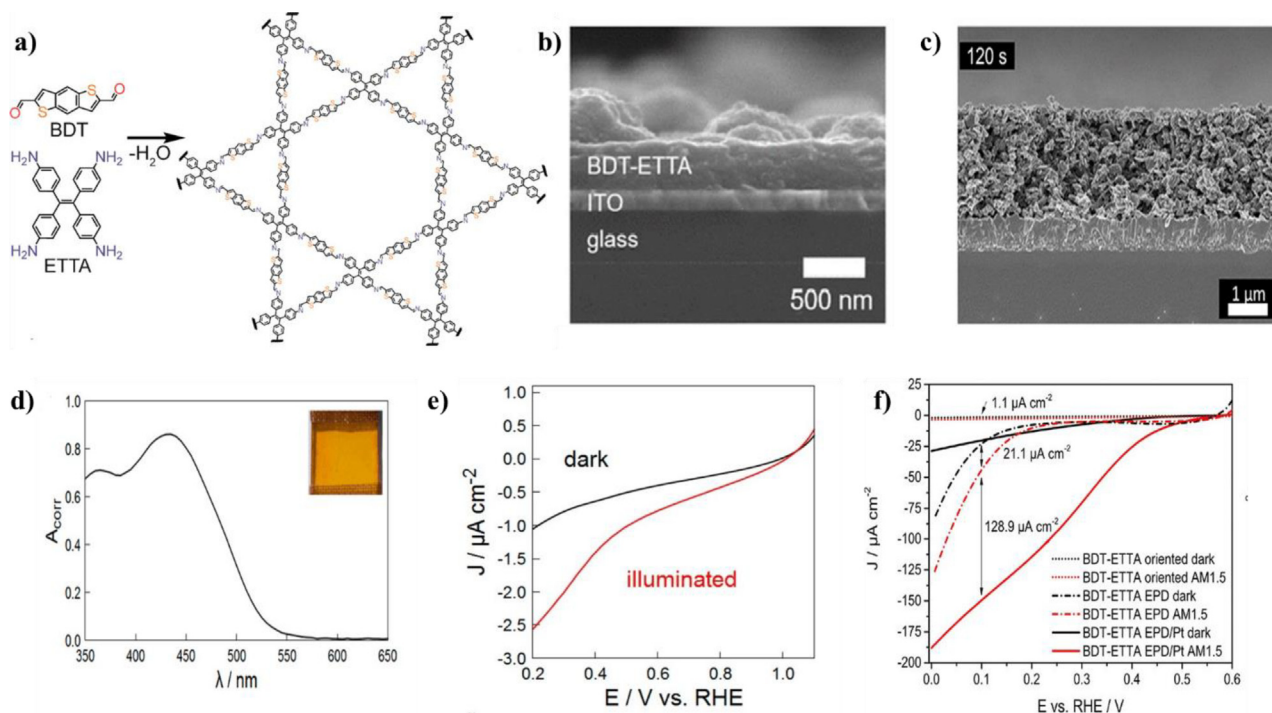


Fig. 41. a) Synthetic approach for the formation of a BDT-ETTA COF. b, c) SEM images (cross-section) of thick BDT-ETTA film grown on ITO substrates by oriented thin film and EPD methods, respectively. d) Absorbance spectrum of a BDT-ETTA thin film on ITO with a photograph of a representative sample masked with a PFTE adhesive tape (inset). e) Linear sweep voltammograms of BDT-ETTA films on ITO performed in the dark (black) and under AM 1.5 illumination through the substrate (red), f) PEC linear sweep voltammograms of electrodes coated with BDT-ETTA COF as a dense and oriented film, a 3 μm thick film prepared by EPD. Reproduced from Ref. [349,350] with permission American Chemical Society.

slope up to 76 mVdec⁻¹ (Fig. 37d and e). interestingly, the carbonized COF at a high current density of 300 mA cm⁻², showed a low overpotential of 580 mV; this opens the horizon to understand the improvement of some of the metal-based OER electrocatalysts.

8.2.2. Metallic COF for electrocatalytic (OER)

Covalent organic frameworks are considered attractive materials for many applications, including catalysis, sorption, separation, and sensing. As a result, this category provides an excellent platform for OER electrocatalysts because it possesses inherently well-designated frameworks as a good active site and can be

manipulated to the required criteria for the electrocatalyst application. All of these serve to advance a better consideration of the mechanism of this multielectron transfer reaction. Recently, many scientists and chemists mentioned the role of metal-complexation in the COFs structures based on bipyridine, porphyrin, and triazine structures to explain how the integration of metal atoms within the COFs network will enhance the OER electrocatalytic activity. These metalized COFs may be potential OER electrocatalysts by using the numerous readily available metal active sites on the exceptional surface areas and the mass-transfer routes offered by the pores. In 2016, Banerjee's group synthesized the Co-TpBpy-

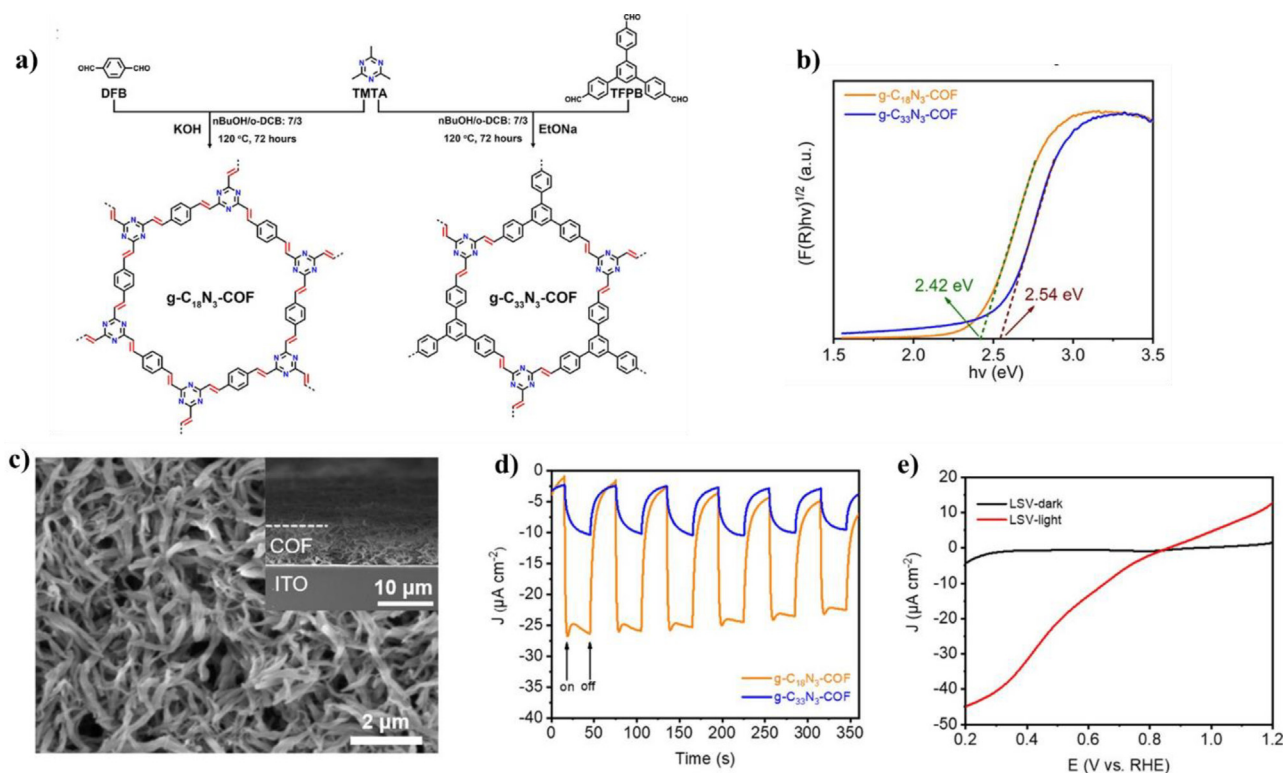


Fig. 42. a) Scheme of the synthesis of $g\text{-C}_{18}\text{N}_3\text{-COF}$ and $g\text{-C}_{33}\text{N}_3\text{-COF}$ by Knoevenagel condensation. b) Band gap determined from the Kubelka–Munk-transformed reflectance spectra. c) Top view: SEM micrograph of $g\text{-C}_{18}\text{N}_3\text{-COF}$ film, representing the surface morphology. The inset is a cross-section SEM micrograph, showing a uniform film thickness. d) Chopped photocurrent density vs time recorded on $g\text{-C}_{18}\text{N}_3\text{-COF}$ and $g\text{-C}_{33}\text{N}_3\text{-COF}$ film at 0.4 V vs RHE. e) Linear sweep voltammograms of $g\text{-C}_{18}\text{N}_3\text{-COF}$ film on ITO performed in the dark (black) and under visible light illumination (red). Reproduced from Ref. [351] with permission American Chemical Society.

COF by keto-enamine condensation between 1,3,5-triformylphloroglucinol (Tp) and 2,2'-bipyridine-5,5'-diamine (Bpy) and coordinated the resultant TpBpy-COF with cobalt ion leads to the abundant of cobalt-nitrogen (Co-N) active site with high surface area reached to $\sim 450 \text{ m}^2/\text{g}$, mimicking metal-bipyridine molecular structures [314–316] (Fig. 38a). The electrocatalytic measurements for this COF revealed that under neutral conditions, a good OER performance with an overpotential of $\sim 520 \text{ mV}$ at 10 mA cm^{-2} and good stability with a similar polarization curve retention after 1000 scans from 0.6 V to 1.8 V (vs RHE) were obtained (Fig. 38c). Ongoing the importance of bipyridyl moiety for the OER process, Chen and his coworkers fabricated a series of bimetallic-based COF ($\text{Co}_x\text{Fe}_{1-x}\text{@COF-TB}$) with different ratios [317]. The pristine COF was prepared by the solvothermal method for the previous monomer (Tp and Bpy) but in different solvents, including the mesitylene and dioxane, as depicted in Fig. 38a and b. As well the COF-TB modified by Fe and Co individually but the bimetallic-COF, especially, $\text{Co}_{0.75}\text{Fe}_{0.25}\text{@COF-TB}$ gave a high performance for OER. This COF showed a lower overpotential of 331 mV at 10 mA cm^{-2} in a 1 M KOH solution and excellent stability with a Tafel slope equal to 88 mVdec^{-1} compared to the other materials (Fig. 38d and e). Interestingly, Gao et al. [318] reported an effective cation-exchange strategy to develop flexible and robust Co/V-incorporated bimetallic COF with optimized formula $\text{Co}_{0.5}\text{V}_{0.5}\text{@COF-SO}_3$ to present a good overpotential reached to 300 mV cm^{-2} and high stability. Integrating the strong electronic effect of the bimetallic system with COFs networks such as Co/V-COF and Co/Fe-COF helped improve OER electrocatalytic activity. Any electrocatalytic process requires mass transfer for electrolyte molecules, ions, gas molecules, etc. On the one hand, COF micro- or tiny mesopores enhance a surface area, but they might be too small to guarantee unobstructed mass transfer across the pore sys-

tem. The injection of extra mesopores or macropores into COFs to design hierarchical porosities is thought to be an effective technique to promote mass movement *via* COFs. Polystyrene spheres (PSs) were used as a hard template to create COFs with hierarchical pore architectures [61] (Fig. 39a). The advantage of increased macroporosity was exhibited using macro/microporous Co-coordinated bipyridine-COFs (macro-TpBpy-Co) as OER catalysts. Macro-TpBpy, TpBpy-Co, and commercialized RuO_2 electrocatalytic activities were examined using the identical mass loading of 0.25 mg/cm^2 (geometrical area). In contrast to macro-TpBpy, TpBpy-Co, and some other reported Co-cation-based catalysts, macro-TpBpy-Co only needs an overpotential of 380 mV to the reversible hydrogen electrode (RHE) to produce an anodic current density of 10 mA cm^{-2} (Fig. 39b). Both macro-TpBpy-Co and TpBpy-Co had a lower linear slope in the comparable Tafel slope of 54 mV/dec and 58 mV/dec, respectively than macro-TpBpy (339 mV/dec) and RuO_2 (79 mV/dec), implying better reaction kinetics in the OER operation (Fig. 39c). It worth mentioning, the chronopotentiometry test was established at current density 10 mA cm^{-2} to show the excellent stability for macro-TpBpy-Co after OER procedure which reached to 10 h in alkaline media (0.1 M KOH) without any notable difference respect with the original one (Fig. 39d). One of the first substances to be examined for noble metal-free OER was metal porphyrins because of their four-coordinated (metal-N₄) [291,319,320]. The porphyrin structure, integrating high- and low-valent metal ions (Co^{2+} , Ni^{2+} , Fe^{2+} , etc.), was explicitly made for oxidizing and reducing catalytic cycles [321,322]. As a result, Porphyrin-integrated COFs have been developed as an OER electrocatalyst. The Suzuki C–C cross-coupled reaction's production of a new Co(II) Por-/pyrene-based conjugated microporous polymer (Co-MPPy-1) demonstrated by Bhattacharya [323] (Fig. 40a). The obtained Co-MPPy-1 exhibited a significant

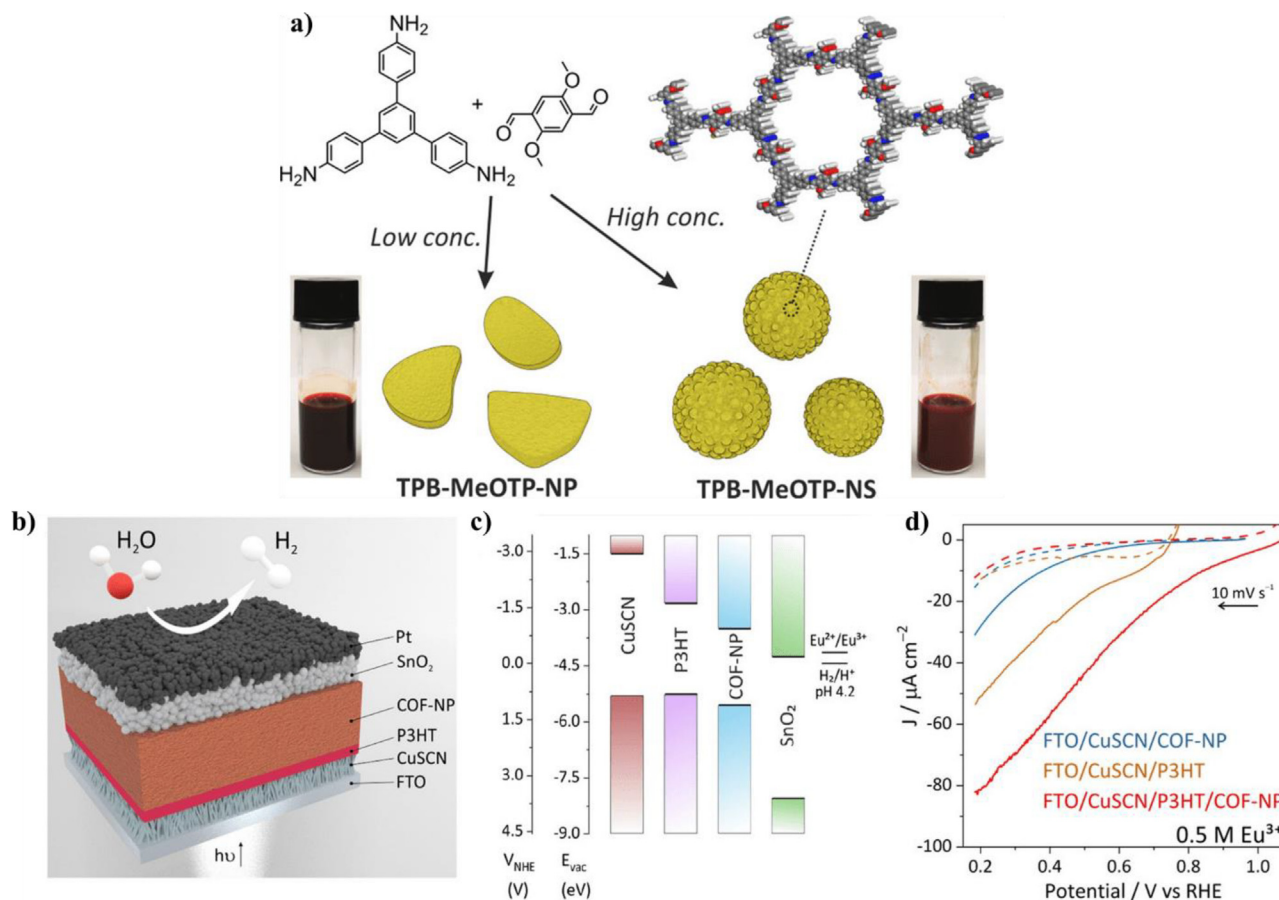


Fig. 43. a) Schematic illustration of the synthesis of TPB-MeOTP nanoplates (TPB-MeOTP-NP) and nanospheres (TPB-MeOTP-NS). Structural representation of TPB-MeOTP COF and photographs of the TPB-MeOTP-NP and TPB-MeOTP-NS colloids with a concentration of 4.5 mg mL^{-1} in acetonitrile. b) Schematic of the optimized hydrogen evolution COF photocathode layer arrangement. (c) Energy levels of the components in the photocathode vs vacuum and normal hydrogen electrode (NHE), including CuSCN, P3HT, TPB-MeOTP, and SnO₂. The energy levels of SnO₂ and H₂/H⁺ were adapted at pH 4.2 given their Nernstian behavior. d) LSV of TPB-MeOTP-NP, P₃H_T, and P₃H_T/TPB-MeOTP-NP photocathodes in 0.5 M Eu³⁺ aqueous electrolytes. Reproduced from Ref. [352] with permission American Chemical Society.

Brunauer-Emmett-Teller surface area of $501 \text{ m}^2/\text{g}$, as shown by the N₂ volumetric adsorption/desorption measurement (Fig. 40b). With a Tafel slope value of 58 mVdec^{-1} and a low overpotential of 420 mV at 10 mA cm^2 , Co-MPPy-1 demonstrated good electrocatalytic activity towards OER (Fig. 40c). The Co(II) Por- (donor) and pyrene (acceptor) electronic interaction and faster intramolecular charge transfer was demonstrated by the DFT calculation for Co-MPPy-1 [323]. A metallophthalocyanine-based COF (CoCMP) gives rise to a small onset potential of 1.57 V and a low Tafel slope of 87 mV dec^{-1} as a promising OER electrocatalyst. The long-term durability of CoCMP was investigated using chronoamperometry and 1000 cycles of LSV, and the findings revealed that CoCMP preserved a consistent catalytic performance without the leaching of Co(II) ions [324]. Mo and his co-workers [325] synthesized a bimetallic-integrated triazine-COF (FeCo(1:3)@SNC) and examined for OER process, with low overpotential ($\eta_{10} = 288 \text{ mV}$) and Tafel slope (40 mV dec^{-1}) in alkaline media. Moreover, the phenolic-linked 2D COF-C₄N showed a good OER process with low overpotential of 349 mV at current density of 10 mA cm^{-2} and Tafel slope (64 mV dec^{-1}) [326].

8.3. COFs for electrocatalytic overall water splitting

The oxygen evolution reaction (OER) and the hydrogen evolution reaction (HER) have attracted much attention due to their utmost importance for clean and renewable energy applications

[327–331]. It is thus highly desirable to develop new cost-effective OER/HER electrocatalysts with ideal activity, stability, and selectivity [327–331]. Two feasible strategies can be employed to achieve the goal: (1) using cheaper and earth-abundant metals; (2) reducing the loading number of precious metals to maximize their utilization efficiency. As emerging versatile nanomaterials, covalent-organic frameworks (COFs) can serve as OER/HER electrocatalysts, but their potential remains underexplored mainly thus far. In 2020, a bifunctional Co(II) Por-based covalent organic polymer (CoCOP) was prepared by a Schiff base reaction and showed excellent electrocatalytic activities both in HER and OER [242]. The resultant CoCOP achieved low overpotentials for both HER ($310 \text{ mV}@10 \text{ mA cm}^{-2}$) and OER ($350 \text{ mV}@10 \text{ mA cm}^{-2}$) in 1 M KOH . The excellent HER&OER performances for CoCOP could be attributed to the large surface area and the synergistic effect between Co(II) Por- moieties and the C=N bonds. Compared to Por-based COFs for electrocatalytic OER, the research on Pc-based COF is rarely reported. Ji et al. [332] described the COF-366-Co as a first-principles calculations to investigate the electrocatalytic performances of fifteen two-dimensional (2D) M-COFs (M = Sc-Zn, Ru, Rh, Pd, Ag, Ir) containing various metalloporphyrin active centers. The results reveal that all the M-COFs bear fully exposed, atomically dispersed, thermodynamically and electrochemically stable metal sites, as required by the ideal single-atom catalysts. According to the thermodynamic calculations, the Co-COF and Ir-COF are perfect OER catalysts with rather low theoretical overpotentials (η_{OER} :

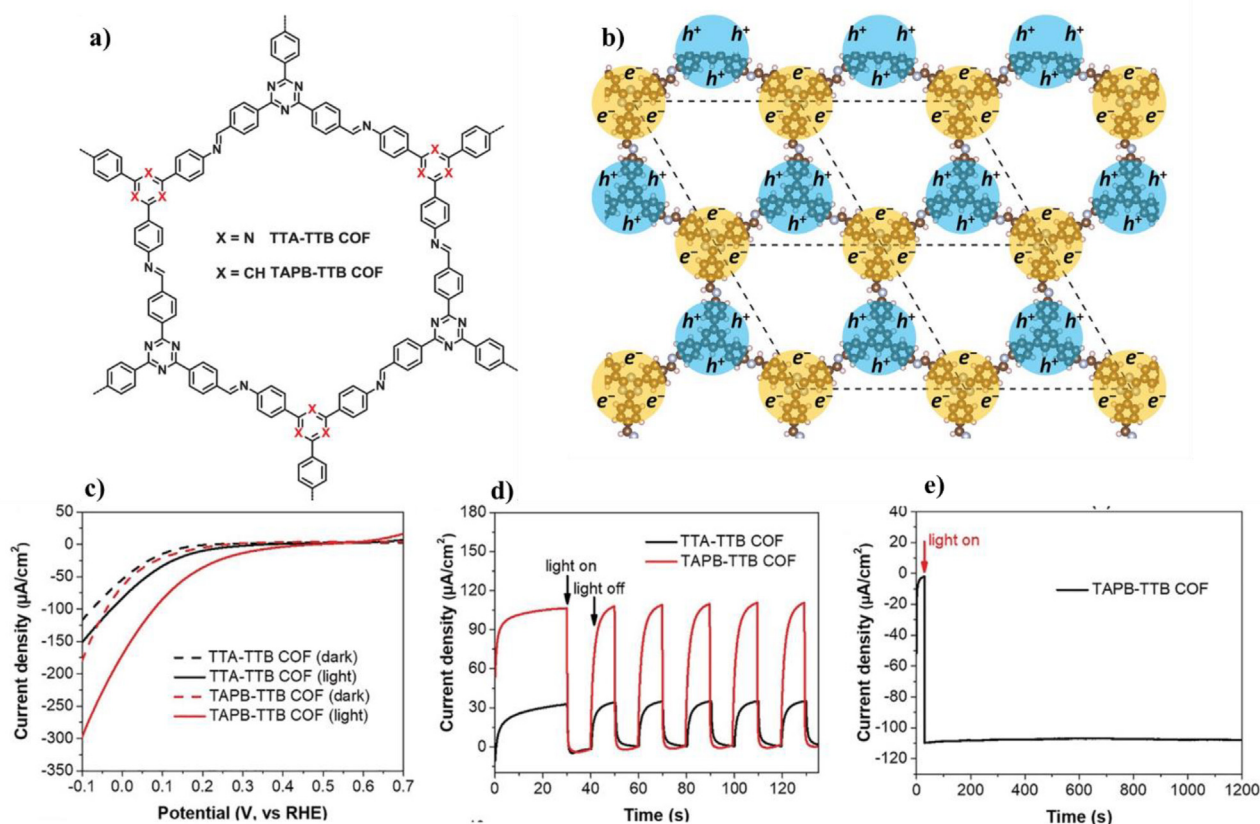


Fig. 44. a) Formation of TTA-TTB and TAPB-TTB-COFs based on imine linkage, b) Schematic illustration of the effective separation between excited e^- and h^+ for TAPB-TTB COF, c) (LSV) curves of TTA-TTB COF (black curve) and TAPB-TTB COF photoelectrodes (red curve), respectively, in $0.2\text{ M Na}_2\text{SO}_4$ aqueous solution (pH = 7) with and without visible light (> 420 nm); d) Photocurrent of COFs at 0 V versus RHE upon on/off visible light irradiation, e) The current-time (i-t) curves for TAPB-TTB COF photoanode under visible light irradiation (> 420 nm). Reproduced from Ref. [353] with permission the John Wiley and Sons.

0.38 and 0.34 V). The Mn-COF, Fe-COF, and Rh-COF are also promising for the OER (η_{OER} : 0.62, 0.57 and 0.51 V). Their excellent performances stem from the suitable metal d bands, which cause optimal bindings for all the key intermediate species along the reaction pathway. The current work not only finds several 2D-COFs as promising electrocatalysts, but also elucidates their exact structure-activity relationship, which is useful for the rational design of more single-atom catalysts. Table 7 presents the comparison of the reported OER catalytic performance of COFs and other catalysts [333–345].

8.4. COFs for photoelectrochemical water splitting

A new technique has been developed combining photocatalysis and electrolysis, called photoelectrochemical phenomena. Hydrogen can be produced cleanly and sustainably through photoelectrochemical water splitting (PEC) under visible light irradiation. In both the HER and OER processes, the electrons are transferred between different electrodes as in electrolysis, but a source of energy is obtained from sunlight, as in photocatalysis. Hydrogen and oxygen are produced by incident sunlight on the semiconductor surfaces of both half cells, and the products are directly separated and stored. Compared to the other approaches mentioned above, the design of this system is anticipated to result in reduced product cross-contamination, minimal energy losses and fabrication costs, and reduced manufacturing time [246]. Photoelectrolysis for large-scale hydrogen production is currently hindered by low yields (below 5 % solar-to-hydrogen efficiency), which means that additional research is needed to make this tech-

nology economically feasible, both on materials and mechanistic understanding. It is important to note that each technology should be studied and optimized separately to fulfill the specific needs of a specific application. In an ideal scenario, semiconductor surfaces would exhibit catalytic activity, which would otherwise require a cocatalyst. A 1.5–2.4 eV bandgap can be postulated for the optimal bandgap for electron transfer processes at the solid-electrolyte interface if the kinetic overpotentials are considered. Based on the Shockley-Queisser limit, experimental and theoretical studies predicted that a single optimal absorber would yield 12.6 mA cm^{-2} of maximum photocurrent density (with a 2.23 eV optical band gap and a 1.0 V assumed loss per photon) and that incident photons would convert 15 % into hydrogen at their maximum efficiency [25,346–352]. The greatest solar-to-hydrogen efficiency of tandem cells with a photoanode and a photocathode is 29.7 %. For optical band gaps of 1.6 and 0.95 eV for top and bottom cell electrodes, respectively. PEC water splitting could be applied to industrial applications if such efficiency and long-term stability can be achieved. A photoelectrochemical approach was used by Bein and his colleagues [349] to study the first COF utilized for water splitting in 2017. As a light-absorbing material, this COF was synthesized by Schiff-base condensation of four coordinate knots (1,1',2,2'-tetra-p-aminophenylethylene, ETTA) and two coordinate linkers (benzo[1,2-*b*:4,5-*b'*]dithiophene-2,6-dicarboxaldehyde (BDT)) (Fig. 41a), grown as an oriented film on transparent, conducting substrates [350]. Based on the results of the analysis, ETTA-BDT-COF is suitable for PCE applications, including efficient light harvesting, stable positioning, and suitable band positions

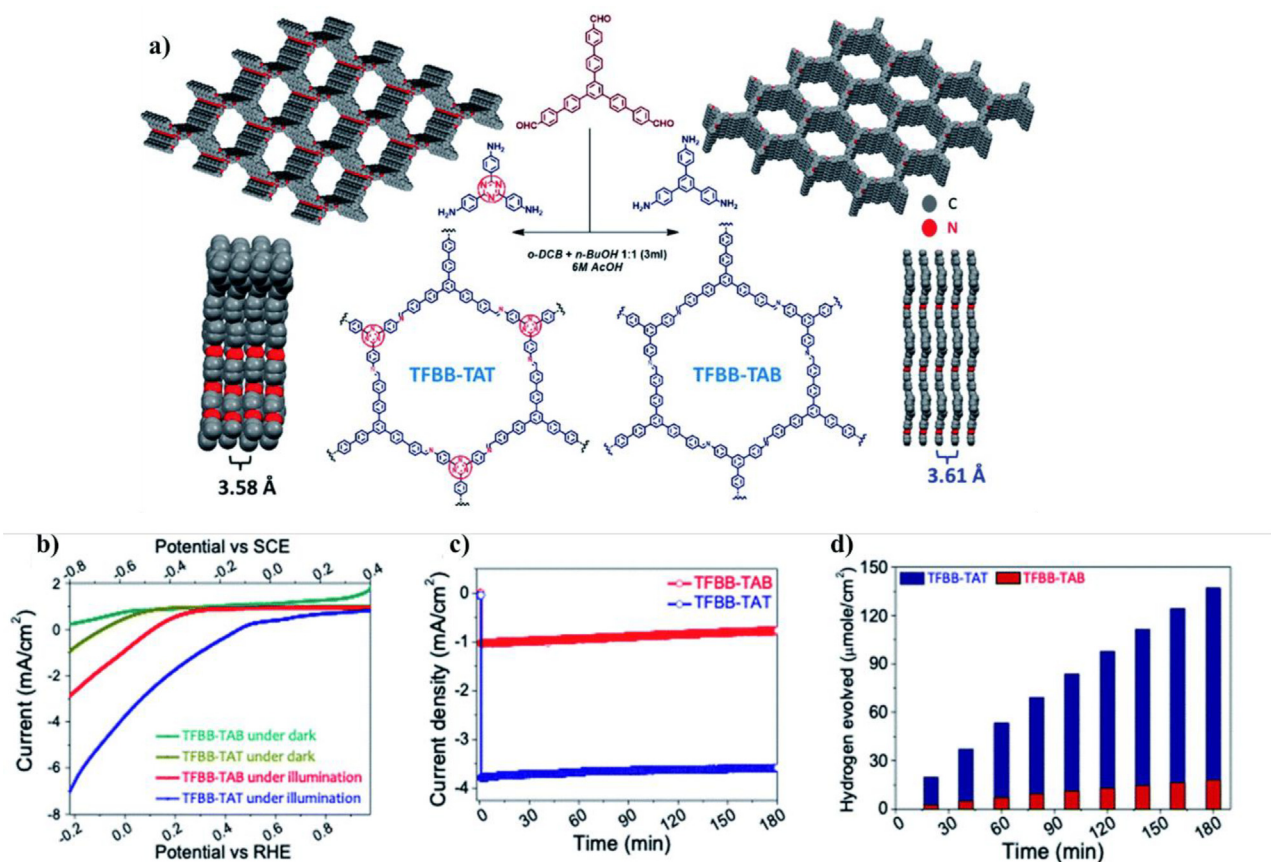


Fig. 45. a) Formation of TFBB-TAT and TFBB-TAB COFs, b) Polarization plots of the developed photocathodes under the dark and illumination, c) long term photostability of COF based photocathodes, d) PEC hydrogen production profile of the developed photocathodes Reproduced from Ref. [354] with permission Royal Chemical Society.

(Fig. 41d). PECs can generate HERs at 1.0 V vs reversible hydrogen electrodes (RHE), with currents as high as $1.5 \mu\text{A cm}^{-2}$ at 0.2 V vs RHE. A thicker (500 nm) film with a less homogeneous orientation showed a higher current density at 0.3 V than RHE, indicating a potential improvement in PEC performance of COF films (Fig. 41e). Electrophoretic deposition (EPD) was used recently to deposit ETTA-DBT-COF on FTO substrates to increase their activity by altering the coating method and layer thickness. It was found that the pristine BDT-ETTA COF film exhibited a photocurrent onset at 0.25 V vs RHE and a high photocurrent density ($21.1 \mu\text{A cm}^{-2}$) at 0.1 V vs RHE, a value 19 times higher than the earlier value for oriented thin BDT-ETTA-COF films [349] (Fig. 41f). Using the Knoevenagel condensation approach, Shice *et al.* [351] synthesized two new 2D covalent organic frameworks (COFs) together with unsubstituted carbon-carbon double bonds by activating the methyl carbons of a 2,4,6-trimethyl-1,3,5-triazine monomer. It has been demonstrated that this method is generalizable by forming two COFs from linear or trigonal aldehydes, termed $g\text{-C}_{18}\text{N}_3\text{-COF}$ and $g\text{-C}_{33}\text{N}_3\text{-COF}$, respectively (Fig. 42a). It is revealed that their honeycomb-like porous structures are stacked vertically and have a large surface area. It is important to note that both above mentioned COFs exhibit semiconducting properties, including the ability to harvest visible light with a suitable band gap, charge separation ability, and photocatalytic activity, which are effective for a good performance of photoelectrochemical processes (Fig. 42b). They enable assembling into microfibrillar morphologies (Fig. 42c), allowing for the fabrication of thin films in micrometer thickness without additives (Fig. 42c). Fig. 42d shows that, at 0.3 V vs RHE, the cathodic photocurrent of $g\text{-C}_{18}\text{N}_3\text{-COF}$ was $25 \mu\text{A cm}^{-2}$, about three times greater than that of $g\text{-C}_{33}\text{N}_3\text{-COF}$ ($8 \mu\text{A cm}^{-2}$), indicating that the separation of charge carriers

in $g\text{-C}_{18}\text{N}_3\text{-COF}$ is more efficient. At 0.2 V versus RHE, the $g\text{-C}_{18}\text{N}_3\text{-COF}$ film demonstrated a photocurrent of up to $45 \mu\text{A cm}^{-2}$ and rapid interfacial charge transfer (Fig. 42e). Yao *et al.* [352] describe the creation and use of colloidal COF nanoplates as photocathodes for solar hydrogen evolution. COF nanoparticles exhibit shape anisotropic growth, which can be attributed to a preference for growth in the direction of interlayer stacking, by analyzing their structure, morphology, nucleation behavior, and growth kinetics. The TPB-MeOTP-NP colloidal COF nanoplates show excellent colloidal stability for 10 months. Examining the growth mechanism of terephthalaldehyde linkers suggests that methoxy functionalization and self-assembly play an important role in forming nanoplate particles. MeOTP's self-assembly properties in acetonitrile are shown by PFG NMR analysis, enabling a template-induced crystallization of TPB-MeOTP and high-yield colloid formation (Fig. 43a). TPB-MeOTP-NP yields a highly homogeneous, thick, and smooth nanofilm compared to TPB-MeOTP-NS. As a result of illumination, photocathodic currents flow through photoelectrodes made from TPB-MeOTP colloids and are used to reduce Eu^{3+} in PEC. The V_{on} of COF photocathodes was shifted from + 0.59 V to + 1.03 V RHE by introducing CuSCN nanowires as HTL and a P3HT/TPB-MeOTP-NP heterojunction to suppress charge carrier recombination (Fig. 43d). The J_{ph} at + 0.7 V RHE can also reach $21 \mu\text{A cm}^{-2}$ with excellent stability over 30 min continuous illumination. The COF photocathode was optimized to produce an exceptionally positive V_{on} of + 1.06 V RHE for PEC hydrogen evolution when combined with a SnO_2 electron-collecting layer and a Pt HER catalyst layer (Fig. 43b). Furthermore, J_{ph} remained stable for 2 h, among the best results of classical semiconductor photocathodes. Because only a limited number of semiconductor materials with $V_{\text{on}} > +1\text{V RHE}$ have been

created so far, our results point to COFs being a promising candidate for use as a new generation of polymeric semiconductors for photoelectrodes. We are gaining a better understanding of how to prepare high-quality nanofilms and design photoelectrodes in this report, thus allowing us to use COFs in next-generation semiconductor devices by revealing the subtleties of photoelectrode preparation and the interplay between individual components. In Fig. 44a, two covalent organic frameworks (COFs) incorporating 2,4,6-triphenyl-1,3,5-triazine have been demonstrated to be excellent photocathodes to produce hydrogen. A significant increase in visible-light photocurrent of TAPB-TTB COF at zero voltage versus a reversible hydrogen electrode (RHE) at 0 V is obtained by adding 2,4,6-triphenylbenzene to create donor/acceptor pairs within COF by inserting 2,4,6-triphenylbenzene to properly create donor/acceptor pairs within COF. There is no need for organic sacrificial agents and metal cocatalysts (>420 nm) (Fig. 44b and c). Based on a durability test (Fig. 44e), TAPB-TTB COF maintained its photocurrent for >1200 s. By combining intramolecular donors and acceptors, the narrowed bandgap enhances photocurrent density. It can be seen in (Fig. 44b) that TAPB-TTB COF exhibits distinct distributions of excited electrons and holes, resulting in more efficient electron-hole separation and dissociation. Due to the smaller bandgap and stronger donor-acceptor interaction, TAPB-TTB COF has a much better photoelectrochemical performance. A high-efficiency organic photoelectrode for water splitting was developed using crystalline donor-acceptor COFs in this study [353]. 2-D TFBB-TAT and TFBB-TAB COFs were prepared by using condensation between 1,3,5-tris(4-formylbiphenyl)benzene (TFBB), 2,4,6-tris(4-aminophenyl)-1,3,5-triazine (TAT) and 2,4,6-tris(4-aminophenyl)benzene (TAB) yields crystalline, respectively (Fig. 45a). The covalent organic framework (COF), which shows promise as an ideal photo absorber due to the combination of efficient light harvesting sites with a suitable band gap and catalytic sites for the HER was described. The TFBB-TAT containing photocathode delivers a current density of 4.32 mA cm^{-2} , which was found to be much superior to that of the TFBB-TAB based counterpart. The higher cathodic current density achieved with the TFBB-TAT photocathode reflects its potential for water reduction under visible light illumination. The prepared triazine containing TFBB-TAT COF shows better photoelectrochemical (PEC) water splitting and chemical stability compared to the non-triazine based TFBB-TAB COF (Fig. 45b and c) [354]. The designed photocathode shows considerable retention of photocurrent density after 180 min of operation under visible light illumination (Fig. 45c). The TFBB-TAT based photocathode offers a hydrogen production capacity of $137 \mu\text{mol cm}^{-2}$ after 180 min of PEC operation. Moreover, the hydrogen production capacity of the TFBB-TAT electrode is shown to be 7.6 times higher than that of the TFBB-TAB electrode (Fig. 45d). It was found that condensation of 1,3,5-tris(4-formylbiphenyl)benzene (TFBB), 2,4,6-tris(4-aminophenyl)-1,3,5-triazine (TAT) and 2,4,6-tris(4-aminophenyl)-benzene (TAB) yielded crystalline COFs, TFBB-TAT and TFBB-TAB, respectively (Fig. 45a). Due to the combination of efficient light-harvesting sites, a suitable band gap, and catalytic sites for HER, the covalent organic framework (COF) appears promising as an ideal photo-absorbing material. It was found that the photocathode containing TFBB-TAT delivers a much higher current density than its TFBB-TAB-based counterpart, which delivers $3.47 \mu\text{A cm}^{-2}$. Under visible light illumination, TFBB-TAT photocathodes can achieve greater cathodic current density. In comparison with the non-triazine-based TFBB-TAB COF, the triazine-containing TFBB-TAT COF shows better photoelectrochemical (PEC) water splitting and chemical stability (Fig. 45c). Despite 180 min of exposure to visible light, the designed photocathode retains considerable photocurrent density. TFBB-TAT-based photocathodes can produce 137 mol of hydrogen per square meter after 180 min of PEC operation. A further differ-

ence between the TFBB-TAT electrode and the TFBB-TAB electrode appears to be that the TFBB-TAT electrode produces hydrogen at a rate seven times greater than that of the TFBB-TAB electrode (Fig. 45d) [354].

9. Conclusion

In this review, we overview and summarize the five hydrogen production routes by using MOFs/COFs and the derived catalysts. As for hydrogen production by using Metal-organic frameworks (MOFs) and MOF-derived catalysts, they are divided into two routes in this review: (1) the steam reforming reaction, and (2) the dry reforming reaction. When it comes to MOF materials with overwhelming catalytic activity in reforming reactions compared to conventional catalysts, though an unprecedented advancement has been accomplished over decades, we have to admit that there are still some limitations we need to overcome for future works. Regarding the obstacles that we are facing to recycling catalysts in the future, thermal and chemical stability problems of MOF materials hamper the development of large-scale catalytic utilization. Although we have already witnessed the progress of MOF materials by modifying them with several treatments (i.e., the introduction of other supports, the addition of promoters, pyrolysis, and the calcination process), there is still room for improvement for researchers to explore. First of all, a mature and stable synthesis method for future scale-up manufacturing must be researched in order to meet commercial requests. Moreover, the deep investigations on the morphological and characteristic transformation of MOF materials during the heat treatments should be analyzed to get a further look at MOF-derived materials. Lastly, although many experts dedicated themselves to hydrogen production research, few works published non-thermal reactions for MOF catalysis, namely the plasma-assisted reaction we introduced before. This review also exhibits a prospective research direction in the hydrogen production by using MOF-based catalysts by using non-thermal processes. Since Yaghi and co-workers discovered COFs in 2005, various COFs have been designed and synthesized, targeting versatile applications. COFs' well-defined structure, porosity, and surface area can benefit energy conversion and storage applications. COFs have several advantages over other typical materials. At first, it is very structurally controlled compared to carbon- and graphene-based materials. A material with defined chemical structures, tuneable pore sizes, and structures and low densities can be prepared by selecting appropriate building blocks and linkage motifs. Enhanced pseudocapacitive performance in supercapacitors or reversible processes rechargeable batteries can be achieved through metal-coordinating moieties in COFs. Furthermore, 100 % covalent connections may enable enhanced charge transport compared to MOFs, which is often problematic. In addition to providing a comprehensive understanding of the underlying photochemical and/or electrochemical reactions, COFs offer an excellent opportunity to study optimal systems of active sites. COF-based photocatalysts and/or electrocatalysts can be designed using various building blocks and molecular designs with precise, controllable active sites. It is possible to gain new insight into structure-function relationships in the photo and/or electrochemical devices using advanced in situ/in operando characterization techniques and computational tools, which can be applied more effectively to crystalline materials than to amorphous or ill-defined materials.

CRedit authorship contribution statement

Wei-Ting Chung: Conceptualization, Data curation, Writing – original draft. **Islam M.A. Mekheimer:** Conceptualization, Data

curation, Writing – original draft. **Mohamed Gamal Mohamed:** Conceptualization, Data curation, Supervision, Writing – original draft. **Ahmed M. Elewa:** Data curation, Writing – original draft. **Ahmed F.M. EL-Mahdy:** Conceptualization, Data curation, Investigation. **Ho-Hsiu Chou:** Supervision. **Shiao-Wei Kuo:** Supervision. **Kevin C.-W. Wu:** Supervision.

Data availability

The authors do not have permission to share data.

Declaration of Competing Interest

The authors declare that they have no known competing financial interests or personal relationships that could have appeared to influence the work reported in this paper.

Acknowledgement

The authors are thankful to the National Science and Technology Council (NSTC), Taiwan (111-2124-M-002-021; 111-2628-E-002-008; 111-2628-E-007-009-; 111-2221-E-007 -004-; 111-2622-8-007-011-) for the funding support. Also, financial support by the Center of Atomic Initiative for New Materials, National Taiwan University, from the Featured Areas Research Center Program within the framework of the Higher Education Sprout Project by the Ministry of Education in Taiwan (111L900801), is acknowledged.

References

- H. Xue, H. Gong, Y. Yamauchi, T. Sasaki, R. Ma, Photo-enhanced rechargeable high-energy-density metal batteries for solar energy conversion and storage, *Nano Res. Energy*, (1) (2022) e9120007. [10.26599/NRE.2022.9120007](https://doi.org/10.26599/NRE.2022.9120007).
- X. Xu, Z. Shao, S.P. Jiang, High-Entropy Materials for Water Electrolysis, *Energy Technol.* 10 (2022) 2200573, <https://doi.org/10.1002/ente.202200573>.
- H. Sun, X. Xu, H. Kim, W.C. Jung, W. Zhou, Z. Shao, Electrochemical Water Splitting: Bridging the Gaps between Fundamental Research and Industrial Applications, *Energy Environ. Mater.* (2022), <https://doi.org/10.1002/eeem.12441>.
- F. Abdelghafar, X. Xu, S.P. Jiang, Z. Shao, Designing single-atom catalysts toward improved alkaline hydrogen evolution reaction, *Mater. Rep. Energy* 2 (2022), <https://doi.org/10.1016/j.matre.2022.100144>.
- X. Xu, Y. Pan, Y. Zhong, R. Ran, Z. Shao, Ruddlesden-Popper perovskites in electrocatalysis, *Mater. Horiz.* 7 (2020) 2519–2565, <https://doi.org/10.1039/D0MH00477D>.
- W. Wang, M. Xu, X. Xu, W. Zhou, Z. Shao, Perovskite Oxide Based Electrodes for High-Performance Photoelectrochemical Water Splitting, *Angew. Chem. Int. Ed.*, (59) (2020) 2519–152. [10.1002/anie.201900292](https://doi.org/10.1002/anie.201900292).
- Y. Li, M. Karimi, Y.-N. Gong, N. Dai, V. Safarifard, H.-L. Jiang, Integration of metal-organic frameworks and covalent organic frameworks: Design, synthesis, and applications, *Matter* 4 (2021) 2230–2265, <https://doi.org/10.1016/j.matt.2021.03.022>.
- H. Wang, H. Wang, Z. Wang, L. Tang, G. Zeng, P. Xu, M. Chen, T. Xiong, C. Zhou, X. Li, D. Huang, Y. Zhu, Z. Wang, J. Tang, Covalent organic framework photocatalysts: structures and applications, *Chem. Soc. Rev.* 49 (2020) 4135–4165, <https://doi.org/10.1039/D0CS00278J>.
- Y. Shi, A.F. Yang, C.S. Cao, B. Zhao, Applications of MOFs: Recent advances in photocatalytic hydrogen production from water, *Coord. Chem. Rev.* 390 (2019) 50–75, <https://doi.org/10.1016/j.ccr.2019.03.012>.
- G.B. Wang, S. Li, C.X. Yan, F.C. Zhu, Q.Q. Lin, K.H. Xie, Y. Geng, Y.B. Dong, Covalent organic frameworks: emerging high-performance platforms for efficient photocatalytic applications, *J. Mater. Chem. A* 8 (2020) 6957–6983, <https://doi.org/10.1039/D0TA00556H>.
- X. Xu, H. Sun, S.P. Jiang, Z. Shao, Modulating metal-organic frameworks for catalyzing acidic oxygen evolution for proton exchange membrane water electrolysis, *SusMat* 1 (2021) 460–481, <https://doi.org/10.1002/sus.2.34>.
- Y. Liu, X. Xu, Z. Shao, S.P. Jiang, Metal-organic frameworks derived porous carbon, metal oxides and metal sulfides-based compounds for supercapacitors application, *Energy Storage Materials* 26 (2020) 1–22, <https://doi.org/10.1016/j.ensm.2019.12.019>.
- J. Tang, C. Su, Z. Shao, Covalent Organic Framework (COF)-Based Hybrids for Electrocatalysis: Recent Advances and Perspectives, *Small, Methods* 5 (2021) 2100945, <https://doi.org/10.1002/smt.202100945>.
- Y. Li, L. Zhou, S. Guo, Noble metal-free electrocatalytic materials for water splitting in alkaline electrolyte, *EnergyChem* 3 (2021), <https://doi.org/10.1016/j.enchem.2021.100053>.
- M.G. Mohamed, E.C. Atayde Jr, M.B. Matsagar, J. Na, Y. Yamauchi, K.C.W. Wu, S.W. Kuo, Construction Hierarchically Mesoporous/Microporous Materials Based on Block Copolymer and Covalent Organic Framework, *J. Taiwan Inst. Chem. Eng.* 112 (2020) 180–192, <https://doi.org/10.1016/j.jtice.2020.06.013>.
- X. Li, X. Yang, H. Xue, H. Pang, Q. Xu, Metal-organic frameworks as a platform for clean energy applications, *EnergyChem* 2 (2020) 1000271, <https://doi.org/10.1016/j.enchem.2020.100027>.
- M.G. Mohamed, A.F.M. EL-Mahdy, M.G. Kotp, S.W. Advances in porous organic polymers: syntheses, structures, and diverse applications, *Mater. Adv.* (3) (2022) 707–733. [10.1039/D1MA00771H](https://doi.org/10.1039/D1MA00771H).
- S.-Y. Ding, W. Wang, Covalent organic frameworks (COFs): from design to applications, *Chem. Soc. Rev.* 42 (2013) 548–568, <https://doi.org/10.1039/C2CS35072F>.
- X. Gao, Y. Dong, S. Li, J. Zhou, L. Wang, B. Wang, MOFs and COFs for Batteries and Supercapacitors, *Electrochem. Energy Rev.* 3 (2020) 81–126, <https://doi.org/10.1007/s41918-019-00055-1>.
- Q. Fang, Z. Zhuang, S. Gu, R.B. Kaspar, J. Zheng, J. Wang, S. Qiu, Y. Yan, Designed synthesis of large-pore crystalline polyimide covalent organic frameworks, *Nat. Commun.* 5 (2014) 1–8, <https://doi.org/10.1038/ncomms5503>.
- T. Ben, S. Qiu, Porous aromatic frameworks: Synthesis, structure and functions, *CrystEngComm* 15 (2013) 17–26, <https://doi.org/10.1039/C2CE25409C>.
- A. Shahvar, R. Soltani, M. Saraji, M. Dinari, S. Alijani, Covalent triazine-based framework for micro solid-phase extraction of parabens, *J. Chromatogr. A* 1565 (2018) 48–56, <https://doi.org/10.1016/j.chroma.2018.06.033>.
- L. Akyuz, An imine based COF as a smart carrier for targeted drug delivery: From synthesis to computational studies, *Microporous Mesoporous Mater.* 294 (2020), <https://doi.org/10.1016/j.micromeso.2019.109850>.
- J. Cao, X. Li, H. Tian, Metal-Organic Framework (MOF)-Based Drug Delivery, *Curr. Med. Chem.* 27 (2020) 5949–5969, <https://doi.org/10.2174/0929867326666190618152518>.
- T. Sick, A.G. Hufnagel, J. Kampmann, I. Kondofersky, M. Calik, J.M. Rotter, A. Evans, M. Döblinger, S. Herbert, K. Peters, Oriented Films of Conjugated 2D Covalent Organic Frameworks as Photocathodes for Water Splitting, *J. Am. Chem. Soc.* 140 (2017) 2085–2092, <https://doi.org/10.1021/jacs.7b06081>.
- Y. Zheng, S. Zheng, H. Xue, H. Pang, Metal-Organic Frameworks/Graphene-Based Materials: Preparations and Applications, *Adv. Funct. Mater.* 28 (2018) 1804950, <https://doi.org/10.1002/adfm.201804950>.
- W. Liu, X.-B. Yin, Metal-organic frameworks for electrochemical applications, *TrAC, Trends Anal. Chem.* 75 (2016) 86–96, <https://doi.org/10.1016/j.trac.2015.07.011>.
- Z. Zhao, J. Ding, R. Zhu, H. Pang, The synthesis and electrochemical applications of core-shell MOFs and their derivatives, *J. Mater. Chem. A* 7 (2019) 15519–15540, <https://doi.org/10.1039/C9TA03833G>.
- X. Xiao, L. Zou, H. Pang, Q. Xu, Synthesis of micro/nanoscaled metal-organic frameworks and their direct electrochemical applications, *Chem. Soc. Rev.* 49 (2020) 301–331, <https://doi.org/10.1039/C7CS00614D>.
- N. ul Qadir, S. A. M. Said, H. M. Bahaidarah, Structural stability of metal organic frameworks in aqueous media – Controlling factors and methods to improve hydrostability and hydrothermal cyclic stability, *Microporous Mesoporous Mater.*, (201) (2015) 61–90. [10.1016/j.micromeso.2014.09.034](https://doi.org/10.1016/j.micromeso.2014.09.034).
- Y. Xue, S. Zheng, H. Xue, H. Pang, Metal-organic framework composites and their electrochemical applications, *J. Mater. Chem. A* 7 (2019) 7301–7327, <https://doi.org/10.1039/C8TA12178H>.
- C.G. Piscopo, S. Loebbecke, Strategies to Enhance Carbon Dioxide Capture in Metal-Organic Frameworks, *Chempluschem* 85 (2020) 538–547, <https://doi.org/10.1002/cplu.202000072>.
- O.M. Yaghi, H. Li, Hydrothermal Synthesis of a Metal-Organic Framework Containing Large Rectangular Channels, *J. Am. Chem. Soc.* 117 (1995) 10401–10402, <https://doi.org/10.1021/ja00146a033>.
- H. Furukawa, K.E. Cordova, M. O’Keeffe, O.M. Yaghi, The chemistry and applications of metal-organic frameworks, *Science* 341 (2013) 974, <https://doi.org/10.1126/science.1230444>.
- O.K. Farha, I. Eryazici, N.C. Jeong, B.G. Hauser, C.E. Wilmer, A.A. Sarjeant, R.Q. Snurr, S.T. Nguyen, A.O. Yazaydin, J.T. Hupp, Metal-Organic Framework Materials with Ultrahigh Surface Areas: Is the Sky the Limit?, *J. Am. Chem. Soc.* 134 (2012) 15016–15021, <https://doi.org/10.1021/ja3055639>.
- W. Wang, X. Xu, W. Zhou, Z. Shao, Recent Progress in Metal-Organic Frameworks for Applications in Electrocatalytic and Photocatalytic Water Splitting, *Adv. Sci.* 4 (2017) 1600371, <https://doi.org/10.1002/advs.201600371>.
- J.Y. Huang, F. Ding, B.I. Yakobson, P. Lu, L. Qi, J. Li, In situ observation of graphene sublimation and multi-layer edge reconstructions, *Proc. Natl. Acad. Sci.* 106 (2009) 10103–10108, <https://doi.org/10.1073/pnas.0905193106>.
- G. Chakraborty, I.-H. Park, R. Medishetty, J.J. Vital, Two-Dimensional Metal-Organic Framework Materials: Synthesis, Structures, Properties and Applications, *Chem. Rev.* 121 (2021) 3751–3891, <https://doi.org/10.1021/acs.chemrev.0c01049>.
- J. Wang, N. Li, Y. Xu, H. Pang, Two-Dimensional MOF and COF Nanosheets: Synthesis and Applications in Electrochemistry, *Chem. Eur. J.* 26 (2020) 6402–6422, <https://doi.org/10.1002/chem.202000294>.
- C. Healy, K.M. Patil, B.H. Wilson, L. Hermanspahn, N.C. Harvey-Reid, B.I. Howard, C. Kleinjan, J. Kolien, F. Payet, S.G. Telfer, The Thermal Stability of

- Metal-Organic Frameworks, *Coord. Chem. Rev.* 419 (2020), <https://doi.org/10.1016/j.ccr.2020.213388>.
- [41] M. Ding, X. Cai, H.-L. Jiang, Improving MOF stability: approaches and applications, *Chem. Sci.* 10 (2019) 10209–10230, <https://doi.org/10.1039/C9SC03916C>.
- [42] K.B. Wang, Q. Xun, Q. Zhang, Recent progress in metal-organic frameworks as active materials for supercapacitors, *EnergyChem* 2 (2020), <https://doi.org/10.1016/j.enchem.2019.100025>.
- [43] Y. Li, Y. Xu, W. Yang, W. Shen, H. Xue, H. Pang, MOF-Derived Metal Oxide Composites for Advanced Electrochemical Energy Storage, *Small* 14 (2018) 1704435, <https://doi.org/10.1002/smll.201704435>.
- [44] J. Liu, D. Zhu, C. Guo, A. Vasileff, S. Qiao, Design Strategies toward Advanced MOF-Derived Electrocatalysts for Energy-Conversion Reactions, *Adv. Energy Mater.* 7 (2017) 1700518, <https://doi.org/10.1002/aenm.201700518>.
- [45] X. Wang, J. Zhou, H. Fu, W. Li, X. Fan, G. Xin, J. Zheng, X. Li, MOF derived catalysts for electrochemical oxygen reduction, *J. Mater. Chem. A* 2 (2014) 14064–14070, <https://doi.org/10.1039/C4TA01506A>.
- [46] Z.C. Yao, T. Tang, J.S. Hu, L.J. Wan, Recent Advances on Nonprecious-Metal-Based Bifunctional Oxygen Electrocatalysts for Zinc-Air Batteries, *Energy Fuels* 35 (2021) 6380–6401, <https://doi.org/10.1021/acs.energyfuels.1c00275>.
- [47] Q. Wang, D. Astruc, State of the Art and Prospects in Metal-Organic Framework (MOF)-Based and MOF-Derived Nanocatalysis, *Chem. Rev.* 120 (2019) 1438–1511, <https://doi.org/10.1021/acs.chemrev.9b00223>.
- [48] X. Liu, H. Pang, X. Liu, Q. Li, N. Zhang, L. Mao, M. Qiu, B. Hu, H. Yang, X. Wang, Orderly Porous Covalent Organic Frameworks-based Materials: Superior Adsorbents for Pollutants Removal from Aqueous Solutions, *Innov.* 2 (2021), <https://doi.org/10.1016/j.xinn.2021.100076>.
- [49] A.P. Cote, A.I. Benin, N.W. Ockwig, M. O’Keeffe, A.J. Matzger, O.M. Yaghi, Porous, crystalline, covalent organic frameworks, *Science* 310 (2005) 1166–1170, <https://doi.org/10.1126/science.1120411>.
- [50] S. Wan, J. Guo, J. Kim, H. Ihee, D. Jiang, A Photoconductive Covalent Organic Framework: Self-Condensed Arene Cubes Composed of Eclipsed 2D Polypyrene Sheets for Photocurrent Generation, *Angew. Chemie Int. Ed.* 48 (2009) 5439–5442, <https://doi.org/10.1002/anie.200900881>.
- [51] L. Stegbauer, K. Schwinghammer, B.V. Lotsch, A hydrazone-based covalent organic framework for photocatalytic hydrogen production, *Chem. Sci.* 5 (2014) 2789–2793, <https://doi.org/10.1039/C4SC00016A>.
- [52] C. Chen, T. Joshi, H. Li, A.D. Chavez, Z. Pedramrazi, P.-N. Liu, H. Li, W.R. Dichtel, J.-L. Bredas, M.F. Crommie, Local Electronic Structure of a Single-Layer Porphyrin-Containing Covalent Organic Framework, *ACS Nano* 12 (2018) 385–391, <https://doi.org/10.1021/acs.nano.7b06529>.
- [53] J. You, Y. Zhao, L. Wang, W. Bao, Recent developments in the photocatalytic applications of covalent organic frameworks: A review, *J. Clean. Prod.* 291 (2021), <https://doi.org/10.1016/j.jclepro.2021.125822>.
- [54] Q. Yang, M. Luo, K. Liu, H. Cao, H. Yan, Covalent organic frameworks for photocatalytic applications, *Appl. Catal. B Environ.* 276 (2020), <https://doi.org/10.1016/j.apcatb.2020.119174>.
- [55] S. Lin, C.S. Diercks, Y.-B. Zhang, N. Kornienko, E.M. Nichols, Y. Zhao, A.R. Paris, D. Kim, P. Yang, O.M. Yaghi, Covalent organic frameworks comprising cobalt porphyrins for catalytic CO₂ reduction in water, *Science* 349 (2015) 1208–1213, <https://doi.org/10.1126/science.aac8343>.
- [56] X. Zhao, P. Pachfule, A. Thomas, Covalent organic frameworks (COFs) for electrochemical applications, *Chem. Soc. Rev.*, (50) (2021) 6871–6913, <https://doi.org/10.1039/D0CS01569E>.
- [57] T. Li, X. Yan, W.-D. Zhang, W.-K. Han, Y. Liu, Y. Li, H. Zhu, Z. Li, Z.-G. Gu, A 2D donor-acceptor covalent organic framework with charge transfer for supercapacitors, *Chem. Commun.* 56 (2020) 14187–14190, <https://doi.org/10.1039/D0CC04109B>.
- [58] Y. Lu, Y. Cai, Q. Zhang, J. Chen, Structure-Performance Relationships of Covalent Organic Framework Electrode Materials in Metal-Ion Batteries, *J. Phys. Chem. Lett.* 12 (2021) 8061–8071, <https://doi.org/10.1021/acs.jpcllett.1c02004>.
- [59] Q. Zhu, X. Wang, R. Clowes, P. Cui, L. Chen, M.A. Little, A.I. Cooper, 3D Cage COFs: A Dynamic Three-Dimensional Covalent Organic Framework with High-Connectivity Organic Cage Nodes, *J. Am. Chem. Soc.* 142 (2020) 16842–16848, <https://doi.org/10.1021/jacs.0c07732>.
- [60] Y. An, S. Tan, Y. Liu, K. Zhu, L. Hu, Y. Rong, Q. An, Designs and applications of multi-functional covalent organic frameworks in rechargeable batteries, *Energy Storage Mater.* 41 (2021) 354–379, <https://doi.org/10.1016/j.ensm.2021.06.010>.
- [61] X. Zhao, P. Pachfule, S. Li, T. Langenhahn, M. Ye, C. Schlesiger, S. Praetzel, J. Schmidt, A. Thomas, Macro/Microporous Covalent Organic Frameworks for Efficient Electrocatalysis, *J. Am. Chem. Soc.*, (141) (2019) 6623–6630, <https://doi.org/10.1021/jacs.9b01226>.
- [62] F. Haase, P. Hirschle, R. Freund, S. Furukawa, Z. Ji, S. Wuttke, Beyond Frameworks: Structuring Reticular Materials across Nano-, Meso-, and Bulk Regimes, *Angew. Chemie Int. Ed.* 59 (2020) 22350–22370, <https://doi.org/10.1002/anie.201914461>.
- [63] S. Kandambeth, K. Dey, R. Banerjee, Covalent Organic Frameworks: Chemistry beyond the Structure, *J. Am. Chem. Soc.* 141 (2018) 1807–1822, <https://doi.org/10.1021/jacs.8b10334>.
- [64] T. Banerjee, K. Gottschling, G. Savasci, C. Ochsenfeld, B.V. Lotsch, H₂ Evolution with Covalent Organic Framework Photocatalysts, *ACS Energy Lett.* 3 (2018) 400–409, <https://doi.org/10.1021/acseenergylett.7b01123>.
- [65] B.P. Biswal, H.A. Vignolo-González, T. Banerjee, L. Grunenberg, G. Savasci, K. Gottschling, J. Nuss, C. Ochsenfeld, B.V. Lotsch, Sustained Solar H₂ Evolution from a Thiazolo[5,4-d]thiazole-Bridged Covalent Organic Framework and Nickel-Thiolate Cluster in Water, *J. Am. Chem. Soc.* 141 (2019) 11082–11092, <https://doi.org/10.1021/jacs.9b03243>.
- [66] X. Wang, L. Chen, S.Y. Chong, M.A. Little, Y. Wu, W.-H. Zhu, R. Clowes, Y. Yan, M.A. Zwiijnenburg, R.S. Sprick, Sulfone-containing covalent organic frameworks for photocatalytic hydrogen evolution from water, *Nat. Chem.* 10 (2018) 1180–1189, <https://doi.org/10.1038/s41557-018-0141-5>.
- [67] M.M. Samy, I.M.A. Mekheimer, M.G. Mohamed, M.H. Elsayed, K.H. Lin, Y.K. Chen, T.L. Wu, H.H. Chou, S.W. Kuo, Conjugated microporous polymers incorporating Thiazolo[5,4-d]thiazole moieties for Sunlight-Driven hydrogen production from water, *Chem. Eng. J.* (446) (2022) 137158, <https://doi.org/10.1016/j.cej.2022.137158>.
- [68] M.G. Mohamed, M.H. Elsayed, Y. Ye, M.M. Samy, A.E. Hassan, T.H. Mansoure, Z. Wen, H.H. Chou, K.H. Chen, S.W. Kuo, Construction Porous Organic/Inorganic Hybrids Polymers Based on Polyhedral Oligomeric silsesquioxane for Energy Storage and Hydrogen Production from Water, *Polymers* 15 (2023) 182, <https://doi.org/10.3390/polym15010182>.
- [69] S. Kevin, R.V. De Krol, Semiconducting materials for photoelectrochemical energy conversion, *Nat. Rev. Mater.* 12 (2016) 1–16, <https://doi.org/10.1038/natrevmats.2016.10>.
- [70] Q.H. Qian, P.A. Asinger, M.J. Lee, G. Han, K.M. Rodriguez, S. Lin, F.M. Benedetti, A. X. Wu, W.S. Chi, Z.P. Smith, MOF-based membranes for gas separations, *Chem. Rev.* 120 (2020) 8161–8266, <https://doi.org/10.1021/acs.chemrev.0c00119>.
- [71] Y.Y. Zhang, X. Feng, S. Yuan, J.W. Zhou, B. Wang, Challenges and recent advances in MOF-polymer composite membranes for gas separation, *Inorg. Chem. Front* 3 (2016) 896–909, <https://doi.org/10.1039/c6qi00042h>.
- [72] D. Alezi, Y. Belmabkhout, M. Suyetin, P.M. Bhatt, Ł.J. Weseliński, V. Solovyeva, K. Adil, I. Spanopoulos, P.N. Trikalitis, A.H. Emwas, M. Eddaoudi, MOF Crystal Chemistry Paving the Way to Gas Storage Needs: Aluminum-Based soc-MOF for CH₄, O₂, and CO₂ Storage, *J. Am. Chem. Soc.* 137 (2015) 13308–13318, <https://doi.org/10.1021/jacs.5b07053>.
- [73] H. Li, L.B. Li, R.B. Lin, W. Zhou, Z.J. Zhang, S.C. Xiang, B.L. Chen, Porous metal-organic frameworks for gas storage and separation: Status and challenges, *EnergyChem* 1 (2019) 10006, <https://doi.org/10.1016/j.enchem.2019.100006>.
- [74] M.L. Ding, R.W. Flaig, H.L. Jiang, O.M. Yaghi, Carbon capture and conversion using metal-organic frameworks and MOF-based materials, *Chem. Soc. Rev.* 48 (2019) 2783–2828, <https://doi.org/10.1039/C8CS00829A>.
- [75] H.D. Lawson, S.P. Walton, C. Chan, Metal-Organic Frameworks for Drug Delivery: A Design Perspective, *ACS Appl. Mater. Interfaces* 13 (2021) 7004–7020, <https://doi.org/10.1021/acsami.1c01089>.
- [76] M.X. Wu, Y.W. Yang, Metal-Organic Framework (MOF)-Based Drug/Cargo Delivery and Cancer Therapy, *Adv. Mater.* 29 (2017) 1606134, <https://doi.org/10.1002/adma.201606134>.
- [77] B. Yan, Photofunctional MOF-based hybrid materials for the chemical sensing of biomarkers, *J. Mater. Chem. C* (7) (2019) 8155–8175, <https://doi.org/10.1039/C9TC01477B>.
- [78] J.F. Olorunyomi, S.T. Geh, R.A. Caruso, C.M. Doherty, Metal-organic frameworks for chemical sensing devices, *Mater. Horiz* 8 (2021) 2387–2419, <https://doi.org/10.1039/D1MH00609F>.
- [79] Z.C. Hu, B.J. Deibert, J. Li, Luminescent metal-organic frameworks for chemical sensing and explosive detection, *Chem. Soc. Rev.* 43 (2014) 5815–5840, <https://doi.org/10.1039/C4CS00010B>.
- [80] M.J. Hao, M.Q. Qiu, H. Yang, B.W. Hu, X.X. Wang, Recent advances on preparation and environmental applications of MOF-derived carbons in catalysis, *Science of the Total Environment* 760 (2021) 143333, <https://doi.org/10.1016/j.scitotenv.2020.143333>.
- [81] D.D. Li, H.Q. Xu, L. Jiao, H.L. Jiang, Metal-organic frameworks for catalysis: State of the art, challenges, and opportunities, *EnergyChem* 1 (2019) 2589–7780, <https://doi.org/10.1016/j.enchem.2019.100005>.
- [82] Y.T. Liao, B.M. Matsagar, K.C.W. Wu, Metal-organic framework (MOF)-derived effective solid catalysts for valorization of lignocellulosic biomass, *ACS Sustainable Chem. Eng* 6 (2018) 13628–13643, <https://doi.org/10.1021/acssuschemeng.8b03683>.
- [83] Y.G. Li, J.J. Hu, J.L. Zhang, S.J. Liu, Y. Peng, H.R. Wen, Lanthanide-based metal-organic framework materials as bifunctional fluorescence sensors toward acetylacetone and aspartic acid, *Crystengcomm* 24 (2022) 2464–2471, <https://doi.org/10.1039/D2CE00174H>.
- [84] J.L.C. Rowsell, J. Eckert, O.M. Yaghi, Characterization of H₂ Binding Sites in Prototypical Metal-Organic Frameworks by Inelastic Neutron Scattering, *J. Am. Chem. Soc.* 127 (2005) 14904–14910, <https://doi.org/10.1021/ja0542690>.
- [85] P. Rocio-Bautista, I. Taima-Mancera, J. Pasan, V. Pino, Metal-Organic Frameworks in Green Analytical Chemistry, *Separations* 6 (2019) 33, <https://doi.org/10.3390/separations6030033>.
- [86] A.E. Baumann, D.A. Burns, B.Q. Liu, V.S. Thoi, Metal-organic framework functionalization and design strategies for advanced electrochemical energy storage devices, *Commun Chem* 2 (2019) 86, <https://doi.org/10.1038/s42004-019-0184-6>.
- [87] K.S. Novoselov, A.K. Geim, S.V. Morozov, D. Jiang, Y. Zhang, S.V. Dubonos, I.V. Grigorieva, A.A. Electric Field Effect in Atomically Thin Carbon Films, *Fisov, Science*, (306) (2004) 666–669, <https://www.science.org/10.1126/science.1102896>.
- [88] S.M. Moosavi, A. Nandy, K.M. Jablonka, D. Ongari, J.P. Janet, P.G. Boyd, Y. Lee, B. Smit, H.J. Kulik, Understanding the diversity of the metal-organic

- framework ecosystem, *Nat. Commun.* 11 (2020) 4068, <https://doi.org/10.1038/s41467-020-17755-8>.
- [89] K.Y. Zou, Z.X. Li, Controllable Syntheses of MOF-Derived Materials, *Chem. Eur. J.* 24 (2017) 6506–6518, <https://doi.org/10.1002/chem.201705415>.
- [90] K. Shen, X.D. Chen, J.Y. Chen, Y.W. Li, Development of MOF-Derived Carbon-Based Nanomaterials for Efficient Catalysis, *ACS Catal.* 6 (2016) 5887–5903, <https://doi.org/10.1021/acscatal.6b01222>.
- [91] Y.R. Lee, J. Kim, W.S. Ahn, Synthesis of metal-organic frameworks: A mini review, *Korean J Chem Eng* 30 (2013) 1667–1680, <https://doi.org/10.1007/s11814-013-0140-6>.
- [92] N. Stock, S. Biswas, Synthesis of Metal-Organic Frameworks (MOFs): Routes to Various MOF Topologies, Morphologies, and Composites, *Chem. Rev.* 112 (2012) 933–969, <https://doi.org/10.1021/cr200304e>.
- [93] R. Banerjee, A. Phan, B. Wang, C. Knobler, H. Furukawa, M. O’Keeffe, O.M. Yaghi, High-Throughput Synthesis of Zeolitic Imidazolate Frameworks and Application to CO₂ Capture, *Science* 319 (2008) 939–943, <https://www.science.org/10.1126/science.1152516>.
- [94] M. Safaei, M.M. Foroughi, N. Ebrahimipour, S. Jahani, A. Omid, M. Khatami, A review on metal-organic frameworks: Synthesis and applications, *Trends Anal. Chem.* 118 (2019) 401–425, <https://doi.org/10.1016/j.trac.2019.06.007>.
- [95] Y. Qi, F. Luo, Y.X. Che, J.M. Zhen, Hydrothermal Synthesis of Metal–Organic Frameworks Based on Aromatic Polycarboxylate and Flexible Bis(imidazole) Ligands, *Cryst. Growth. Des.* 8 (2008) 606–611, <https://doi.org/10.1021/cg700758c>.
- [96] S. Neugebauer, U. Muller, T. Lohmuller, J.R. Spatz, M. Stelzle, W. Schuhmann, Characterization of Nanopore Electrode Structures as Basis for Amplified Electrochemical Assays, *Electroanalysis* 18 (2006) 1929–1936, <https://doi.org/10.1002/elan.200603612>.
- [97] O.J.D. Neto, A.C.D. Fros, B.S. Barros, A.F.D. Monteiro, J. Kulesza, Rapid and efficient electrochemical synthesis of a zinc-based nano-MOF for Ibuprofen adsorption, *New J. Chem.* 43 (2019) 5518–5524, <https://doi.org/10.1039/C8NJ06420B>.
- [98] H.M. Yang, X. Liu, X.L. Song, T.L. Yang, Z.H. Liang, C.M. Fan In situ electrochemical synthesis of MOF-5 and its application in improving photocatalytic activity of BiOBr, *Nonferrous Met. Soc. (25)* (2015) 3987–3994, 10.1016/S1003-6326(15)64047-X.
- [99] A. Pichon, A. Lazuen-Garay, S.L. James, CrystEngComm, Solvent-free synthesis of a microporous metal–organic framework, *CrystEngComm*, (8) (2006) 211–214, 10.1039/B513750K.
- [100] M. Klimakow, P. Klobes, A.F. Thunemann, K. Rademann, F. Emmerling, Mechanochemical Synthesis of Metal–Organic Frameworks: A Fast and Facile Approach toward Quantitative Yields and High Specific Surface Areas, *Chem. Mater.* 22 (2010) 5216–5221, <https://doi.org/10.1021/cm1012119>.
- [101] D. Chen, J.H. Zhao, P.F. Zhang, S. Dai, Mechanochemical synthesis of metal-organic frameworks, *Polyhedron* 162 (2019) 59–64, <https://doi.org/10.1016/j.poly.2019.01.024>.
- [102] S.H. Lo, D.S. Raja, C.W. Chen, Y.H. Kang, J.J. Chen, C.H. Lin, Waste polyethylene terephthalate (PET) materials as sustainable precursors for the synthesis of nanoporous MOFs, MIL-47, MIL-53(Cr, Al, Ga) and MIL-101(Cr), *Dalton Trans* 45 (2016) 9565–9573, <https://doi.org/10.1039/C6DT01282E>.
- [103] R.R. Mishra, A.K. Sharma, Microwave–material interaction phenomena: Heating mechanisms, challenges and opportunities in material processing, *Compos. Part A Appl. Sci. Manuf.* 81 (2016) 78–97, <https://doi.org/10.1016/j.compositesa.2015.10.035>.
- [104] J. Wegner, S. Ceylan, A. Kirschning, Flow Chemistry – A Key Enabling Technology for (Multistep) Organic Synthesis, *Adv. Synth. Catal.* 354 (2012) 17–57, <https://doi.org/10.1002/adsc.201100584>.
- [105] S.H. Jung, J.H. Lee, J.S. Chang, Microwave Synthesis of a Nanoporous Hybrid Material, Chromium Trimesate, *Bull. Korean Chem. Soc.* 26 (2005) 880–881, <https://doi.org/10.5012/bkcs.2005.26.6.880>.
- [106] S.H. Jung, J.S. Chang, J.S. Hwang, S.E. Park, Selective formation of SAPO-5 and SAPO-34 molecular sieves with microwave irradiation and hydrothermal heating, *Microporous Mesoporous Mater.* 64 (2003) 33–39, [https://doi.org/10.1016/S1387-1811\(03\)00501-8](https://doi.org/10.1016/S1387-1811(03)00501-8).
- [107] C.C. Coussios, C.H. Farny, G. Ter Haar, R.A. Roy, Role of acoustic cavitation in the delivery and monitoring of cancer treatment by high-intensity focused ultrasound (HIFU), *Int. J. Hyperther.* 23 (2007) 105–120, <https://doi.org/10.1080/02656730701194131>.
- [108] W.J. Son, J. Kim, J. Kim, W.S. Ahn, Sonochemical synthesis of MOF-5, *Chem. Commun* (2008) 6336–6338, <https://doi.org/10.1039/B814740J>.
- [109] L.G. Qiu, Z.Q. Li, Y. Wu, W. Wang, T. Xu, X. Jiang, Facile synthesis of nanocrystals of a microporous metal–organic framework by an ultrasonic method and selective sensing of organoamines, *Chem. Commun* (2008) 3642–3644, <https://doi.org/10.1039/B804126A>.
- [110] A. Gedanken, Using sonochemistry for the fabrication of nanomaterials, *Ultrason. Sonochem.* 11 (2004) 47–55, <https://doi.org/10.1016/j.ultrasonch.2004.01.037>.
- [111] J.H. Lee, C.Y. Koh, J.P. Singer, S.J. Jeon, M. Maldovan, O. Stein, E.L. Thomas, 25th Anniversary article: ordered polymer structures for the engineering of photons and phonons, *Adv. Mater.* 26 (2014) 532–569, <https://doi.org/10.1002/adma.201303456>.
- [112] E. Yashima, K. Maeda, H. Iida, Y. Furusho, K. Nagai, Helical polymers: synthesis, structures, and functions, *Chem. Rev.* 109 (2009) 6102–6211, <https://doi.org/10.1021/cr900162q>.
- [113] G.W. Coates, Precise control of polyolefin stereochemistry using single-site metal catalysts, *Chem. Rev.* 100 (2000) 1223–1252, <https://doi.org/10.1021/cr990286u>.
- [114] R.O. Ebeuele, Polymer science and technology, CRC Press 504 (2000) 1–544, <https://doi.org/10.1201/9781420057805>.
- [115] P.J. Flory, Principles of polymer chemistry 672 (1953), <https://doi.org/10.1007/978-1-4614-2212-9>.
- [116] G. Yilmaz, Y. Yagci, Light-induced step-growth polymerization, *Prog. Polym. Sci.* 100 (2020), <https://doi.org/10.1016/j.progpolymsci.2019.101178>.
- [117] M. Kamigaito, T. Ando, M. Sawamoto, Metal-catalyzed living radical polymerization, *Chem. Rev.* 101 (2001) 3689–3746, <https://doi.org/10.1021/cr9901182>.
- [118] S. Wang, C. Zhang, Y. Shu, S. Jiang, Q. Xia, L. Chen, S. Jin, I. Hussain, A.I. Cooper, B. Tan, Layered Microporous Polymers by Solvent Knitting Method, *Sci. Adv.* 3 (2017) e1602610.
- [119] M.G. Mohamed, M.H. Elsayed, A.M. Elewa, A.F.M. EL-Mahdy, C.H. Yang, A.A.K. Mohammed, H.H. Chou, S.W. Kuo, Pyrene-containing conjugated organic microporous polymers for photocatalytic hydrogen evolution from water, *Catal. Sci. Technol.*, (11) (2021), 10.1039/D0CY02482A.
- [120] X. Li, C. Zhang, S. Cai, X. Lei, V. Altoe, F. Hong, J.J. Urban, J. Ciston, E.M. Chan, Y. Liu, Facile transformation of imine covalent organic frameworks into ultrastable crystalline porous aromatic frameworks, *Nat. Commun.* 9 (2018) 2998, <https://doi.org/10.1038/s41467-018-05462-4>.
- [121] J. Wei, Z. Sun, W. Luo, Y. Li, A.A. Elzatory, A.M. Al-Enizi, Y. Deng, D. Zhao, New Insight into the Synthesis of Large-Pore Ordered Mesoporous Materials, *J. Am. Chem. Soc.* 139 (2017) 1706–1713, <https://doi.org/10.1021/jacs.6b11411>.
- [122] X.Y. Yang, L.H. Chen, J.C. Rooke, C. Sanchez, Hierarchically porous materials: synthesis strategies and structure design, *Chem. Soc. Rev.* 46 (2017) 481–558, <https://doi.org/10.1039/C6CS00829A>.
- [123] L. Yu, X. Shang, H. Chen, L. Xiao, Y. Zhu, J. Fan, A tightly-bonded and flexible mesoporous zeolite–cotton hybrid hemostat, *Nat. Commun.* 10 (2019) 1932, <https://doi.org/10.1038/s41467-019-09849-9>.
- [124] M. Manzano, M. Vallet-Regi, Mesoporous silica nanoparticles for drug delivery, *Adv. Funct. Mater.* 30 (2020) 1902634, <https://doi.org/10.1002/adfm.201902634>.
- [125] T. Feng, B. Sun, Q. Hao, J. Li, Y. Xu, H. Shang, D. Wang, Ambient synthesis of metal–covalent organic frameworks with Fe-iminopyridine linkages, *Chem. Commun.* 58 (2022) 8830–8833, <https://doi.org/10.1039/D2CC03148E>.
- [126] W.C. Chen, M.M.M. Ahmed, C.F. Wang, C.F. Huang, S.W. Kuo, Highly thermally stable mesoporous Poly (cyanate ester) featuring double-decker-shaped polyhedral silsesquioxane framework, *Polymer* 185 (2019), <https://doi.org/10.1016/j.polymer.2019.121940>.
- [127] J.G. Li, Y.F. Ho, M.M.M. Ahmed, H.C. Liang, S.W. Kuo, Mesoporous carbons templated by PEO-PCL block copolymers as electrode materials for supercapacitors, *Chem. Eur. J.* 25 (2019) 10456–10463, <https://doi.org/10.1002/chem.201901724>.
- [128] K.S. Lakhii, D.H. Park, K. Al-Bahily, W. Cha, B. Viswanathan, J.H. Choy, A. Vinu, Mesoporous carbon nitrides: synthesis, functionalization, and applications, *Chem. Soc. Rev.* 46 (2017) 72–101, <https://doi.org/10.1039/C6CS00532B>.
- [129] A.G. Slater, A.I. Cooper, Porous materials. Function-led design of new porous materials, *Science* 348 (2015) 8075, <https://doi.org/10.1126/science.aaa8075>.
- [130] A.I. Cooper, Conjugated microporous polymers, *Adv. Mater.* 26 (2009) 1291–1295, <https://doi.org/10.1002/adma.200801971>.
- [131] M.G. Mohamed, T.C. Chen, S.W. Kuo, Solid-State Chemical Transformations to Enhance Gas Capture in Benzoxazine-Linked Conjugated Microporous Polymers, *Macromolecules* 54 (2021) 5866–5877, <https://doi.org/10.1021/acs.macromol.1c00736>.
- [132] S. Das, P. Heasman, T. Ben, S. Qiu, Porous organic materials: strategic design and structure–function correlation, *Chem. Rev.* 117 (2017) 1515–1563, <https://doi.org/10.1021/acs.chemrev.6b00439>.
- [133] M.G. Mohamed, M.M.M. Ahmed, W.T. Du, S.W. Kuo, Meso/Microporous Carbons from Conjugated Hyper-Crosslinked Polymers Based on Tetraphenylethene for High-Performance CO₂ Capture and Supercapacitor, *Molecules* 26 (2021) 738, <https://doi.org/10.3390/molecules26030738>.
- [134] C. Young, T. Park, J.W. Yi, J. Kim, M.S.A. Hossain, Y.V. Kaneti, Y. Yamauchi, Advanced Functional Carbons and Their Hybrid Nanoarchitectures Towards Supercapacitor Applications, *ChemSusChem* 11 (2018) 3546–3558, <https://doi.org/10.1002/cssc.201801525>.
- [135] K. Geng, V. Arumugam, H. Xu, Y. Gao, D. Jiang, Covalent organic frameworks: Polymer chemistry and functional design, *Prog. Polym. Sci.* 108 (2020), <https://doi.org/10.1016/j.progpolymsci.2020.101288>.
- [136] M.G. Mohamed, C.C. Lee, A.F.M. EL-Mahdy, J. Lüder, M.H. Yu, Z. Li, Z. Zhu, C.C. Chueh, S.W. Kuo, Exploitation of two-dimensional conjugated covalent organic frameworks based on tetraphenylethylene with bicarbazole and pyrene units and applications in perovskite solar cells, *J. Mater. Chem. A*, (8) (2020) 11448–11459, 10.1039/D0TA02956D.
- [137] R. Liu, K.T. Tan, Y. Gong, Y. Chen, Z. Li, S. Xie, T. He, Z. Lu, H. Yang, D. Jiang, Covalent organic frameworks: an ideal platform for designing ordered materials and advanced applications, *Chem. Soc. Rev.* 50 (2021) 120–242, <https://doi.org/10.1039/D0CS00620C>.
- [138] L. Gong, X. Yang, Y. Gao, G. Yang, Z. Yu, X. Fu, Y. Wang, D. Qi, Y. Bian, K. Wang, J. Jiang, Two-dimensional covalent organic frameworks with p- and bipolar-type redox-active centers for organic high-performance Li-ion battery cathodes, *J. Mater. Chem. A* 10 (2022) 16595–16601, <https://doi.org/10.1039/D2TA03579K>.

- [139] T. Sun, J. Xie, W. Guo, D.S. Li, Q. Zhang, Covalent-Organic Frameworks: Advanced Organic Electrode Materials for Rechargeable Batteries, *Adv. Energy Mater.* 10 (2020) 1904199.
- [140] G. Zhao, L. Xu, J. Jiang, Z. Mei, Q. An, P. Lv, X. Yang, H. Guo, X. Sun, COFs-based electrolyte accelerates the Na⁺ diffusion and restrains dendrite growth in quasi-solid-state organic batteries, *Nano Energy* 92 (2022), <https://doi.org/10.1016/j.nanoen.2021.106756>.
- [141] X. Luo, W. Li, H. Liang, H. Zhang, K. Du, X. Wang, X. Liu, J. Zhang, X. Wu, Covalent Organic Framework with Highly Accessible Carbonyls and π -Cation Effect for Advanced Potassium-Ion Batteries, *Angew. Chem., Int. Ed.* 61 (2022) e202117661.
- [142] Z. Wang, S. Gu, L. Cao, L. Kong, Z. Wang, N. Qin, M. Li, W. Luo, J. Chen, S. Wu, G. Liu, H. Yuan, Y. Bai, K. Zhang, Z. Lu, Redox of Dual-Radical Intermediates in a Methylene-Linked Covalent Triazine Framework for High-Performance Lithium-Ion Batteries, *ACS Appl. Mater. Interfaces* 13 (2021) 514–521, <https://doi.org/10.1021/acsmi.0c17692>.
- [143] Z. Lei, Q. Yang, Y. Xu, S. Guo, W. Sun, H. Liu, L. Lv, Y. Zhang, Y. Wang, Boosting lithium storage in covalent organic framework via activation of 14-electron redox chemistry, *Nat. Commun.* 9 (2018) 576, <https://doi.org/10.1038/s41467-018-02889-7>.
- [144] L. Tian, W. Zhang, Z. Xie, K. Peng, Q. Ma, Q. Xu, S. Pasupathi, H. Su, Enhanced Performance and Durability of High-temperature Polymer Electrolyte Membrane Fuel Cell by Incorporating Covalent Organic Framework into Catalyst Layer, *Acta Phys.-Chim. Sin.* 37 (2021) 2009049, <https://doi.org/10.3866/PKU.WHXB202009049>.
- [145] H.M. El-Kaderi, J.R. Hunt, J.L. Mendoza-Cortés, A.P. Côté, R.E. Taylor, M. O'Keeffe, O.M. Yaghi, Designed synthesis of 3D covalent organic frameworks, *Science* 316 (2007) 268–272, <https://doi.org/10.1126/science.1139915>.
- [146] Q. Fang, J. Wang, S. Gu, R.B. Kaspar, Z. Zhuang, J. Zheng, H. Guo, 3D porous crystalline polyimide covalent organic frameworks for drug delivery, *J. Am. Chem. Soc.* 137 (2015) 8352–83555, <https://doi.org/10.1021/jacs.5b04147>.
- [147] C. Wu, Y. Liu, H. Liu, C. Duan, Q. Pan, J. Zhu, F. Hu, X. Ma, T. Jiu, Z. Li, Y. Zhao, Highly conjugated three-dimensional covalent organic frameworks based on spirobifluorene for perovskite solar cell enhancement, *J. Am. Chem. Soc.* 140 (2018) 10016–10024, <https://doi.org/10.1021/jacs.8b06291>.
- [148] S. Yan, X. Guan, H. Li, D. Li, M. Xue, Y. Yan, V. Valtchev, S. Qiu, Q. Fang, Three-dimensional salphen-based covalent-organic frameworks as catalytic antioxidants, *J. Am. Chem. Soc.* 141 (2019) 2920–2924, <https://doi.org/10.1021/jacs.9b00485>.
- [149] X. Han, J. Huang, C. Yuan, Y. Liu, Y. Cui, Chiral 3D covalent organic frameworks for high performance liquid chromatographic enantioseparation, *J. Am. Chem. Soc.* 140 (2018) 892–895, <https://doi.org/10.1021/jacs.7b12110>.
- [150] F.J. Uribe-Romo, J.R. Hunt, H. Furukawa, C. Klöck, M. O'Keeffe, O.M. Yaghi, A Crystalline Imine-Linked 3-D Porous Covalent Organic Framework, *J. Am. Chem. Soc.* 131 (2009) 4570–4571, <https://doi.org/10.1021/ja8096256>.
- [151] G. Lin, H. Ding, R. Chen, Z. Peng, B. Wang, C. Wang, 3D porphyrin-based covalent organic frameworks, *J. Am. Chem. Soc.* 139 (2017) 8705–8709, <https://doi.org/10.1021/jacs.7b04141>.
- [152] G. Lin, H. Ding, D. Yuan, B. Wang, C. Wang, A pyrene-based, fluorescent three-dimensional covalent organic framework, *J. Am. Chem. Soc.* 138 (2016) 3302–3305, <https://doi.org/10.1021/jacs.6b00652>.
- [153] C. Gao, J. Li, S. Yin, G. Lin, T. Ma, Y. Meng, J. Sun, C. Wang, Isostructural three-dimensional covalent organic frameworks, *Angew. Chem., Int. Ed.* 58 (2019) 9770–9775, <https://doi.org/10.1002/anie.201905591>.
- [154] H. Li, J. Ding, X. Guan, F. Chen, C. Li, L. Zhu, M. Xue, D. Yuan, V. Valtchev, Y. Yan, S. Qiu, Q. Fang, Three-Dimensional Large-Pore Covalent Organic Framework with stp Topology, *J. Am. Chem. Soc.* (142) (2020) 13334–13338, [dx.10.1021/jacs.0c06485](https://doi.org/10.1021/jacs.0c06485).
- [155] Z. Li, L. Sheng, H. Wang, X. Wang, M. Li, Y. Xu, H. Cui, H. Zhang, H. Liang, H. Xu, X. He, Three-Dimensional Covalent Organic Framework with ceq Topology, *J. Am. Chem. Soc.* 143 (2021) 92–96, <https://doi.org/10.1021/jacs.0c11313>.
- [156] H. Li, F. Chen, X. Guan, J. Li, C. Li, B. Tang, V. Valtchev, Y. Yan, S. Qiu, Q. Fang, Three-Dimensional Triptycene-Based Covalent Organic Frameworks with ceq or acs Topology, *J. Am. Chem. Soc.* 143 (2021) 2654–2659, <https://doi.org/10.1021/jacs.0c12499>.
- [157] Y. Xie, J. Li, C. Lin, B. Gui, C. Ji, D. Yuan, J. Sun, C. Wang, Tuning the Topology of Three-Dimensional Covalent Organic Frameworks via Steric Control: From pts to Unprecedented ljh, *J. Am. Chem. Soc.* 143 (2021) 7279–7284, <https://doi.org/10.1021/jacs.1c03042>.
- [158] L. Chen, C. Gong, X. Wang, F. Dai, M. Huang, X. Wu, C.Z. Lu, Y. Peng, Substoichiometric 3D Covalent Organic Frameworks Based on Hexagonal Linkers, *J. Am. Chem. Soc.* 143 (2021) 10243–10249, <https://doi.org/10.1021/jacs.1c03739>.
- [159] Z. Shan, M. Wu, D. Zhu, X. Wu, K. Zhang, R. Verdusco, G. Zhang, 3D Covalent Organic Frameworks with Interpenetrated pcb Topology Based on 8-Connected Cubic Nodes, *J. Am. Chem. Soc.* 144 (2022) 5728–5733, <https://doi.org/10.1021/jacs.2c01037>.
- [160] L. Li, Q. Yun, C. Zhu, G. Sheng, J. Guo, B. Chen, M. Zhao, Z. Zhang, Z. Lai, X. Zhang, Y. Peng, Y. Zhu, H. Zhang, Isorecticular Series of Two-Dimensional Covalent Organic Frameworks with the kgd Topology and Controllable Micropores, *J. Am. Chem. Soc.* 144 (2022) 6475–6482, <https://doi.org/10.1021/jacs.2c01199>.
- [161] S.L. James, C.J. Adams, C. Bolm, D. Braga, P. Collier, T. Friščić, F. Greponi, K.D. M. Harris, G. Hyett, W. Jones, A. Krebs, J. Mack, L. Maini, A.G. Orpen, I.P. Parkin, W.C. Shearouse, J.W. Steed, D.C. Waddell, Mechanochemistry: opportunities for new and cleaner synthesis, *Chem. Soc. Rev.* 41 (2012) 413–417, <https://doi.org/10.1039/C1CS15171A>.
- [162] B.P. Biswal, S. Chandra, S. Kandambeth, B. Lukose, T. Heine, R. Banerjee, Mechanochemical synthesis of chemically stable isorecticular covalent organic frameworks, *J. Am. Chem. Soc.* 135 (2013) 5328–5331, <https://doi.org/10.1021/ja4017842>.
- [163] G. Das, D.B. Shinde, S. Kandambeth, B.P. Biswal, R. Banerjee, Mechanochemical synthesis of imine, beta-ketoenamine, and hydrogen-bonded imine-linked covalent organic frameworks using liquid-assisted grinding, *Chem. Commun.* 50 (2014) 12615–12618, <https://doi.org/10.1039/C4CC03389B>.
- [164] X. Wang, R. Ma, L. Hao, Q. Wu, C. Wang, Z. Wang, Mechanochemical synthesis of covalent organic framework for the efficient extraction of benzoylurea insecticides, *J. Chromatogr. A* 1551 (2018) 1–9, <https://doi.org/10.1016/j.chroma.2018.03.053>.
- [165] J.H. Bang, K.S. Suslick, Applications of ultrasound to the synthesis of nanostructured materials, *Adv. Mater.* 22 (2010) 1039–1059, <https://doi.org/10.1002/adma.200904093>.
- [166] S.T. Yang, J. Kim, H.Y. Cho, S. Kim, W.S. Ahn, Facile synthesis of covalent organic frameworks COF-1 and COF-5 by sonochemical method, *RSC Adv.* 2 (2012) 10179–10181, <https://doi.org/10.1039/C2RA21531D>.
- [167] M.B. Gawande, S.N. Shelke, R. Zboril, R.S. Varma, Microwave-assisted chemistry: synthetic applications for rapid assembly of nanomaterials and organics, *Acc. Chem. Res.* 47 (2014) 1338–1348, <https://doi.org/10.1021/ar400309b>.
- [168] E. Vitaku, W.R. Dichtel, Synthesis of 2D imine-linked covalent organic frameworks through formal transamination reactions, *J. Am. Chem. Soc.* (139) (2017), 12911–12914, [10.1021/jacs.7b06913](https://doi.org/10.1021/jacs.7b06913).
- [169] H. Wei, S.Z. Chai, N.T. Hu, Z. Yang, L.M. Wei, L. Wang, The microwave-assisted solvothermal synthesis of a crystalline two-dimensional covalent organic framework with high CO₂ capacity, *Chem Commun.* 51 (2015) 12178–12181, <https://doi.org/10.1039/C5CC04680G>.
- [170] S. Kim, H.C. Choi, Light-promoted synthesis of highly-conjugated crystalline covalent organic framework, *Commun. Chem.* 2 (2019) 60, <https://doi.org/10.1038/s42004-019-0162-z>.
- [171] Y. Jiang, W. Huang, J. Wang, Q. Wu, H. Wang, L. Pan, X. Liu, Green, scalable and morphology controlled synthesis of nanofibrous covalent organic frameworks and their nanohybrids through a vapor-assisted solid-state approach, *J. Mater. Chem. A* 2 (2014) 8201–8204, <https://doi.org/10.1039/C4TA00555D>.
- [172] D.D. Medina, J.M. Rotter, Y. Hu, M. Dogru, V. Werner, F. Auras, J.T. Markiewicz, P. Knochel, T. Bein, Room temperature synthesis of covalent-organic framework films through vapor-assisted conversion, *J. Am. Chem. Soc.* 137 (2015) 1016–1019, <https://doi.org/10.1021/ja510895m>.
- [173] W. Dai, F. Shao, J. Szczerbiński, R. McCaffrey, R. Zenobi, Y. Jin, A.D. Schlüter, W. Zhang, Synthesis of a two-dimensional covalent organic monolayer through dynamic imine chemistry at the air/water interface, *Angew. Chem., Int. Ed.* 55 (2016) 213–217, <https://doi.org/10.1002/ange.201508473>.
- [174] Q. Hao, C. Zhao, B. Sun, C. Lu, J. Liu, M. Liu, L.J. Wan, D. Wang, Confined synthesis of two-dimensional covalent organic framework thin films within superspreading water layer, *J. Am. Chem. Soc.* 140 (2018) 12152–12158, <https://doi.org/10.1021/jacs.8b07120>.
- [175] K. Dey, M. Pal, K.C. Rout, H.S. Kujatttu, A. Das, R. Mukherjee, U.K. Kharul, R. Banerjee, Selective molecular separation by interfacially crystallized covalent organic framework thin films, *J. Am. Chem. Soc.* 139 (2017) 13083–13091, <https://doi.org/10.1021/jacs.7b06640>.
- [176] H. Sahabudeen, H. Qi, B.A. Glatz, D. Tranca, R. Dong, Y. Hou, T. Zhang, C. Kuttner, T. Lehnert, G. Seifert, U. Kaiser, A. Fery, Z. Zheng, X. Feng, Wafer-sized multifunctional polyimine-based two-dimensional conjugated polymers with high mechanical stiffness, *Nat. Commun.* 7 (2016) 13461, <https://doi.org/10.1038/ncomms13461>.
- [177] L. Garzón-Tovar, J. Pérez-Carvajal, A. Yazdi, J. Hernández-Muñoz, P. Tarazona, I. Imaz, F. Zamora, D. MasPOCH, A MOF@COF composite with enhanced uptake through interfacial pore generation, *Angew. Chem., Int. Ed.* 58 (2019) 9512–9516, <https://doi.org/10.1002/ange.201904766>.
- [178] Y. Xu, X. Shi, R. Hua, R. Zhang, Y. Yao, B. Zhao, T. Liu, J. Zheng, G. Lu, Remarkably catalytic activity in reduction of 4-nitrophenol and methylene blue by Fe₃O₄@COFs supported noble metal nanoparticles, *Appl. Catal. B.* (260) (2020), <https://doi.org/10.1016/j.apcatb.2019.118142>.
- [179] K. Liu, H. Qi, R. Dong, R. Shivhare, M. Addicoat, T. Zhang, H. Sahabudeen, T. Heine, S. Mannsfeld, U. Kaiser, Z. Zheng, X. Feng, On-water surface synthesis of crystalline, few-layer two-dimensional polymers assisted by surfactant monolayers, *Nat. Chem.* 11 (2019) 994–1000, <https://doi.org/10.1038/s41557-019-0327-5>.
- [180] C. Zhao, H. Lyu, Z. Ji, C. Zhu, O.M. Yaghi, Ester-Linked Crystalline Covalent Organic Frameworks, *J. Am. Chem. Soc.* 142 (2020) 14450–14454, <https://doi.org/10.1021/jacs.0c07015>.
- [181] C. Yuan, S. Fu, K. Yang, B. Hou, Y. Liu, J. Jiang, Y. Cui, Crystalline C–C and C=C Bond-Linked Chiral Covalent Organic Frameworks, *J. Am. Chem. Soc.* 143 (2021) 369–381, <https://doi.org/10.1021/jacs.0c11050>.
- [182] Z.B. Zhou, X.H. Han, Q.Y. Qi, S.X. Gan, D.L. Ma, X. Zhao, A. Facile, Efficient, and General Synthetic Method to Amide-Linked Covalent Organic Frameworks, *J. Am. Chem. Soc.* 144 (2022) 1138–1143, <https://doi.org/10.1021/jacs.1c12392>.
- [183] H. Yazdani, S.E. Hooshmand, R.S. Varma, Covalent organic frameworks, and multicomponent reactions: an endearing give-and-take relationship, *Org. Chem. Front.* 9 (2022) 4178, <https://doi.org/10.1039/D2QO00697A>.

- [184] E. Ruijter, R. Scheffelaar, R.V.A. Orru, Multicomponent Reaction Design in the Quest for Molecular Complexity and Diversity, *Angew. Chem., Int. Ed.* 50 (2011) 6234–6246, <https://doi.org/10.1002/anie.201006515>.
- [185] R.C. Cioc, E. Ruijter, R.V.A. Orru, Multicomponent reactions: advanced tools for sustainable organic synthesis, *Green Chem.* 16 (2014) 2958–2975, <https://doi.org/10.1039/C4GC00013G>.
- [186] S. Brauch, S.S. van Berkel, B. Westermann, Higher order multicomponent reactions: beyond four reactants, *Chem. Soc. Rev.* 42 (2013) 4948–4962, <https://doi.org/10.1039/C3CS35505E>.
- [187] P.L. Wang, S.Y. Ding, Z.C. Zhang, Z.P. Wang, W. Wang, Constructing Robust Covalent Organic Frameworks via Multicomponent Reactions, *J. Am. Chem. Soc.* 141 (2019) 18004–18008, <https://doi.org/10.1021/jacs.9b10625>.
- [188] X.T. Li, J. Zou, T.H. Wang, H.C. Ma, G.J. Chen, Y.B. Dong, Construction of Covalent Organic Frameworks via Three-Component One-Pot Strecker and Povarov Reactions, *J. Am. Chem. Soc.* 142 (2020) 6521–6526, <https://doi.org/10.1021/jacs.0c00969>.
- [189] J. Liu, T. Yang, Z.P. Wang, P.L. Wang, J. Feng, S.Y. Ding, W. Wang, Pyrimidazole-Based Covalent Organic Frameworks: Integrating Functionality and Ultra-stability via Isocyanide Chemistry, *J. Am. Chem. Soc.* 142 (2020) 20956–20961, <https://doi.org/10.1021/jacs.0c10919>.
- [190] J.C. Wang, X. Kan, J.Y. Shang, H. Qiao, Y.B. Dong, Catalytic Asymmetric Synthesis of Chiral Covalent Organic Frameworks from Prochiral Monomers for Heterogeneous Asymmetric Catalysis, *J. Am. Chem. Soc.* 142 (2020) 16915–16920, <https://doi.org/10.1021/jacs.0c07461>.
- [191] K. Wang, Z. Jia, Y. Bai, X. Wang, S.E. Hodgkiss, L. Chen, S.Y. Chong, X. Wang, H. Yang, Y. Xu, F. Feng, J.W. Ward, A.I. Cooper, Synthesis of Stable Thiazole-Linked Covalent Organic Frameworks via a Multicomponent Reaction, *J. Am. Chem. Soc.* 142 (2020) 11131–11138, <https://doi.org/10.1021/jacs.0c03418>.
- [192] B.X. Lee, F. Kjaerulf, S. Turner, L. Cohen, P.D. Donnelly, R. Muggah, R. Davis, A. Realini, B. Kieselbach, L.S. MacGregor, I. Waller, R. Gordon, M. Moloney-Kitts, C. Lee, J. Gilligan, Transforming Our World: Implementing the 2030 Agenda Through Sustainable Development Goal Indicators, *J. Public Health Policy* 37 (2016) S13–S31, <https://doi.org/10.1057/s41271-016-0002-7>.
- [193] I.P. Jain, C. Lal, A. Jain, Hydrogen storage in Mg: A most promising material, *Int J Hydrogen Energy* 35 (2010) 5133–5144, <https://doi.org/10.1016/j.ijhydene.2009.08.088>.
- [194] I. Dincer, Renewable energy and sustainable development: a crucial review, *Renew. Sust. Energy. Rev.* 4 (2000) 157–175, [https://doi.org/10.1016/S1364-0321\(99\)00011-8](https://doi.org/10.1016/S1364-0321(99)00011-8).
- [195] T.M. Gur, Review of electrical energy storage technologies, materials and systems: challenges and prospects for large-scale grid storage, *Energy Environ. Sci.* 11 (2018) 2696–2767, <https://doi.org/10.1039/C8EE01419A>.
- [196] J.I. Perez-Diaz, M. Chazarra, J. Garcia-Gonzalez, G. Cavazzini, A. Stoppato, Trends and challenges in the operation of pumped-storage hydropower plants, *Renew. Sust. Energy. Rev.* 44 (2015) 767–784, <https://doi.org/10.1016/j.rser.2015.01.029>.
- [197] M. Gotz, J. Lefebvre, F. Mors, A.M. Koch, F. Graf, S. Bajohr, R. Reimert, T. Kolb, Renewable Power-to-Gas: A technological and economic review, *Renew. Energy* 85 (2016) 1371–1390, <https://doi.org/10.1016/j.renene.2015.07.066>.
- [198] G. Glenk, S. Reichelstein, Reversible Power-to-Gas systems for energy conversion and storage, *Nat. Commun.* 13 (2022) 2010, <https://doi.org/10.1038/s41467-022-29520-0>.
- [199] N. Kamyar, Y. Khani, M.M. Amini, F. Bahadoran, N. Safari, Embedding Pt-SnO Nanoparticles into MIL-101(Cr) Pores: Hydrogen Production with Low Carbon Monoxide Content from a New Methanol Steam Reforming Catalyst, *ChemistrySelect* 4 (2019) 6113–6122, <https://doi.org/10.1002/slct.201901071>.
- [200] Y. Khani, N. Kamyar, F. Bahadoran, N. Safari, M.M. Amini, High H₂ selectivity with low coke formation for methanol steam reforming over Cu/Y_{1.5}Ce_{0.84}Ru_{0.04}O₄ catalyst in a microchannel plate reactor, *Renew. Energy* 156 (2020) 1055–1064, <https://doi.org/10.1016/j.ijhydene.2021.10.089>.
- [201] Y. Chen, S.T. Li, S.Y. Lv, Y.M. Huang, A novel synthetic route for MOF-derived CuO-CeO₂ catalyst with remarkable methanol steam reforming performance, *Catal. Commun.* 149 (2021), <https://doi.org/10.1016/j.catcom.2020.106215>.
- [202] M. Varmazyari, Y. Khani, F. Bahadoran, Z. Shariatnia, S. Soltanali, Hydrogen production employing Cu(BDC) metal-organic framework support in methanol steam reforming process within monolithic micro-reactors, *Int. J. Hydrogen Energy* 46 (2021) 565–580, <https://doi.org/10.1016/j.ijhydene.2020.09.245>.
- [203] A.A. Lytkina, N.A. Zhilyaeva, M.M. Ermilova, N.V. Orekhova, A.B. Yaroslavl'tsev, Influence of the support structure and composition of Ni-Cu-based catalysts on hydrogen production by methanol steam reforming, *Int. J. Hydrogen Energy* 40 (2015) 9677–9684, <https://doi.org/10.1016/j.ijhydene.2015.05.094>.
- [204] Z.G. Qi, C.Z. He, A. Kaufman, Effect of CO in the anode fuel on the performance of PEM fuel cell cathode, *J. Power Sources* 111 (2002) 239–247, [https://doi.org/10.1016/S0378-7753\(02\)00300-2](https://doi.org/10.1016/S0378-7753(02)00300-2).
- [205] B.A. Peppley, J.C. Amphlett, L.M. Kearns, R.F. Mann, Methanol-steam reforming on Cu/ZnO/Al₂O₃ catalysts. Part 2. A comprehensive kinetic model, *Appl. Catal. A: Gen* 179 (1999) 31–49, [https://doi.org/10.1016/S0926-860X\(98\)00299-3](https://doi.org/10.1016/S0926-860X(98)00299-3).
- [206] B.A. Peppley, J.C. Amphlett, L.M. Kearns, R.F. Mann, Methanol-steam reforming on Cu/ZnO/Al₂O₃. Part 1: the reaction network, *Appl. Catal. A: Gen* 179 (1999) 21–29, [https://doi.org/10.1016/S0926-860X\(98\)00298-1](https://doi.org/10.1016/S0926-860X(98)00298-1).
- [207] T.L. LeValley, A.R. Richard, M.H. Fan, The progress in water gas shift and steam reforming hydrogen production technologies – A review, *Int. J. Hydrogen Energy* 39 (2014) 16983–17000, <https://doi.org/10.1016/j.ijhydene.2014.08.041>.
- [208] P. Tahay, Y. Khani, M. Jabari, F. Bahadoran, N. Safari, Highly porous monolith/TiO₂ supported Cu, Cu-Ni, Ru, and Pt catalysts in methanol steam reforming process for H₂ generation, *Appl. Catal. A: Gen* 554 (2018) 44–53, <https://doi.org/10.1016/j.apcata.2018.01.022>.
- [209] B.Y. Hwang, S. Sakthianathan, T.W. Chiu, Production of hydrogen from steam reforming of methanol carried out by self-combusted CuCr_{1-x}Fe_xO₂ (x = 0–1) nanopowders catalyst, *Int. J. Hydrogen Energy* 44 (2019) 2848–2856, <https://doi.org/10.1016/j.ijhydene.2018.12.052>.
- [210] B.L. Kniep, F. Girgsdies, T. Ressler, Effect of precipitate aging on the microstructural characteristics of Cu/ZnO catalysts for methanol steam reforming, *J. Catal.* 236 (2005) 34–44, <https://doi.org/10.1016/j.jcat.2005.09.001>.
- [211] N. Srisiriwat, S. Therdthianwong, A. Therdthianwong, Oxidative steam reforming of ethanol over Ni/Al₂O₃ catalysts promoted by CeO₂, ZrO₂ and CeO₂-ZrO₂, *Int. J. Hydrogen Energy* 34 (2009) 2224–2234, <https://doi.org/10.1016/j.ijhydene.2008.12.058>.
- [212] E.A. Sanchez, R.A. Comelli, Hydrogen production by glycerol steam-reforming over nickel and nickel-cobalt impregnated on alumina, *Int. J. Hydrogen Energy* 39 (2014) 8650–8655, <https://doi.org/10.1016/j.ijhydene.2013.12.067>.
- [213] L.F. Bobadilla, F. Romero-Sarria, M.A. Centeno, J.A. Odriozola, Promoting effect of Sn on supported Ni catalyst during steam reforming of glycerol, *Int. J. Hydrogen Energy* 41 (2016) 9234–9244, <https://doi.org/10.1016/j.ijhydene.2016.04.119>.
- [214] D. Liu, Y. Men, J.G. Wang, G. Kolb, X. Liu, Y.Q. Wang, Q.Y. Sun, Highly active and durable Pt/In₂O₃/Al₂O₃ catalysts in methanol steam reforming, *Int. J. Hydrogen Energy* 41 (2016) 21990–21999, <https://doi.org/10.1016/j.ijhydene.2016.08.184>.
- [215] M. Razavian, S. Fatemi, M.M. Mohammadi, A. Nouralishahi, Nickel supported ZIF-8/PEG modified catalyst: A designed active catalyst with high H₂ productivity in steam reforming of ethanol at moderate temperature, *J. Environ. Chem. Eng.* 9 (2021), <https://doi.org/10.1016/j.jece.2021.105531>.
- [216] M.D. Argyle, C.H. Bartholomew, Heterogeneous Catalyst Deactivation and Regeneration: A Review, *Catalysts* 5 (2015) 145–269, <https://doi.org/10.3390/catal5010145>.
- [217] P. Fornasiero, R. Dimonte, G.R. Rao, J. Kaspar, S. Meriani, A. Trovarelli, M. Graziani, Rh-Loaded CeO₂-ZrO₂ Solid-Solutions as Highly Efficient Oxygen Exchangers: Dependence of the Reduction Behavior and the Oxygen Storage Capacity on the Structural-Properties, *J. Catal.* 151 (1995) 168–177, <https://doi.org/10.1006/jcat.1995.1019>.
- [218] J.D. Holladay, J. Hu, D.L. King, Y. Wang, An overview of hydrogen production technologies, *Catalysis Today* 139 (2009) 244–260, <https://doi.org/10.1016/j.cattod.2008.08.039>.
- [219] A. Gual, C. Godard, S. Castillon, D. Curulla-Ferre, C. Claver, Colloidal Ru, Co and Fe-nanoparticles. Synthesis and application as nanocatalysts in the Fischer-Tropsch process, *Catal. Today* 183 (2012) 154–171, <https://doi.org/10.1016/j.cattod.2011.11.025>.
- [220] W.L. Luyben, Control of parallel dry methane and steam methane reforming processes for Fischer-Tropsch syngas, *J. Process Control* 39 (2016) 77–87, <https://doi.org/10.1016/j.jprocont.2015.11.007>.
- [221] I. Luisetto, S. Tuti, E. Di Bartolomeo, Co and Ni supported on CeO₂ as selective bimetallic catalyst for dry reforming of methane, *Int. J. Hydrogen Energy* 37 (2012) 15992–15999, <https://doi.org/10.1016/j.ijhydene.2012.08.006>.
- [222] D. Pakhare, J. Spivey, A review of dry (CO₂) reforming of methane over noble metal catalysts, *Chem. Soc. Rev.* 43 (2014) 7813–7837, <https://doi.org/10.1039/C3CS60395D>.
- [223] M. Usman, W. Daud, H.F. Abbas, Dry reforming of methane: Influence of process parameters—A review, *Renew. Sust. Energy. Rev.* 45 (2015) 710–744, <https://doi.org/10.1016/j.rser.2015.02.026>.
- [224] L. Karam, J. Reboul, N. El Hassan, J. Nelayah, P. Massiani, Nanostructured Nickel Aluminate as a Key Intermediate for the Production of Highly Dispersed and Stable Nickel Nanoparticles Supported within Mesoporous Alumina for Dry Reforming of Methane, *Molecules* 24 (2019), <https://doi.org/10.3390/molecules24224107>.
- [225] L. Karam, J. Reboul, S. Casale, P. Massiani, N. El Hassan, Porous Nickel-Alumina Derived from Metal-Organic Framework (MIL-53): A New Approach to Achieve Active and Stable Catalysts in Methane Dry Reforming, *Chemcatchem* 12 (2020) 373–385, <https://doi.org/10.1002/cctc.201901278>.
- [226] L. Karam, A. Miglio, S. Specchia, N. El Hassan, P. Massiani, J. Reboul, PET waste as organic linker source for the sustainable preparation of MOF-derived methane dry reforming catalysts, *Mater. Adv.* 2 (2021) 2750–2758, <https://doi.org/10.1039/D0MA00984A>.
- [227] W.J. Jang, J.O. Shim, H.M. Kim, S.Y. Yoo, H.S. Roh, A review on dry reforming of methane in aspect of catalytic properties, *Catal. Today* 324 (2019) 15–26, <https://doi.org/10.1016/j.cattod.2018.07.032>.
- [228] T.Y. Liang, D.S. Raja, K.C. Chin, C.L. Huang, S.A.P. Sethupathi, L.K. Leong, D.H. Tsai, S.Y. Lu, Bimetallic Metal-Organic Framework-Derived Hybrid Nanostructures as High-Performance Catalysts for Methane Dry Reforming, *ACS Appl. Mater. Interfaces*, (12) (2020) 15183–15193, [10.1021/acsaami.0c00086](https://doi.org/10.1021/acsaami.0c00086).
- [229] I. Khan, A. Ramirez, G. Shterk, L. Garzon-Tovar, J. Gascon, Bimetallic Metal-Organic Framework Mediated Synthesis of Ni-Co Catalysts for the Dry Reforming of Methane, *Catalysts* 10 (2020) 592, <https://doi.org/10.3390/catal10050592>.

- [230] R.S. Abiev, D.A. Sladkovskiy, K.V. Semikin, D.Y. Murzin, E.V. Rebrov, Non-Thermal Plasma for Process and Energy Intensification in Dry Reforming of Methane, *Catalysts* 10 (2020) 1358, <https://doi.org/10.3390/catal10111358>.
- [231] D. Yap, J.M. Tatibouet, C. Batiot-Dupeyrat, Catalyst assisted by non-thermal plasma in dry reforming of methane at low temperature, *Catal. Today* 299 (2020) 263–271, <https://doi.org/10.1016/j.cattod.2017.07.020>.
- [232] R. Vakilii, R. Gholami, C.E. Stere, S. Chansai, H. Chen, S.M. Holmes, Y.L. Jiao, C. Hardacre, X.L. Fan, Plasma-assisted catalytic dry reforming of methane (DRM) over metal-organic frameworks (MOFs)-based catalysts, *Appl. Catal. B* 260 (2020), <https://doi.org/10.1016/j.apcatb.2019.118195>.
- [233] K. Meyer, M. Ranocchiari, J.A. van Bokhoven, Metal organic frameworks for photo-catalytic water splitting, *Energy Environ. Sci.* 8 (2015) 1923–1937, <https://doi.org/10.1039/C5EE00161G>.
- [234] M. Ni, M.K.H. Leung, D.Y.C. Leung, K. Sumathy, A review and recent developments in photocatalytic water-splitting using TiO₂ for hydrogen production, *Renew. Sustain. Energy Rev.* 11 (2007) 401–425, <https://doi.org/10.1016/j.rser.2005.01.009>.
- [235] E. Amouyal, Photochemical production of hydrogen and oxygen from water: A review and state of the art, *Sol. Energy Mater. Sol. Cells* 38 (1995) 249–276, [https://doi.org/10.1016/0927-0248\(95\)00003-8](https://doi.org/10.1016/0927-0248(95)00003-8).
- [236] L.L. Tinker, N.D. McDaniel, P.N. Curtin, C.K. Smith, M.J. Ireland, S. Bernhard, Visible Light Induced Catalytic Water Reduction without an Electron Relay, *Chem. Eur. J.* 13 (2007) 8726–8732, <https://doi.org/10.1002/chem.200700480>.
- [237] X. Li, Q. Dong, Q. Tian, A. Sial, H. Wang, H. Wen, B. Pan, K. Zhang, J. Qin, C. Wang, Recent advance in metal- and covalent-organic framework-based photocatalysis for hydrogen evolution, *Mater. Today Chem.* 26 (2022), <https://doi.org/10.1016/j.mtchem.2022.101037>.
- [238] N. Romero, R. Bofill, L. Francàs, J. García-Antón, X. Sala, Light-Driven Hydrogen Evolution Assisted by Covalent Organic Frameworks, *Catalysts* 11 (2021) 754, <https://doi.org/10.3390/catal11060754>.
- [239] A.M. Elewa, A.F.M. EL-Mahdy, M.H. Elsayed, M.G. Mohamed, S.-W. Kuo, H.-H. Chou, Sulfur-doped triazine-conjugated microporous polymers for achieving the robust visible-light-driven hydrogen evolution, *Chem. Eng. J.* (421) (2021) 129825, <https://doi.org/10.1016/j.cej.2021.129825>.
- [240] M.G. Pfeffer, C. Müller, E.T. Kastl, A.K. Mengele, B. Bagemihl, S.S. Fauth, J. Habermann, L. Petermann, M. Wächter, M. Schulz, Active repair of a dinuclear photocatalyst for visible-light-driven hydrogen production, *Nat. Chem.* 14 (2022) 500–506, <https://doi.org/10.1038/s41557-021-00860-6>.
- [241] Y. Li, L. Yang, H. He, L. Sun, H. Wang, X. Fang, Y. Zhao, D. Zheng, Y. Qi, Z. Li, In situ photodeposition of platinum clusters on a covalent organic framework for photocatalytic hydrogen production, *Nat. Commun* 13 (2022) 1355, <https://doi.org/10.1038/s41467-022-29076-z>.
- [242] C. Mao, Y. Hu, C. Yang, C. Qin, G. Dong, Y. Zhou, Y. Zhang, Well-Designed Spherical Covalent Organic Frameworks with an Electron-Deficient and Conjugate System for Efficient Photocatalytic Hydrogen Evolution, *ACS Appl. Energy Mater.* 4 (2021) 14111–14120, <https://doi.org/10.1021/acsaem.1c02874>.
- [243] S. Ghosh, A. Nakada, M.A. Springer, T. Kawaguchi, K. Suzuki, H. Kaji, I. Baburin, A. Kuc, T. Heine, H. Suzuki, Identification of prime factors to maximize the photocatalytic hydrogen evolution of covalent organic frameworks, *J. Am. Chem. Soc.* 142 (2020) 9752–9762, <https://doi.org/10.1021/jacs.0c02633>.
- [244] J.L. Sheng, H. Dong, X.B. Meng, H.L. Tang, Y.H. Yao, D.Q. Liu, L.L. Bai, F.M. Zhang, J.Z. Wei, X.J. Sun, Effect of different functional groups on photocatalytic hydrogen evolution in covalent-organic frameworks, *ChemCatChem* 11 (2019) 2313–2319, <https://doi.org/10.1002/cctc.201900058>.
- [245] W. Chen, L. Wang, D. Mo, F. He, Z. Wen, X. Wu, H. Xu, L. Chen, Modulating benzothiadiazole-based covalent organic frameworks via halogenation for enhanced photocatalytic water splitting, *Angew. Chem.* 132 (2020) 17050–17057, <https://doi.org/10.1002/anie.202006925>.
- [246] H. Dong, X.-B. Meng, X. Zhang, H.-L. Tang, J.-W. Liu, J.-H. Wang, J.-Z. Wei, F.-M. Zhang, L.-L. Bai, X.-J. Sun, Boosting visible-light hydrogen evolution of covalent-organic frameworks by introducing Ni-based noble metal-free cocatalyst, *Chem. Eng. J.* 379 (2020), <https://doi.org/10.1016/j.cej.2019.122342>.
- [247] G. Yan, X. Sun, K. Zhang, Y. Zhang, H. Li, Y. Dou, D. Yuan, H. Huang, B. Jia, H. Li, Integrating Covalent Organic Framework with Transition Metal Phosphide for Noble-Metal-Free Visible-Light-Driven Photocatalytic H₂ Evolution, *Small* 18 (2022) 2201340, <https://doi.org/10.1002/sml.202201340>.
- [248] Z. Mi, T. Zhou, W. Weng, J. Unruangsri, K. Hu, W. Yang, C. Wang, K.A. Zhang, J. Guo, Covalent Organic Frameworks Enabling Site Isolation of Viologen-Derived Electron-Transfer Mediators for Stable Photocatalytic Hydrogen Evolution, *Angew. Chem.* 133 (2021) 9728–9735, <https://doi.org/10.1002/anie.202016618>.
- [249] J. Yang, A. Achariya, M.Y. Ye, J. Rabeah, S. Li, Z. Kochovski, S. Youk, J. Roeser, J. Grüneberg, C. Penschke, Protonated Imine-Linked Covalent Organic Frameworks for Photocatalytic Hydrogen Evolution, *Angew. Chem. Int. Ed.* 60 (2021) 19797–19803, <https://doi.org/10.1002/anie.202104870>.
- [250] R. Lu, C. Liu, Y. Chen, L. Tan, G. Yuan, P. Wang, C. Wang, H. Yan, Effect of linkages on photocatalytic H₂ evolution over covalent organic frameworks, *J. Photochem. Photobiol. A: Chem.* 421 (2021), <https://doi.org/10.1016/j.jphotochem.2021.113546>.
- [251] P. Dong, Y. Wang, A. Zhang, T. Cheng, X. Xi, J. Zhang, Platinum Single Atoms Anchored on a Covalent Organic Framework: Boosting Active Sites for Photocatalytic Hydrogen Evolution, *ACS Catalysis* 11 (2021) 13266–13279, <https://doi.org/10.1021/acscatal.1c03441>.
- [252] R. Chen, Y. Wang, Y. Ma, A. Mal, X.-Y. Gao, L. Gao, L. Qiao, X.-B. Li, L.-Z. Wu, C. Wang, Rational design of isostructural 2D porphyrin-based covalent organic frameworks for tunable photocatalytic hydrogen evolution, *Nat. Commun.* 12 (2021) 1–9, <https://doi.org/10.1038/s41467-021-21527-3>.
- [253] A.M. Elewa, A.F.M. El-Mahdy, A.E. Hassan, Z. Wen, J. Jayakumar, T.-L. Lee, L.-Y. Ting, I.M.A. Mekheimer, T.-F. Huang, M.H. Elsayed, C.-L. Chang, W.-C. Lin, H.-H. Chou, Solvent polarity tuning to enhance the crystallinity of 2D-covalent organic frameworks for visible-light-driven hydrogen generation, *J. Mater. Chem. A* 10 (2022) 12378–12390, <https://doi.org/10.1039/D2TA00328G>.
- [254] L.-L. Zheng, L.-S. Zhang, Y. Chen, L. Tian, X.-H. Jiang, L.-S. Chen, Q.-J. Xing, X.-Z. Liu, D.-S. Wu, J.-P. Zou, A new strategy for the fabrication of covalent organic framework-metal-organic framework hybrids via in-situ functionalization of ligands for improved hydrogen evolution reaction activity, *Chinese, J. Catal.* 43 (2022) 811–819, [https://doi.org/10.1016/S1872-2067\(21\)63892-5](https://doi.org/10.1016/S1872-2067(21)63892-5).
- [255] C. Li, J. Liu, H. Li, K. Wu, J. Wang, Q. Yang, Covalent organic frameworks with high quantum efficiency in sacrificial photocatalytic hydrogen evolution, *Nat. Commun* 13 (2022) 2357, <https://doi.org/10.1038/s41467-022-30035-x>.
- [256] Y. Wan, L. Wang, H. Xu, X. Wu, J. Yang, A Simple Molecular Design Strategy for Two-Dimensional Covalent Organic Framework Capable of Visible-Light-Driven Water Splitting, *J. Am. Chem. Soc.* 142 (2020) 4508–4516, <https://doi.org/10.1021/jacs.0c00564>.
- [257] S. Zhang, G. Cheng, L. Guo, N. Wang, B. Tan, S. Jin, Strong-base-assisted synthesis of a crystalline covalent triazine framework with high hydrophilicity via benzylamine monomer for photocatalytic water splitting, *Angew. Chem.* 132 (2020) 6063–6070, <https://doi.org/10.1002/ange.201914424>.
- [258] J.-L. Sheng, H. Dong, X.-B. Meng, H.-L. Tang, Y.-H. Yao, D.-Q. Liu, L.-L. Bai, F.-M. Zhang, J.-Z. Wei, X.-J. Sun, Effect of Different Functional Groups on Photocatalytic Hydrogen Evolution in Covalent-Organic Frameworks, *ChemCatChem* 11 (2019) 2313–2319, <https://doi.org/10.1002/cctc.201900058>.
- [259] N. Xu, Y. Liu, W. Yang, J. Tang, B. Cai, Q. Li, J. Sun, K. Wang, B. Xu, Q. Zhang, 2D–2D Heterojunctions of a Covalent Triazine Framework with a Triphenylphosphine-Based Covalent Organic Framework for Efficient Photocatalytic Hydrogen Evolution, *ACS Appl. Energy Mater.* 3 (2020) 11939–11946, <https://doi.org/10.1021/acsaem.0c02102>.
- [260] A.F.M. EL-Mahdy, A.M. Elewa, S.W. Huang, H.H. Chou, S.W. Kuo, Dual-function fluorescent covalent organic frameworks: HCl sensing and photocatalytic H₂ evolution from water, *Adv. Opt. Mater.*, (8) (2020) 2000641, <https://doi.org/10.1002/adom.202000641>.
- [261] J. Zhang, Y. Cao, W. Liu, T. Cao, J. Qian, J. Wang, X. Yao, A. Iqbal, W. Qin, Structural Engineering of Covalent Organic Frameworks Comprising Two Electron Acceptors Improves Photocatalytic Performance, *ChemSusChem* 15 (2022) e202101510.
- [262] B. You, Y. Sun, Innovative Strategies for Electrocatalytic Water Splitting, *Acc. Chem. Res.* 51 (2018) 1571–1580, <https://doi.org/10.1021/acs.accounts.8b00002>.
- [263] S. Sultan, J.N. Tiwari, A.N. Singh, S. Zhumagali, M. Ha, C.W. Myung, P. Thangavel, K.S. Kim, Single Atoms and Clusters Based Nanomaterials for Hydrogen Evolution, Oxygen Evolution Reactions, and Full Water Splitting, *Adv. Energy Mater.* 9 (2019) 1900624, <https://doi.org/10.1002/aenm.201900624>.
- [264] J. Wang, F. Xu, H. Jin, Y. Chen, Y. Wang, Non-Noble Metal-based Carbon Composites in Hydrogen Evolution Reaction: Fundamentals to Applications, *Adv. Mater.* 29 (2017) 1605838, <https://doi.org/10.1002/adma.201605838>.
- [265] V. Artero, M. Chavarot-Kerlidou, M. Fontecave, Splitting Water with Cobalt, *Angew. Chemie Int. Ed.* 50 (2011) 7238–7266, <https://doi.org/10.1002/anie.201007987>.
- [266] D. Merki, X. Hu, Recent developments of molybdenum and tungsten sulfides as hydrogen evolution catalysts, *Energy Environ. Sci.* 4 (2011) 3878–3888, <https://doi.org/10.1039/C1EE01970H>.
- [267] Y. Jiao, Y. Zheng, M. Jaroniec, S.Z. Qiao, Design of electrocatalysts for oxygen- and hydrogen-involving energy conversion reactions, *Chem. Soc. Rev.* 44 (2015) 2060–2086, <https://doi.org/10.1039/C4CS00470A>.
- [268] B.C. Patra, S. Khilari, R.N. Manna, S. Mondal, D. Pradhan, A. Pradhan, A. Bhaumik, A Metal-Free Covalent Organic Polymer for Electrocatalytic Hydrogen Evolution, *ACS Catal.*, (7) (2017) 6120–6127, <https://doi.org/10.1021/acscatal.7b01067>.
- [269] J. Duan, S. Chen, C. Zhao, Ultrathin metal-organic framework array for efficient electrocatalytic water splitting, *Nat. Commun.* 28 (2017) 15341, <https://doi.org/10.1038/ncomms15341>.
- [270] Y. Jiao, Y. Zheng, K. Davey, S.-Z. Qiao, Activity origin and catalyst design principles for electrocatalytic hydrogen evolution on heteroatom-doped graphene, *Nat. Energy* 1 (2016) 16130, <https://doi.org/10.1038/nenergy.2016.130>.
- [271] H.-W. Liang, S. Brüller, R. Dong, J. Zhang, X. Feng, K. Müllen, Molecular metal–N centres in porous carbon for electrocatalytic hydrogen evolution, *Nat. Commun.* 6 (2015) 7992, <https://doi.org/10.1038/ncomms8992>.
- [272] Y. Peng, B. Lu, S. Chen, Carbon-Supported Single Atom Catalysts for Electrochemical Energy Conversion and Storage, *Adv. Mater.* 30 (2018) 1801995, <https://doi.org/10.1002/adma.201801995>.
- [273] W. Chen, J. Pei, C. He, J. Wan, H. Ren, Y. Zhu, Y. Wang, J. Dong, S. Tian, W. Cheong, Rational Design of Single Molybdenum Atoms Anchored on N-Doped Carbon for Effective Hydrogen Evolution Reaction, *Angew. Chemie Int. Ed.* 56 (2017) 16086–16090, <https://doi.org/10.1002/anie.201710599>.

- [274] W. Chen, J. Pei, C. He, J. Wan, H. Ren, Y. Wang, J. Dong, K. Wu, W. Cheong, J. Mao, Single Tungsten Atoms Supported on MOF-Derived N-Doped Carbon for Robust Electrochemical Hydrogen Evolution, *Adv. Mater.* 30 (2018) 1800396, <https://doi.org/10.1002/adma.201800396>.
- [275] D.-Y. Wang, M. Gong, H.-L. Chou, C.-J. Pan, H.-A. Chen, Y. Wu, M.-C. Lin, M. Guan, J. Yang, C.-W. Chen, Highly Active and Stable Hybrid Catalyst of Cobalt-Doped FeS₂ Nanosheets-Carbon Nanotubes for Hydrogen Evolution Reaction, *J. Am. Chem. Soc.* 137 (2015) 1587–1592, <https://doi.org/10.1021/ja511572q>.
- [276] X. Long, G. Li, Z. Wang, H. Zhu, T. Zhang, S. Xiao, W. Guo, S. Yang, Metallic Iron-Nickel Sulfide Ultrathin Nanosheets As a Highly Active Electrocatalyst for Hydrogen Evolution Reaction in Acidic Media, *J. Am. Chem. Soc.* 137 (2015) 11900–11903, <https://doi.org/10.1021/jacs.5b07728>.
- [277] J. Yang, D. Voiry, S.J. Ahn, D. Kang, A.Y. Kim, M. Chowla, H.S. Shin, Two-Dimensional Hybrid Nanosheets of Tungsten Disulfide and Reduced Graphene Oxide as Catalysts for Enhanced Hydrogen Evolution, *Angew. Chemie* 125 (2013) 13996–13999, <https://doi.org/10.1002/ange.201307475>.
- [278] D.V. Esposito, J.G. Chen, Monolayer platinum supported on tungsten carbides as low-cost electrocatalysts: opportunities and limitations, *Energy Environ. Sci.* 4 (2011) 3900–3912, <https://doi.org/10.1039/C1EE01851E>.
- [279] H. Jin, C. Guo, X. Liu, J. Liu, A. Vasileff, Y. Jiao, Y. Zheng, S.-Z. Qiao, Emerging Two-Dimensional Nanomaterials for Electrocatalysis, *Chem. Rev.* 118 (2018) 6337–6408, <https://doi.org/10.1021/acs.chemrev.7b00689>.
- [280] B. Cao, G.M. Veith, J.C. Neufeind, R.R. Adzic, P.G. Khalifah, Mixed Close-Packed Cobalt Molybdenum Nitrides as Non-noble Metal Electrocatalysts for the Hydrogen Evolution Reaction, *J. Am. Chem. Soc.* 135 (2013) 19186–19192, <https://doi.org/10.1021/ja4081056>.
- [281] S. Bhunia, S.K. Das, R. Jana, S.C. Peter, S. Bhattacharya, M. Addicoat, A. Bhaumik, A. Pradhan, Electrochemical Stimuli-Driven Facile Metal-Free Hydrogen Evolution from Pyrene-Porphyrin-Based Crystalline Covalent Organic Framework, *ACS Appl. Mater. Interfaces* 9 (2017) 23843–23851, <https://doi.org/10.1021/acsami.7b06968>.
- [282] P. Pachfule, A. Achariya, J. Roeser, R.P. Sivasankaran, M.-Y. Ye, A. Brückner, J. Schmidt, A. Thomas, Donor–acceptor covalent organic frameworks for visible light induced free radical polymerization, *Chem. Sci.* 10 (2019) 8316–8322, <https://doi.org/10.1039/C9SC02601K>.
- [283] Y. Ma, Y. Fu, W. Jiang, Y. Wu, C. Liu, G. Che, Q. Fang, Excellent electrocatalytic performance of metal-free thiophene–sulfur covalent organic frameworks for hydrogen evolution in alkaline medium, *J. Mater. Chem. A* 10 (2022) 10092–10097, <https://doi.org/10.1039/D2TA00659F>.
- [284] W. Wang, Y. Zhang, L. Chen, H. Chen, S. Hu, Q. Li, H. Liu, S. Qiao, Tricycloquinazoline-containing 3D conjugated microporous polymers and 2D covalent quinazoline networks: microstructure and conductivity, *Polym. Chem.* 12 (2021) 650–659, <https://doi.org/10.1039/D0PY01615B>.
- [285] H. Jia, Y. Yao, Y. Gao, D. Lu, P. Du, Pyrolyzed cobalt porphyrin-based conjugated mesoporous polymers as bifunctional catalysts for hydrogen production and oxygen evolution in water, *Chem. Commun.* 52 (2016) 13483–13486, <https://doi.org/10.1039/C6CC06972J>.
- [286] X. Guan, H. Li, Y. Ma, M. Xue, Q. Fang, Y. Yan, V. Valtchev, S. Qiu, Chemically stable polyarylether-based covalent organic frameworks, *Nat. Chem.* 11 (2019) 587–594, <https://doi.org/10.1038/s41557-019-0238-5>.
- [287] Y. Bai, Y. Liu, M. Liu, X. Wang, S. Shang, W. Gao, C. Du, Y. Qiao, J. Chen, J. Dong, Near-Equilibrium Growth of Chemically Stable Covalent Organic Framework/Graphene Oxide Hybrid Materials for the Hydrogen Evolution Reaction, *Angew. Chemie* 134 (2022) e202113067.
- [288] C. Yang, S. Tao, N. Huang, X. Zhang, J. Duan, R. Makiura, S. Maenosono, Heteroatom-Doped Carbon Electrocatalysts Derived from Nanoporous Two-Dimensional Covalent Organic Frameworks for Oxygen Reduction and Hydrogen Evolution, *ACS Appl. Nano Mater.* 3 (2020) 5481–5488, <https://doi.org/10.1021/acsnano.0c00786>.
- [289] S. Ruidas, B. Mohanty, P. Bhanja, E.S. Erakulan, R. Thapa, P. Das, A. Chowdhury, S.K. Mandal, B.K. Jena, A. Bhaumik, Metal-Free Triazine-Based 2D Covalent Organic Framework for Efficient H₂ Evolution by Electrochemical Water Splitting, *ChemSusChem* 14 (2021) 5057–5064, <https://doi.org/10.1002/cssc.202101663>.
- [290] Y. Wu, J.M. Veleta, D. Tang, A.D. Price, C.E. Botez, D. Villagrán, Efficient electrocatalytic hydrogen gas evolution by a cobalt–porphyrin-based crystalline polymer, *Dalt. Trans.* 47 (2018) 8801–8806, <https://doi.org/10.1039/C8DT00302E>.
- [291] K.C. Ranjesh, R. Illathvalappil, V.C. Wakchaure, S. Goudappagouda, S.S.B. Kurungot, Metalloporphyrin Two-Dimensional Polymers via Metal-Catalyst-Free C–C Bond Formation for Efficient Catalytic Hydrogen Evolution, *ACS Appl. Energy Mater.* 1 (2018) 6442–6450, <https://doi.org/10.1021/acsaem.8b01381>.
- [292] S. Qiao, B. Zhang, Q. Li, Z. Li, W. Wang, J. Zhao, X. Zhang, Y. Hu, Pore Surface Engineering of Covalent Triazine Frameworks@MoS₂ Electrocatalyst for the Hydrogen Evolution Reaction, *ChemSusChem* 12 (2019) 5032–5040, <https://doi.org/10.1002/cssc.201902582>.
- [293] S. Maiti, A.R. Chowdhury, A.K. Das, Electrochemically Facile Hydrogen Evolution Using Ruthenium Encapsulated Two Dimensional Covalent Organic Framework (2D COF), *ChemNanoMat* 6 (2020) 99–106, <https://doi.org/10.1002/cnma.201900499>.
- [294] P. Kuhn, M. Antonietti, A. Thomas, Porous, Covalent Triazine-Based Frameworks Prepared by Ionothermal Synthesis, *Angew. Chemie Int. Ed.* 47 (2008) 3450–3453, <https://doi.org/10.1002/anie.200705710>.
- [295] S. Hug, L. Stegbauer, H. Oh, M. Hirscher, B.V. Lotsch, Nitrogen-Rich Covalent Triazine Frameworks as High-Performance Platforms for Selective Carbon Capture and Storage, *Chem. Mater.* 27 (2015) 8001–8010, <https://doi.org/10.1021/acs.chemmater.5b03330>.
- [296] A. Thomas, A. Fischer, F. Goettmann, M. Antonietti, J.-O. Müller, R. Schlögl, J. M. Carlsson, Graphitic carbon nitride materials: variation of structure and morphology and their use as metal-free catalysts, *J. Mater. Chem.* 18 (2008) 4893–4908, <https://doi.org/10.1039/B800274F>.
- [297] K. Kamiya, Selective single-atom electrocatalysts: a review with a focus on metal-doped covalent triazine frameworks, *Chem. Sci.* 11 (2020) 8339–8349, <https://doi.org/10.1039/D0SC03328F>.
- [298] D. Wu, Q. Xu, J. Qian, X. Li, Y. Sun, Bimetallic Covalent Organic Frameworks for Constructing Multifunctional Electrocatalyst, *Chem. Eur. J.* 25 (2019) 3105–3111, <https://doi.org/10.1002/chem.201805550>.
- [299] H. Sahabudeen, H. Qi, B.A. Glatz, D. Tranca, R. Dong, Y. Hou, T. Zhang, C. Kuttner, T. Lehnert, G. Seifert, Wafer-sized multifunctional polyimine-based two-dimensional conjugated polymers with high mechanical stiffness, *Nat. Commun.* 7 (2016) 13461, <https://doi.org/10.1038/ncomms13461>.
- [300] A. Wang, L. Cheng, W. Zhao, X. Shen, W. Zhu, Electrochemical hydrogen and oxygen evolution reactions from a cobalt-porphyrin-based covalent organic polymer, *J. Colloid Interface Sci.* 579 (2020) 598–606, <https://doi.org/10.1016/j.jcis.2020.06.109>.
- [301] S. Huang, K. Chen, T.-T. Li, Porphyrin and phthalocyanine based covalent organic frameworks for electrocatalysis, *Coord. Chem. Rev.*, (464) (2022) 214563, <https://doi.org/10.1016/j.ccr.2022.214563>.
- [302] G. Xu, H. Lei, G. Zhou, C. Zhang, L. Xie, W. Zhang, R. Cao, Boosting hydrogen evolution by using covalent framework of fluorinated cobalt porphyrins supported on carbon nanotubes, *Chem. Commun.* 55 (2019) 12647–12650, <https://doi.org/10.1039/C9CC06916j>.
- [303] J.-D. Yi, R. Xu, G.-L. Chai, T. Zhang, K. Zhang, B. Nan, H. Lin, Y.-L. Liang, J. Lv, J. Luo, Cobalt single-atoms anchored on porphyrinic triazine-based frameworks as bifunctional electrocatalysts for oxygen reduction and hydrogen evolution reactions, *J. Mater. Chem. A* 7 (2019) 1252–1259, <https://doi.org/10.1039/C8TA09490j>.
- [304] Y. Liang, H. Wang, J. Zhou, Y. Li, J. Wang, T. Regier, H. Dai, Covalent Hybrid of Spinel Manganese-Cobalt Oxide and Graphene as Advanced Oxygen Reduction Electrocatalysts, *J. Am. Chem. Soc.* 134 (2012) 3517–3523, <https://doi.org/10.1021/ja210924t>.
- [305] J. Liu, T. He, Q. Wang, Z. Zhou, Y. Zhang, H. Wu, Q. Li, J. Zheng, Z. Sun, Y. Lei, Confining ultrasmall bimetallic alloys in porous N-carbon for use as scalable and sustainable electrocatalysts for rechargeable Zn–air batteries, *J. Mater. Chem. A* 7 (2019) 12451–12456, <https://doi.org/10.1039/C9TA02264C>.
- [306] Y. Pan, S. Liu, K. Sun, X. Chen, B. Wang, K. Wu, X. Cao, W. Cheong, R. Shen, A. Han, A Bimetallic Zn/Fe Polyphthalocyanine-Derived Single-Atom Fe-N 4 Catalytic Site: A Superior Trifunctional Catalyst for Overall Water Splitting and Zn–Air Batteries, *Angew. Chemie Int. Ed.* 57 (2018) 8614–8618, <https://doi.org/10.1002/anie.201804349>.
- [307] D. Friebe, M.W. Louie, M. Bajdich, K.E. Sanwald, Y. Cai, A.M. Wise, M.-J. Cheng, D. Sokaras, T.-C. Weng, R. Alonso-Mori, Identification of Highly Active Fe Sites in (Ni, Fe)OOH for Electrocatalytic Water Splitting, *J. Am. Chem. Soc.* 137 (2015) 1305–1313, <https://doi.org/10.1021/ja511559d>.
- [308] F. Song, X. Hu, Exfoliation of layered double hydroxides for enhanced oxygen evolution catalysis, *Nat. Commun.* 5 (2014) 4477, <https://doi.org/10.1038/ncomms5477>.
- [309] R. Subbaraman, D. Tripkovic, K.-C. Chang, D. Strmcnik, A.P. Paulikas, P. Hirunsit, M. Chan, J. Greeley, V. Stamenkovic, N.M. Markovic, Trends in activity for the water electrolyser reactions on 3d(Ni Co, Fe, Mn) hydr(oxy) oxide catalysts, *Nat. Mater.* 11 (2012) 550–557, <https://doi.org/10.1038/nmat3313>.
- [310] H. Bin Yang, J. Miao, S.-F. Hung, J. Chen, H.B. Tao, X. Wang, L. Zhang, R. Chen, J. Gao, H.M. Chen, Identification of catalytic sites for oxygen reduction and oxygen evolution in N-doped graphene materials: Development of highly efficient metal-free bifunctional electrocatalyst, *Sci. Adv.* 2 (2016) e1501122.
- [311] K. Qu, Y. Zheng, S. Dai, S.Z. Qiao, Graphene oxide–polydopamine derived N, S-codoped carbon nanosheets as superior bifunctional electrocatalysts for oxygen reduction and evolution, *Nano Energy* 19 (2016) 373–381, <https://doi.org/10.1016/j.nanoen.2015.11.027>.
- [312] S. Gopi, M. Kathiresan, 1,4-Phenylenediamine based covalent triazine framework as an electro catalyst, *Polymer*. 109 (2017) 315–320, <https://doi.org/10.1016/j.polymer.2016.12.052>.
- [313] S. Gopi, K. Giribabu, M. Kathiresan, Porous Organic Polymer-Derived Carbon Composite as a Bimodal Catalyst for Oxygen Evolution Reaction and Nitrophenol Reduction, *ACS omega* 3 (2018) 6251–6258, <https://doi.org/10.1021/acsomega.8b00574>.
- [314] H.B. Aiyappa, J. Thote, D.B. Shinde, R. Banerjee, S. Kurungot, Cobalt-Modified Covalent Organic Framework as a Robust Water Oxidation Electrocatalyst, *Chem. Mater.* 28 (2016) 4375–4379, <https://doi.org/10.1021/acs.chemmater.6b01370>.
- [315] S.M. Barnett, K.I. Goldberg, J.M. Mayer, A soluble copper-bipyridine water-oxidation electrocatalyst, *Nat. Chem.* 4 (2012) 498–502, <https://doi.org/10.1038/nchem.1350>.
- [316] N. Elgrishi, M.B. Chambers, X. Wang, M. Fontecave, Molecular polypyridine-based metal complexes as catalysts for the reduction of CO₂, *Chem. Soc. Rev.* 46 (2017) 761–796, <https://doi.org/10.1039/C5CS00391A>.
- [317] X. Liu, L. Feng, Y. Li, T. Xia, Z. Sui, Q. Chen, Covalent Organic Framework Composites Containing Bipyridine Metal Complex for Oxygen Evolution and Methane Conversion, *Molecules* 7 (2022) 5193, <https://doi.org/10.3390/molecules27165193>.

- [318] Z. Gao, Z. Yu, Y. Huang, X. He, X. Su, L. Xiao, Y. Yu, X. Huang, F. Luo, Flexible and robust bimetallic covalent organic frameworks for the reversible switching of electrocatalytic oxygen evolution activity, *J. Mater. Chem. A* 8 (2020) 5907–5912, <https://doi.org/10.1039/C9TA14023A>.
- [319] B. Wurster, D. Grumelli, D. Hötger, R. Gutzler, K. Kern, Driving the Oxygen Evolution Reaction by Nonlinear Cooperativity in Bimetallic Coordination Catalysts, *J. Am. Chem. Soc.* 138 (2016) 3623–3626, <https://doi.org/10.1021/jacs.5b10484>.
- [320] Y. Naruta, M. Sasayama, T. Sasaki, Oxygen Evolution by Oxidation of Water with Manganese Porphyrin Dimers, *Angew. Chemie Int. Ed.* 33 (1994) 1839–1841, <https://doi.org/10.1002/anie.199418391>.
- [321] S. Shaik, H. Hirao, D. Kumar, Reactivity of High-Valent Iron-Oxo Species in Enzymes and Synthetic Reagents: A Tale of Many States, *Acc. Chem. Res.* 40 (2007) 532–542, <https://doi.org/10.1021/ar600042c>.
- [322] C. Lin, L. Zhang, Z. Zhao, Z. Xia, Design Principles for Covalent Organic Frameworks as Efficient Electrocatalysts in Clean Energy Conversion and Green Oxidizer Production, *Adv. Mater.* 29 (2017) 1606635, <https://doi.org/10.1002/adma.201606635>.
- [323] S. Bhunia, K. Bhunia, B.C. Patra, S.K. Das, D. Pradhan, A. Bhaumik, A. Pradhan, S. Bhattacharya, Efficacious Electrochemical Oxygen Evolution from a Novel Co(II) Porphyrin/Pyrene-Based Conjugated Microporous Polymer, *ACS Appl. Mater. Interfaces* 11 (2018) 1520–1528, <https://doi.org/10.1021/acsami.8b20142>.
- [324] A. Singh, S. Roy, C. Das, D. Samanta, T.K. Maji, Metallophthalocyanine-based redox active metal-organic conjugated microporous polymers for OER catalysis, *Chem. Commun.* 54 (2018) 4465–4468, <https://doi.org/10.1039/C8CC01291A>.
- [325] X. Zhu, N. He, J. Ding, R. Yue, S. He, W. Liu, N. Liu, R. Guo, Z. Mo, Bimetal-anchored covalent organic frameworks derivatives for efficient alkaline electrolyte oxygen evolution, *J. Alloys Compd.* 924 (2022), <https://doi.org/10.1016/j.jallcom.2022.166442>.
- [326] C. Yang, Z.-D. Yang, H. Dong, N. Sun, Y. Lu, F.-M. Zhang, G. Zhang, Theory-Driven Design and Targeting Synthesis of a Highly-Conjugated Basal-Plane 2D Covalent Organic Framework for Metal-Free Electrocatalytic OER, *ACS Energy Lett.* 4 (2019) 2251–2258, <https://doi.org/10.1021/acscenergylett.9b01691>.
- [327] H. Wang, H.-W. Lee, Y. Deng, Z. Lu, P.-C. Hsu, Y. Liu, D. Lin, Y. Cui, Bifunctional non-noble metal oxide nanoparticle electrocatalysts through lithium-induced conversion for overall water splitting, *Nat. Commun.* 6 (2015) 7261, <https://doi.org/10.1038/ncomms8261>.
- [328] C. Ling, L. Shi, Y. Ouyang, X.C. Zeng, J. Wang, Nanosheet Supported Single-Metal Atom Bifunctional Catalyst for Overall Water Splitting, *Nano Lett.* 17 (2017) 5133–5139, <https://doi.org/10.1021/acs.nanolett.7b02518>.
- [329] T. Zhang, B. Zhang, Q. Peng, J. Zhou, Z. Sun, Mo₂B₂ MBene-supported single-atom catalysts as bifunctional HER/OER and OER/ORR electrocatalysts, *J. Mater. Chem. A* 9 (2021) 433–441, <https://doi.org/10.1039/D0TA08630D>.
- [330] X. Han, X. Ling, D. Yu, D. Xie, L. Li, S. Peng, C. Zhong, N. Zhao, Y. Deng, W. Hu, Atomically Dispersed Binary Co-Ni Sites in Nitrogen-Doped Hollow Carbon Nanocubes for Reversible Oxygen Reduction and Evolution, *Adv. Mater.* 31 (2019) 1905622, <https://doi.org/10.1002/adma.201905622>.
- [331] T. He, S.K. Matta, G. Will, A. Du, Transition-Metal Single Atoms Anchored on Graphdiyne as High-Efficiency Electrocatalysts for Water Splitting and Oxygen Reduction, *Small, Methods* 3 (2019) 1800419, <https://doi.org/10.1002/smt.201800419>.
- [332] J. Ji, C. Zhang, S. Qin, P. Jin, First-principles investigation of two-dimensional covalent-organic framework electrocatalysts for oxygen evolution/reduction and hydrogen evolution reactions, *Sustain, Energy Fuels* 5 (2021) 5615–5626, <https://doi.org/10.1039/D1SE01257F>.
- [333] J.H. Park, C.H. Lee, J. Ju, J. Lee, J. Seol, S.U. Lee, J. Kim, Bifunctional Covalent Organic Framework-Derived Electrocatalysts with Modulated p-Band Centers for Rechargeable Zn-Air Batteries, *Adv. Funct. Mater.* 31 (2021) 2101727, <https://doi.org/10.1002/adfm.202101727>.
- [334] M. Wang, C. Wang, J. Liu, F. Rong, L. He, Y. Lou, Z. Zhang, M. Du, Efficient Ag/Ag₂O-Doped Cobalt Metallo-Covalent Organic Framework Electrocatalysts for Rechargeable Zinc-Air Battery, *ACS Sustain, Chem. Eng.* 9 (2021) 5872–5883, <https://doi.org/10.1021/acssuschemeng.0c09205>.
- [335] D. Mullangi, V. Dhavale, S. Shalini, S. Nandi, S. Collins, T. Woo, S. Kurungot, R. Vaidyanathan, Low-Overpotential Electrocatalytic Water Splitting with Noble-Metal-Free Nanoparticles Supported in a sp³ N-Rich Flexible COF, *Adv. Energy Mater.* 6 (2016) 1600110, <https://doi.org/10.1002/aenm.201600110>.
- [336] Y. Xu, B. Li, S. Zheng, P. Wu, J. Zhan, H. Xue, Q. Xu, H. Pang, Ultrathin two-dimensional cobalt-organic framework nanosheets for high-performance electrocatalytic oxygen evolution, *J. Mater. Chem. A* 6 (2018) 22070–22076, <https://doi.org/10.1039/C8TA03128B>.
- [337] Y. Liang, T. Xia, Z. Wu, Y. Yang, Y. Li, Z. Sui, C. Li, R. Fan, X. Tian, Q. Chen, Tetrazole-functionalized two-dimensional covalent organic frameworks coordinated with metal ions for electrocatalytic oxygen evolution reaction, *Mater. Today Chem.* 24 (2022), <https://doi.org/10.1016/j.mtchem.2022.100777>.
- [338] Y. Zhao, Y. Yang, T. Xia, H. Tian, Y. Li, Z. Sui, N. Yuan, X. Tian, Q. Chen, Pyrimidine-Functionalized Covalent Organic Framework and its Cobalt Complex as an Efficient Electrocatalyst for Oxygen Evolution Reaction, *ChemSusChem* 14 (2021) 4556–4562, <https://doi.org/10.1002/cssc.202101434>.
- [339] Z. Gao, L. Le Gong, X.Q. He, X.M. Su, L.H. Xiao, F. Luo, General Strategy to Fabricate Metal-Incorporated Pyrolysis-Free Covalent Organic Framework for Efficient Oxygen Evolution Reaction, *Inorg. Chem.* 59 (2020) 4995–5003, <https://doi.org/10.1021/acs.inorgchem.0c00235>.
- [340] F. Kong, X. Fan, X. Zhang, L. Wang, A. Kong, Y. Shan, Soft-confinement conversion of Co-Salen-organic-frameworks to uniform cobalt nanoparticles embedded within porous carbons as robust trifunctional electrocatalysts, *Carbon* 149 (2019) 471–482, <https://doi.org/10.1016/j.carbon.2019.04.079>.
- [341] Z. Gan, S. Lu, L. Qiu, H. Zhu, H. Gu, M. Du, Fine tuning of supported covalent organic framework with molecular active sites loaded as efficient electrocatalyst for water oxidation, *Chem. Eng. J.* 415 (2021), <https://doi.org/10.1016/j.cej.2020.127850>.
- [342] S. Mondal, B. Mohanty, M. Nurhuda, S. Dalapati, R. Jana, M. Addicoat, A. Datta, B.K. Jena, A. Bhaumik, A Thiadiazole-Based Covalent Organic Framework: A Metal-Free Electrocatalyst toward Oxygen Evolution Reaction, *ACS Catal.* 10 (2020) 5623–5630, <https://doi.org/10.1021/acscatal.9b05470>.
- [343] Q. Xu, J. Qian, D. Luo, G. Liu, Y. Guo, G. Zeng, Ni/Fe Clusters and Nanoparticles Confined by Covalent Organic Framework Derived Carbon as Highly Active Catalysts toward Oxygen Reduction Reaction and Oxygen Evolution Reaction, *Adv. Sustain. Syst.* 4 (2020) 2000115, <https://doi.org/10.1002/adsu.202000115>.
- [344] R. Zhang, S. Cheng, N. Li, W. Ke, N. S-codoped graphene loaded Ni-Co bimetal sulfides for enhanced oxygen evolution activity, *Appl. Surf. Sci.*, (503) (2020) 144146, <https://doi.org/10.1016/j.apsusc.2019.144146>.
- [345] C.C. Yang, S.F. Zai, Y.T. Zhou, L. Du, Q. Jiang, Fe₃C-Co Nanoparticles Encapsulated in a Hierarchical Structure of N-Doped Carbon as a Multifunctional Electrocatalyst for ORR, OER, and HER, *Adv. Funct. Mater.* 29 (2019) 1901949, <https://doi.org/10.1002/adfm.201901949>.
- [346] M.G. Walter, E.L. Warren, J.R. McKone, S.W. Boettcher, Q. Mi, E.A. Santori, N.S. Lewis, Solar Water Splitting Cells, *Chem. Rev.* 110 (2010) 6446–6473, <https://doi.org/10.1021/cr1002326>.
- [347] W. Lubitz, E.J. Reijerse, J. Messinger, Solar water-splitting into H₂ and O₂: design principles of photosystem II and hydrogenases, *Energy Environ. Sci.* 1 (2008) 15–31, <https://doi.org/10.1039/B808792J>.
- [348] M.S. Prévot, K. Sivula, Photoelectrochemical Tandem Cells for Solar Water Splitting, *J. Phys. Chem. C* 117 (2013) 17879–17893, <https://doi.org/10.1021/jp405291g>.
- [349] J.M. Rotter, S. Weinberger, J. Kampmann, T. Sick, M. Shalom, T. Bein, D.D. Medina, Covalent Organic Framework Films through Electrophoretic Deposition—Creating Efficient Morphologies for Catalysis, *Chem. Mater.* 31 (2019) 10008–10016, <https://doi.org/10.1021/acs.chemmater.9b02286>.
- [350] X. Fan, F. Kong, A. Kong, A. Chen, Z. Zhou, Y. Shan, Covalent Porphyrin Framework-Derived Fe₂P@Fe₄N-Coupled Nanoparticles Embedded in N-Doped Carbons as Efficient Trifunctional Electrocatalysts, *ACS Appl. Mater. Interfaces* 9 (2017) 32840–32850, <https://doi.org/10.1021/acsami.7b11229>.
- [351] S. Wei, F. Zhang, W. Zhang, P. Qiang, K. Yu, X. Fu, D. Wu, S. Bi, F. Zhang, Semiconducting 2D Triazine-Cored Covalent Organic Frameworks with Unsubstituted Olefin Linkages, *J. Am. Chem. Soc.* 141 (2019) 14272–14279, <https://doi.org/10.1021/jacs.9b06219>.
- [352] L. Yao, A. Rodríguez-Camargo, M. Xia, D. Mücke, R. Guntermann, Y. Liu, L. Grunenberg, A. Jiménez-Solano, S.T. Emmerling, V. Duppel, Covalent Organic Framework Nanoplates Enable Solution-Processed Crystalline Nanofilms for Photoelectrochemical Hydrogen Evolution, *J. Am. Chem. Soc.* 144 (2022) 10291–10300, <https://doi.org/10.1021/jacs.2c01433>.
- [353] C. Dai, T. He, L. Zhong, X. Liu, W. Zhen, C. Xue, S. Li, D. Jiang, B. Liu, 2,4,6-Triphenyl-1,3,5-Triazine Based Covalent Organic Frameworks for Photoelectrochemical H₂ Evolution, *Adv. Mater. Interfaces* 8 (2021) 2002191, <https://doi.org/10.1002/admi.202002191>.
- [354] A. Pradhan, M.A. Addicoat, Photoelectrochemical water splitting with a triazine based covalent organic framework, *Sustain. Energy Fuels* 6 (2022) 4248–4255, <https://doi.org/10.1039/D2SE00827K>.